EFFECTS OF EXCITATION DENSITY AND ENERGY TRANSFER ON CATHODOLUMINESCENCE FROM POWDER PHOSPHORS WITH AND WITHOUT EMBEDDED NANOPARTICLES

By

JUNGSIK BANG

A DISSERTATION PRESENTED TO THE GRADUATE SCHOOL
OF THE UNIVERSITY OF FLORIDA IN PARTIAL FULFILLMENT
OF THE REQUIREMENTS FOR THE DEGREE OF
DOCTOR OF PHILOSOPHY

UNIVERSITY OF FLORIDA

2004

Copyright 2004

by

Jungsik Bang

This work is dedicated to my family.

ACKNOWLEDGMENTS

Above all, I would like to thank my advisor and committee chairman, Dr. Paul H. Holloway for his sincere guidance, advice, and support. It was my fortune to have the opportunity to work for him and learn valuable lessons in research and life from him.

In addition, it is my great honor to discuss data with my committee members, Dr. David Norton, Dr. Rajiv Singh, Dr. Wolfgang Sigmund and Dr. David Tanner.

I would appreciate all of the members of Dr. Holloway's group for their valuable help. I am especially thankful to Dr. Billie Abrams, Dr. Heesun Yang, Lizandra Williams and Hyukjin Lee for their friendship and discussions on research. Another special thanks go to Ludie Harmon for helping me out with everything.

I would like to thank the MAIC crew for lots of valuable data, Kwanghoon Kim for helping me collect PL data, and Dr. Brent Wagner from Georgia Technology Research Institute for time resolved CL data. In addition, I am thankful to Dr. Mostafa Abboudi from Universite Abdelmalek Essaadi for advice and discussion on combustion synthesis.

For my fundamentals in the area of science and engineering, I would like to thanks Dr. Taehyun Kwon, Dr. Myungjin Kim, Dr. Hyunkook Lee, Dr. Juyoung Kim and Dr. Jiwha Lee from my home country.

I would like to give my sincere appreciation to my parent and sisters for their unconditional love and support. Finally, I deeply appreciate my two daughters, Yewon and Yejin for giving me happiness and my wife, Yoonkyong for her continual encouragement and support.

TABLE OF CONTENTS

page

ACKNOWLEDGMENTS iv

LIST OF TABLES ix

LIST OF FIGURES x

ABSTRACT xvi

CHAPTER

1 INTRODUCTION 1

2 LITERATURE REVIEW 5

- 2.1 Introduction 5
- 2.2 Low Temperature Synthesis of Powder Phosphors 6
- 2.3 Field Emission Display (FED) Phosphors 7
  - 2.3.1 Status of Field Emission Displays (FED) 7
  - 2.3.2 Problems of FED Phosphors 9
  - 2.3.3 Luminescence Quenching at High Excitation Densities 11
- 2.4 Activator Interactions 12
  - 2.4.1 Optical Transitions 12
  - 2.4.2 Multipolar Resonant Energy Transfer and Interaction Quenching 13
- 2.5 Surface Modification of Powder Phosphors 15
  - 2.5.1 Reduction of Degradation 15
  - 2.5.2 Improvement of Cathodoluminescent (CL) Efficiency 16
- 2.6 Characteristics of Nanoparticles 17
  - 2.6.1 Quantum Confinement 17
  - 2.6.2 Interactions between Nanoparticles 18
  - 2.6.3 Effects of Large Surface Area on Material Properties 20
- 2.7 Applications of Nanoparticles 20
  - 2.7.1 Nanoparticle Phosphors 20
    - 2.7.1.1 Developments of nanophosphors 20
    - 2.7.1.2 Importance of surfaces in nanoparticle phosphors 21
    - 2.7.1.3 Cathodoluminescence from nanoparticle phosphors 23
    - 2.7.1.4 Luminescence properties from ZnO nanoparticles 23
  - 2.7.2 Nanoparticles as Luminescence Sensitizer 24
    - 2.7.2.1 Energy transfer from embedded nanoparticles to activators 24

2.7.2.2 Nanoparticle embedding 26

3 COMBUSTION SYNTHESIS OF Eu^{3+}, Tb^{3+} and Tm^{3+} Doped Ln_2O_2S (Ln = Y, La, Gd) PHOSPHORS 30

3.1 Introduction 30
3.2 Experimental Section 30
3.2.1 Combustion Synthesis of Rare Earth Element doped Ln_2O_2S 30
3.2.2 Characterization 31
3.3. Result and Discussion 32
3.3.1 Morphology and Structure of as-Synthesized Powders 32
3.3.2 Effect of Fuel to Oxidizer Ratio on as-Synthesized Powders 33
3.3.3 Oxidation Stability of as-Synthesized Powders 34
3.3.4 Effect of Water on Combustion Reaction 34
3.3.5 Luminescence from Eu^{3+}, Tb^{3+} and Tm^{3+} doped Ln_2O_2S 35
3.3.6 Comparison with Commercial Phosphors 37
3.3.7 Effect of Grinding and Heat Treatment 37
3.4 Conclusion 39

4 TEMPORAL LUMINESCENCE QUENCHING FROM Eu^{3+} DOPED La_2O_2S 53

4.1 Introduction 53
4.2 Experimental Section 53
4.3 Results 55
4.3.1 Effect of Time, Temperature and Current Density on CL Intensities 55
4.3.2 Effect of Current Density on $^5D_1/^5D_0$ Peak Height Ratios 55
4.3.3 Effect of Surface Potential on $^5D_1/^5D_0$ Peak Height Ratios 56
4.3.4 Effect of Electon Beam Energy on $^5D_1/^5D_0$ Peak Height Ratios 56
4.3.5 Effect of Eu^{3+} Concentration on $^5D_1/^5D_0$ Peak Height Ratios 57
4.4 Discussion 57
4.4.1 CL Quenching at High Electron Beam Current Densities 57
4.4.1.1 Thermal quenching by electron beam heating 57
4.4.1.2 Temporal CL quenching from induced internal electric fields 60
4.4.2 Effect of Electron Beam Energy on Temporal CL Quenching 64
4.4.3 Enhanced Activator Interaction by Induced Internal Electric Fields 66
4.5 Conclusion 70

5 EFFECTS OF ENERGY FEEDING AND FUNNELING ON PEAK HEIGHT RATIOS $^5D_J/^5D_0$ FROM CATHODOLUMENSCENC OF $Ln_2O_2S:Eu^{3+}$ (Ln = La, Gd) 84

5.1 Introduction 84
5.2 Experimental Section 85
5.3 Results and Discussion 86
5.3.1 Temporal CL Quenching at Lower Eu^{3+} Concentration 86
5.3.1.1 Feeding from a higher to lower excited states 88
5.3.1.2 Competing process: feeding vs. funneling 89

5.3.2 Thermal versus Activator Interaction Quenching 91
5.4 Conclusion 93

6 EFFECTS OF COATINGS ON TEMPORAL CATHODOLUMINESCENCE QUENCHING IN ZnS:Ag,Cl PHOSPHORS 104

6.1 Introduction.. 104
6.2 Experimental Section.. 105
6.2.1 Surface Modification of ZnS:Ag,Cl Phosphors...................................... 105
6.2.2 Characterization... 105
6.3 Results and Discussion 106
6.3.1 Morphology and Luminescence of Oxides Coated ZnS:Ag,Cl 106
6.3.2 Temporal CL Quenching from Oxides Coated ZnS:Ag,Cl 107
6.3.3 Effects of Induced Internal Electric Fields and Surface Voltages........... 110
6.3.4 Effects of Nonradiative Surface Centers 113
6.3.5 Nonradiative Surface Recombination under Internal Electric Fields...... 116
6.4 Conclusion 119

7 ENHANCED GREEN EMISSION FROM ZnO NANOPARTICLES BY SURFACE SEGREGATION OF Mg.. 130

7.1 Introduction.. 130
7.2 Experimental Section.. 131
7.2.1 Synthesis of Nanoparticles: ZnO and ZnO with Mg.............................. 131
7.2.2 Characterization... 132
7.3 Results and Discussion 132
7.3.1 Formation and Growth of Suspended Nanoparticles.............................. 132
7.3.2 Surface Segregation of Mg on ZnO Nanoparticles 134
7.3.3 Effects of Mg Surface Segregation on Luminescence from Suspended ZnO Nanoparticles 136
7.3.3.1 Stability of green emission.. 136
7.3.3.2 Red shift of green emission and band filling................................ 137
7.3.4 Emissions from Powdered ZnO Nanoparticles 140
7.3.4.1 Effect of Mg surface segregation on the luminescence................. 140
7.3.4.2 Effect of excitation energy and precipitation medium on the luminescence... 141
7.4 Conclusions.. 143

8 ENHANCED LUMINESCENCE FROM $SiO_2:Eu^{3+}$ BY EMBEDDING OF ZnO NANOPARTICLES.. 157

8.1 Introduction.. 157
8.2 Experimental section... 158
8.2.1 *Ex situ* Embedding of ZnO Nanoparticles into $SiO_2:Eu^{3+}$....................... 158
8.2.2 Characterization... 159
8.3 Results and Discussion 159
8.3.1 Luminescence from ZnO Nanoparticles Embedded in SiO_2.................. 159

8.3.2 Luminescence from ZnO Nanoparticles Embedded SiO_2:Eu^{3+} 161
8.3.2.1 Enhanced emissions from SiO_2:Eu^{3+} by embedding of ZnO nanoparticles 161
8.3.2.2 Effect of Eu^{3+} and ZnO concentration on PL enhancement 162
8.4 Conclusions 164

9 CONCLUSIONS AND FUTURE WORK 170

9.1 Conclusions 170
9.1.1 Combustion Synthesis of Eu^{3+}, Tb^{3+} and Tm^{3+} Doped Ln_2O_2S (Ln = Y, La, Gd) Phosphors 170
9.1.2 Temporal Cathodoluminescence Quenching from Eu^{3+} Doped La_2O_2S . 171
9.1.3 Effects of Energy Feeding and Funneling on Peak Height Ratios $^5D_J/^5D_0$ from Cathodoluminescence of Ln_2O_2S: Eu^{3+}(Ln = La, Gd) 172
9.1.4 Effects of Coatings on Temporal Cathodoluminescence Quenching in ZnS:Ag,Cl Phosphors 173
9.1.5 Enhanced Green Emission from ZnO Nanoparticles by Surface Segregation of Mg 174
9.1.6 Enhanced Luminescence from SiO_2:Eu^{3+} by Embedding of ZnO Nanoparticles 175
9.2 Future Work 175

LIST OF REFERENCES 177

BIOGRAPHICAL SKETCH 187

LIST OF TABLES

Table page

4-1. Characteristics of region I, II, and III 72

6-1. Properties of coating materials 120

LIST OF FIGURES

Figure page

2-1. Optical properties of CdSe NC. (a) Energy diagram of CdSe NC versus NC diameter. (b) Blue shift in the absorption edge for a homologous size series of CdSe NC dispersions at RT [MUR00]. 28

2-2. Luminescent properties of CdSe NC. PL spectra for dispersed NCs of 82% 37.5 Å (small) and 18% 62 Å (large) CdSe at RT (a), and close-packed into a glassy solid at RT (b) under the excitation at 2.762 eV. Dotted lines show PL for isolated small (label A) and large (label B) NC solids under the excitation at 2.762 eV and at 2.143 eV [KAG96]. 29

3-1. X-ray diffraction pattern of as-synthesized La_2O_2S:Eu (3.2 mole %) powder prepared by combustion reaction with dithiooxamide (F/O = 2.0). The peak location and identification agrees with that of JCPDS #27-263 for La_2O_2S. 41

3-2. Morphology of as-synthesized La_2O_2S:Eu (1 mole %) powder prepared by combustion reaction with dithiooxamide (F/O = 2.0). (Scale bar: 10 μm for (a), 2 μm for (b)) 42

3-3. Morphology of ground La_2O_2S:Eu (1 mole %) powder prepared by combustion reaction with dithiooxamide (F/O = 2.0). (Scale bar: 5 μm) 43

3-4. The effect of fuel (dithiooxamide) to oxidizer (F/O) ratio on the formation of Y_2O_2S and Y_2O_3 prepared by combustion reaction with $Y(NO_3)_3$, $Tb(NO_3)_3$ and dithiooxamide The weight loss was measured using thermogravimetric analysis (TGA). The peak location and identification of X-ray diffraction patterns agree with that of JCPDS #24-1424 for Y_2O_2S and #25-1200 for Y_2O_3. 44

3-5. Cathodoluminescence (2 kV, 30 $\mu A/cm^2$) spectrum of powder after heat-treatment at 600 °C for 30 min. in air. The as-synthesized powders, Y_2O_2S and Y_2O_3, were from the combustion reaction with $Y(NO_3)_3$, $Eu(NO_3)_3$ and dithiooxamide (F/O = 1.6) with an Eu content of 3.2 mole %. 45

3-6. X-ray diffraction pattern of as-synthesized powder prepared by a combustion reaction of $La(NO_3)_3$, $Eu(NO_3)_3$ and dithiooxamide(F/O = 2.0) with water intentionally added. The peak location and identification agrees with that of JCPDS #27-263 for La_2O_2S and #16-1501 for $La_2O_2(SO_4)$. 46

3-7. Cathodoluminescence spectra from La_2O_2S:Eu (0.5 mole %) and Gd_2O_2S:Eu (0.5 mole %) measured at 2 kV and 30 μA/cm^2. 47

3-8. Cathodoluminescence spectra from Gd_2O_2S:Tb (0.2 mole %) and Y_2O_2S:Tb (0.2 mole %) measured at 2 kV and 20 μA/cm^2. 48

3-9. Cathodoluminescence spectrum from La_2O_2S:Tm (3.2 mole %) measured at 2 kV and 20 μA/cm^2. 49

3-10. The CL emission intensity (2 kV, 30 μA/cm^2) from the $^5D_0 \Rightarrow {}^7F_2$ electronic transition of La_2O_2S:Eu phosphor and the peak intensity ratio D_1/D_0 (see text) observed from La_2O_2S:Eu phosphor as a function of Eu concentration. 50

3-11. Relative efficiency and the ratio of the relative efficiencies of combustion prepared phosphors (1 mole %) to that of commercial phosphors for Gd_2O_2S:Tb as a function of electron beam energy (20 μA/cm^2). 51

3-12. Photoluminescence spectra of "as-synthesized ", "as-synthesized and heat-treated", "ground" and "ground and heat-treated" La_2O_2S:Eu (1.0 mole %) powder phosphors (λ_{exc} = 325 nm). The heat treatment was at 900 °C for 60 min in Ar. 52

4-1. Cathodoluminescence spectrum of $La_2O_2S:Eu^{3+}$ (0.5 mole %) measured at 2 kV and 50 μA/cm^2. 73

4-2. Emission intensity versus time or current density. (a) The temporal behavior of emission from the $^5D_0 \Rightarrow {}^7F_2$ transition of $La_2O_2S:Eu^{3+}$ (0.5 mole %) excited by a 2 kV electron beam. (b) The initial and steady state emission intensity from the $^5D_0 \Rightarrow {}^7F_2$ transition of $La_2O_2S:Eu^{3+}$ (0.5 mole %) as a function of electron beam current density with a 2 kV electron beam. 74

4-3. Temperature dependence of the $^5D_0 \Rightarrow {}^7F_2$ transition from $La_2O_2S:Eu^{3+}$ (0.5 mole %). (2 kV, 75 μA/cm^2) 75

4-4. Peak height ratio versus time or current density. (a) The temporal behavior of peak height ratio $^5D_1/^5D_0$ observed from $La_2O_2S:Eu^{3+}$ (0.5 mole %) phosphor with a 2kV electron beam. (b) The initial (t = 0) and steady state peak height ratio $^5D_1/^5D_0$ observed from $La_2O_2S:Eu^{3+}$ (0.5 mole %) as a function of electron beam current density at 2 kV. 76

4-5. Auger electron spectra of $La_2O_2S:Eu^{3+}$ (0.5 mole %) phosphor measured at position A, B and C. (2 kV, 60 μA/cm^2) The correspondent steady state peak height ratio $^5D_1/^5D_0$ is 0.52 at B and 0.56 at C. 77

4-6. Peak height ratio versus electron beam energy. (a) The initial (t = 0) and steady state $^5D_1/^5D_0$ peak height ratio observed from $La_2O_2S:Eu^{3+}$ (0.5 mole %) as a function of electron beam voltage at 135 μA/cm^2. (b) The steady state $^5D_1/^5D_0$ peak height ratio observed from $La_2O_2S:Eu^{3+}$ phosphor as a function of electron beam energy at 30 $\mu A/cm^2$. 78

4-7. Steady state peak height ratio versus current density. (a) The steady state $^5D_1/^5D_0$ peak height ratio observed from $La_2O_2S:Eu^{3+}$ (0.5 mole %) phosphor as a function of electron beam current density. The electron beam voltage was 2 kV. (b) The steady state $^5D_1/^5D_0$ peak height ratio versus electron beam current density. The electron beam voltage was 2 kV and Eu concentrations were 0.5, 1.0 or 2.5 mole %. 79

4-8. The steady state peak height ratio $^5D_1/^5D_0$ observed in $La_2O_2S:Eu^{3+}$ phosphor as a function of Eu concentration. (CL condition: 2 kV, 30 $\mu A/cm^2$, PL condition: $\lambda_{ex} =$ 325nm from He-Cd laser) 80

4-9. The quenching ratio, F, observed from $La_2O_2S:Eu^{3+}$ (0.5 mole %) as a function of electron beam current density at 2 kV. These ratios were calculated from data in Fig. 4-2(b). 81

4-10. The estimated intensity corrected for thermal quenching from the $^5D_0 \Rightarrow ^7F_2$ transition from $La_2O_2S:Eu^{3+}$ (0.5 mole %) as a function of electron beam current density at 2 kV 82

4-11. Schematic of charge distribution and internal electric field in Eu^{3+} doped La_2O_2S phosphor during electron beam bombardment. 83

5-1. Cathodoluminescent spectra from $La_2O_2S:Eu^{3+}$ (0.5 mole %) and $Gd_2O_2S:Eu^{3+}$ (0.5 mole %) measured at 2 kV and 30 $\mu A/cm^2$. 95

5-2. Temporal CL quenching factors versus electron beam current densities for the $^5D_0 \Rightarrow ^7F_2$ (626 nm) or $^5D_1 \Rightarrow ^7F_3$ (591 nm) transition of $La_2O_2S:Eu^{3+}$ (0.1 mole %) measured at 2 kV. 96

5-3. The initial ($t = t_{ini}$) and steady ($t = t_{quench}$) state peak height ratio, $^5D_1/^5D_0$, observed from $La_2O_2S:Eu^{3+}$ (0.1 mole %) as a function of electron beam current density at 2 kV. 97

5-4. The initial ($t = 0$) and steady ($t = t_{quench}$) state peak height ratios, $^5D_1/^5D_0$ and $^5D_2/^5D_0$, observed from $Gd_2O_2S:Eu^{3+}$ (0.4 mole %) as a function of electron beam current density at 2 kV. 98

5-5. A schematic diagram of activator interaction between an excited and ground state Eu^{3+} activator. The markers, * and **, show the energy states of activators after interaction. 99

5-6. The steady state peak height ratio, $^5D_1/^5D_0$, versus Eu^{3+} concentration observed from $La_2O_2S:Eu^{3+}$ at 2 kV and 22 ~ 176 $\mu A/cm^2$. 100

5-7. Temperature dependence of the steady state peak height ratio, $^5D_1/^5D_0$ and $^5D_2/^5D_0$, from $Gd_2O_2S:Eu^{3+}$ (0.4 mole %). (2 kV, 15 $\mu A/cm^2$) 101

5-8. The steady state peak height ratio, $^5D_1/^5D_0$ and $^5D_2/^5D_0$, observed from $Gd_2O_2S:Eu^{3+}$ (0.5, 1.5 and 2.5 mole %) as a function of electron beam current density at 2 kV.102

5-9. Temperature dependence of the initial and steady state peak height ratio, $^5D_1/^5D_0$, from $La_2O_2S:Eu^{3+}$ (0.5 mole %). (2 kV, 143 $\mu A/cm^2$).. 103

6-1. Schematic diagrams showing emission intensities versus time at low and high excitation density (left) and temporal CL quenching behavior (right)................. 121

6-2. A SEM image of SiO_2 (130 nm sized) coated ZnS:Ag,Cl powder phosphors. (Scale bar: 10 μm).. 121

6-3. Cathodoluminescence (2 kV and 70 $\mu A/cm^2$) and photoluminescence ($\lambda_{exc} = 325$ nm) spectra of non-coated and SiO_2 (130 nm sized) coated ZnS:Ag,Cl powder phosphors.. 122

6-4. Emission intensity from non-coated ZnS:Ag,Cl versus time or current density. (a) The temporal behavior of emission from non-coated ZnS:Ag,Cl powder phosphors after incidence of a 2 kV DC electron beam. Each current density was 72 or 564 $\mu A/cm^2$. (b) The initial and steady state emission intensity from non-coated ZnS:Ag,Cl powder phosphors as a function of electron beam current density. The electron beam energy was 2 kV. 123

6-5. Emission intensity from coated ZnS:Ag,Cl versus time or current density. (a) The temporal behavior of emission from SiO_2 (130 nm sized) coated ZnS:Ag,Cl powder phosphors after incidence of a 2 kV DC electron beam. Each current density was 72 or 564 $\mu A/cm^2$. (b) The initial and steady state emission intensity from SiO_2 (130 nm sized) coated ZnS:Ag,Cl powder phosphors as a function of electron beam current density. The electron beam energy was 2 kV. 124

6-6. Temporal quenching factors versus current density. (a) Temporal quenching factors versus current density of non-coated and SiO_2 (130 nm sized) coated ZnS:Ag,Cl powder phosphors. (b) Temporal quenching factors versus current density of ZnS:Ag,Cl coated with SiO_2 (22 nm nanoparticles), SnO_2 or Al_2O_3, and commercial ZnS:Ag,Cl phosphors coated with SiO_2 (produced by Kasei). 125

6-7. A schematic diagram of charging and induced internal electric field during electron beam bombardment. 126

6-8. The initial and steady state emission intensity and peak shift of S Auger electron at each coulombic load (2 kV, 330 $\mu A/cm^2$). For the measurement of temporal emission behaviors, an electron beam was shortly turned off during electron beam irradiation on SiO_2 (130 nm sized) coated ZnS:Ag,Cl powder phosphors. 127

6-9. CL (E_b = 1 and 4 kV) and PL (λ_{exc} = 335nm) decay curves of non-coated and SiO_2 (130 nm sized) coated ZnS:Ag,Cl powder phosphors. (left: CL at 1 kV, middle: CL at 4 kV , right: PL)........ 128

6-10. Temporal CL quenching and Auger electron spectra of heat-treated phosphors. (a) Temporal quenching factors versus current density of non-coated ZnS:Ag,Cl powder phosphors, which were heat-treated at 300 °C or 500 °C for 3 hr in air. The electron beam energy was 2 kV. (b) Auger electron spectra of non-coated ZnS:Ag,Cl powder phosphors, which were heat-treated at 300 °C or 500 °C for 3 hr in air. The electron beam energy was 2 kV. (left: Zn, middle: S, right: O) 129

7-1. Optical absorption spectrum of ZnO nanoparticles suspended in ethanol and corresponding plot of $[\mathrm{Ln}\ (1\text{-}A/I_0)]^2$ versus wavelength. The latter plot allows determination of the optical bandgap. 146

7-2. Bandgap energy (E_g) or corresponding wavelength (λ_g) versus aging time (t_a) of suspended nanoparticles of ZnO and ZnO:MgO........ 147

7-3. X-ray diffraction patterns from powdered (precipitated with heptane) nanoparticles of ZnO, ZnO:MgO, and micron-sized ZnO phosphors. 147

7-4. High resolution transmission electron microscope images and selected area diffraction patterns of ZnO nanoparticles. 148

7-5. FT-IR spectra from powdered nanoparticles of ZnO and ZnO:Mg,, and micron-sized ZnO phosphors. 149

7-6. Chemical composition of ZnO:MgO. EDS spectrum (a) and AES spectrum (b) from powdered nanoparticles of ZnO:MgO........ 150

7-7. PL emission spectra from suspended nanoparticles of ZnO and ZnO:MgO, excited by 325nm UV photons from a HeCd laser. (aging time = 29 days for (a), 138 days for (b)). 151

7-8. PL properties versus aging time. (a) Intensity ratio of UV to green emission (I(UV)/I(green)) from suspended ZnO nanoparticles versus aging time. (b) Intensity of green emission peak from ZnO divided by that from ZnO:MgO versus aging time. (c) Peak wavelength of green emission from suspended nanoparticles of ZnO and ZnO:MgO versus aging time........ 151

7-9. Schematic diagram showing the effects of non-radiative centers and the various filling levels of radiative centers on the intensity and peak wavelength of green emission........ 152

7-10. PL properties of powdered nanoparticles. PL emission (a) and PLE excitation (b) spectra from powdered nanoparticles of ZnO and ZnO:MgO precipitated using heptane........ 153

7-11. PL properties of micron-sized ZnO. PL emission (a) and PLE ecxitation (b) spectra from micron-sized ZnO phosphors.. 154

7-12. PLE spectra from suspended nanoparticles of ZnO and ZnO:MgO...................... 155

7-13. PL spectra for three different excitation energies from powdered ZnO nanoparticles that were precipitated by heptane.. 155

7-14. PL and PLE spectra from powdered ZnO nanoparticles that were precipitated by water. (a) PL spectrum from 325 nm excitation, (b) PLE spectrum for 570 nm emission, (c) PL spectrum from 395 nm excitation, (d) PL spectrum from 415 nm excitation, (e) PLE spectrum for 475 nm emission, and (f) PLE spectrum from 507 nm emission.. 156

8-1. FT-IR spectra from ZnO nanoparticle powders and from ZnO embedded in SiO_2 (Zn:Si = 1:9). The coincidence between the Zn-O stretching frequency demonstates that ZnO embedded in SiO_2 as nanoparticles.. 165

8-2. PL properties of embedded ZnO. PL emission (a) and excitation (b) spectrum from ZnO nanoparticles embedded SiO_2 166

8-3. PL emission spectra from SiO_2:Eu^{3+} and ZnO nanoparticle embedded SiO_2:Eu^{3+} after calcining at 500°C. (λ_{ex} = 325 nm) Note the lack of green emission from ZnO... 167

8-4. PL excitation spectra from SiO_2:Eu^{3+} and ZnO nanoparticle embedded SiO_2:Eu^{3+} after calcining at 500°C. (λ_{em} = 612 nm)... 167

8-5. Schematic diagram of ZnO nanoparticles embedded in SiO_2:Eu^{3+} 168

8-6. Emission intensities (at 612 nm) from SiO_2:Eu^{3+} (5 mole %) versus concentration of embedded ZnO nanoparticles.. 168

8-7. Possible luminescent mechanisms for ZnO nanoparticle embedded SiO_2: Eu^{3+}..... 169

Abstract of Dissertation Presented to the Graduate School
of the University of Florida in Partial Fulfillment of the
Requirements for the Degree of Doctor of Philosophy

EFFECTS OF EXCITATION DENSITY AND ENERGY TRANSFER ON CATHODOLUMINESCENCE FROM POWDER PHOSPHORS WITH AND WITHOUT EMBEDDED NANOPARTICLES

By

Jungsik Bang

August 2004

Chair: Paul H. Holloway
Major Department: Materials Science and Engineering

The intensity of cathodoluminescence (CL) from combustion synthesized $Ln_2O_2S:Eu^{3+}$ and nano-particulate oxide coated ZnS:Ag,Cl micron-sized powder phosphors was studied. In addition, the intensity of photoluminescence (PL) from nanometer-sized ZnO coated with MgO or embedded in $SiO_2:Eu^{3+}$ was studied.

Eu^{3+}, Tb^{3+}, or Tm^{3+} doped Ln_2O_2S (Ln = La, Y, or Gd) crystalline powders were prepared in air by combustion reactions between mixed metal nitrate and $(CSNH_2)_2$ (ignition temperatures of 300 ~ 350 °C). As-synthesized powders were agglomerants with 100 ~ 200 nm primary particles that exhibited characteristic emissions from Eu^{3+}, Tb^{3+}, or Tm^{3+} without additional heating.

For combustion synthesized $La_2O_2S:Eu^{3+}$ (0.5 mole %) powders, it was shown that CL intensities from the $^5D_1$ ($^5D_1 \Rightarrow {}^7F_3$) and $^5D_0$ transition ($^5D_0 \Rightarrow {}^7F_2$) and their ratio (designated $^5D_1/^5D_0$) decayed over the first ~ 5 sec. of DC electron beam irradiation at a higher current density (e.g., 2 keV, 500 $\mu A/cm^2$). Temporal CL quenching could not be

completely explained by thermal quenching from electron beam heating or by surface voltage changes due to charging. Instead, it was postulated that the primary electron beam induced internal electric fields, which were significant at higher excitation densities and resulted in local redistribution of charge carriers. Carrier redistribution led to enhanced activator interactions with temporal quenching and color change.

In addition, the $^5D_1/^5D_0$ ratio increased and then decreased for both $La_2O_2S:Eu^{3+}$ (0.1 mole %) and $Gd_2O_2S:Eu^{3+}$ (0.4 mole %) as the current density was increased from 10 towards 1000 $\mu A/cm^2$. These effects were shown to be consistent with the feeding from the higher $^5D_2$ excited state to the lower $^5D_1$, resulting in an increase of the $^5D_1/^5D_0$ ratio at low current densities. At higher current densities, energy was funneled from the $^5D_1$ to $^5D_0$ states, resulting in a decrease of the $^5D_1/^5D_0$ ratio.

In contrast to non-coated ZnS:Ag,Cl powder phosphors, ZnS:Ag,Cl coated with SiO_2 (22 or 130 nm), SnO_2 or Al_2O_3 showed a decrease of CL intensity over the first ~ 15 sec. of electron beam irradiation at higher current densities (e.g., 300 ~ 800 $\mu A/cm^2$). This temporal CL quenching of coated ZnS:Ag,Cl was postulated to result from a large concentration of non-radiative surface centers generated during surface modification of the phosphor, and from localization of generated electrons at the surface due to induced internal electric fields. These effects resulted in increased non-radiative surface recombination between electrons and holes and CL quenching.

The effects of Mg addition on the emission of green photons from ZnO nanoparticles ranging in size from 3 to 16 nm were studied. EDS and AES data demonstrated that ZnO nanoparticles with surface segregation of Mg (ZnO:MgO) were precipitated from colloidal reactions between Zn^{2+}, Mg^{2+} and OH solutions in EtOH. The PLE and PL spectra showed stronger green emission from suspended nanoparticles and dried powder of ZnO:MgO versus ZnO (3 ~ 13 times, and 20 times, respectively). ZnO:MgO also exhibited small red shift with aging. It was postulated that the presence of MgO on the surface of ZnO prevented aggregation via electrostatic stabilization in the suspension and also prevented formation of surface non-radiative recombination states, resulting in stabilized emission from ZnO. The red shift of the green emission peak from suspended ZnO versus aging times was discussed in terms of the filling of radiative surface trap states in the bandgap. The luminescent properties of ZnO were a dramatic function of the precipitation medium (e.g., heptane and water).

Enhanced luminescence from SiO_2:Eu^{3+} phosphor was demonstrated when ZnO nanoparticles was embedded. The characteristic f-f emissions from Eu^{3+} was enhanced by 5 ~ 10 times. The PLE spectra showed that the enhanced luminescence resulted from energy transfer from embedded ZnO nanoparticles to the Eu^{3+} activator ions. In addition, the energy transfer was shown to be dependent on the Eu^{3+} and ZnO concentrations.

CHAPTER 1
INTRODUCTION

The competitive development of display and lighting devices today requires luminescent materials with high efficiency and stability. In addition, small (< 5 μm), uniform and spherical phosphor powders are required for high resolution displays. It is difficult to control the morphology of phosphor powders commercially produced by solid state reactions due to the high temperatures. In addition, the conventional solid state reaction phosphor synthesis techniques are time consuming, requiring multiple steps such as blending, calcination, washing, milling, classification, filtering, drying and sieving. Several direct phosphor synthesis techniques have been studied to overcome these disadvantages. Combustion synthesis is especially attractive due to direct crystallization of small particles, a low process temperature, and less time consumed. Combustion synthesis has been used primarily to produce complex oxide phosphors, even though higher luminescence efficiencies are observed from sulfide or oxy-sulfide phosphors. In chapter 3, low temperature direct combustion synthesis of oxysulfide phosphors is reported with a general formula of $Ln_2O_2S:RE^{3+}$ (where Ln = Y, La, Gd and RE = Eu, Tb, Tm).

Due to the large size and weight of cathode ray tubes (CRTs), development of flat panel displays (FPDs) is of interest. Among several FPD technologies, liquid crystal displays (LCDs), plasma display panels (PDPs) and organic emissive displays (OEDs) are now commercially available in the FPD market. Another FPD technology, field emission displays (FEDs), is still under development because there are several problems in commercialization. FEDs are based on cathodoluminescence, similar to CRTs, but need a higher current density (75 ~ 100 mA/cm^2 per pulse) due to a lower operating voltage (below 2 kV). As a result, FED phosphors lose efficiency from a number of problems that occur at high excitation densities, such as degradation and luminescence quenching. Even though there are many reports of a decreased CL efficiency with increased current density at high (e.g., > 10 kV) or low (e.g., < 5 kV) electron energies, the mechanisms that lead to CL quenching at high current densities are only poorly understood. While the decay or rise times for CL peaks, ranging from nsec to msec in principle give information about the CL saturation mechanisms, variations of CL luminescence over several hours or longer generally result from degradation. In chapter 4, the temporal CL quenching behavior of $La_2O_2S:Eu^{3+}$ powder phosphors prepared by combustion reaction is reported and discussed. CL decay over the first several seconds of electron beam irradiation versus excitation density, i.e., temporal quenching, is reported and interpreted in terms of emission intensity of $^5D_j{=>}^7F_j$ electronic transitions and peak height ratio of the $^5D_1{=>}^7F_3$ to $^5D_0{=>}^7F_2$ (designated $^5D_1/^5D_0$ ratio) from Eu. The effects of Eu concentration, primary beam energy and current density upon the cathodoluminescent (CL) intensity and color from $La_2O_2S:Eu^{3+}$ are discussed based on the thermal quenching by electron beam heating, surface voltage by charging, and enhanced activator interaction due to induced internal electric fields. In chapter 5, the effects of excited state densities and temperature on the temporal quenching of the $^5D_2{=>}^7F_3$, $^5D_1{=>}^7F_3$ and $^5D_0{=>}^7F_2$ cathodoluminescent transitions from $Ln_2O_2S:Eu^{3+}$ (Ln = La or Gd) are reported. The simultaneous effects of current density and Eu^{3+} concentration on the energy feeding and funneling between excited states (i.e., ^5D_j) are analyzed in terms of peak height ratios, $^5D_2/^5D_0$ and $^5D_1/^5D_0$. In addition, the effects upon CL quenching of temperature versus activator interactions are discussed.

Surface modification of powder phosphors has been used to improve their properties for commercial display and lighting devices. In particular, surface modifications have been studied to reduce degradation or improve CL efficiency at low voltages. In chapter 6, the effects of coatings on the temporal CL quenching of ZnS:Ag,Cl powder phosphors versus current densities are reported and discussed. CL brightness versus time (i.e., temporal CL quenching) from powder phosphors of ZnS:Ag,Cl coated with SiO_2 (22 or 130 nm nanoparticles), SnO_2 or Al_2O_3 are compared to those from non-coated phosphors, and discussed based on non-radiative surface centers and localization of electrons at the surface due to primary beam-induced internal electric fields.

Higher luminescence efficiencies from nano-sized versus micron-sized phosphors have been reported and suggest a new approach for FED phosphors with low CL efficiency at low voltages. However, the higher luminescent efficiencies from nano-sized phosphors still need to be proven and mechanisms developed to explain the improvements. The effects of large surface area on the luminescent efficiencies and defect emission from nanoparticles also need to be studied. Green emission from ZnO is known to be defect emission from radiative oxygen vacancies, which are naturally present on the large surface area of nanoparticles and may lead to larger efficiencies for ZnO nanoparticles. To achieve this larger efficiency, surface segregation of elements (e.g., Mg), or even creations of a surface shell layer (e.g., MgO) over a core of ZnO may quench non-radiative surface states. In chapter 7, the formation of ZnO:MgO core/shell-type nanoparticles is shown to result in surface passivation. In addition, a red shift of suspended ZnO nanoparticle emission peaks versus aging times is discussed in terms of filling of radiative surface trap states (i.e., oxygen vacancies) over a range of energies in the bandgap. The effects of precipitation by heptane versus water on the luminescence from powdered ZnO nanoparticles are shown to be dramatic and due to differences in surface passiavation and defects.

Finally in Chapter 8, energy transfer between nanoparticles and activator ions will be shown to provide another way to improve luminescence, especially photoluminescence. The effects of embedded nanoparticles (i.e., they acted as luminescence sensitizers) on luminescence from Eu^{3+} activator ions in a SiO_2 host matrix are reported. In this system, the ZnO nanoparticles do not emit visible photons but do help activator ions to emit more photons. In addition, the effects of Eu^{3+} concentration (e.g., 1 vs. 5 mole %) and amounts of embedded ZnO nanoparticles (e.g., 5 ~ 20 mole %) on energy transfer from embedded ZnO nanoparticles to Eu^{3+} are discussed.

CHAPTER 2
LITERATURE REVIEW

2.1 Introduction

Luminescent materials are the main components of display and lightening devices and are commercially produced by solid state reactions. In order to overcome the problems in the conventional process, low temperature synthesis has been studied. In subhead 2.2, the characteristics and methods for low temperature synthesis, especially combustion methods, are reviewed. Low voltage phosphors are the main components for the successful commercialization of Field Emission Displays (FEDs) and the characteristics of phosphors at low voltages and high current densities have been studied. In subhead 2.3, the characteristics and status of FEDs are reviewed with an emphasis on the problems of FED phosphors. Previous results for luminescence quenching at high excitation densities are also discussed. In order to reduce problems with FED phosphors, surface modification of powder phosphors have been studied. In the subhead 2.4, the effects of coatings on the reduction of degradation and enhancement of CL efficiency are reviewed. Activator interactions are one of the reasons for luminescence quenching and result in emission color changes. The principles and effects of activator interaction are reviewed in subhead 2.5. Nanoparticles have been the focus of several studies due to their unique properties, with special emphasis on new approaches for the enhancement of luminescence efficiency. In subhead 2.6 and 2.7, the basics of nanoparticles, including quantum effect, energy transfer between nanoparticles and surface passivation, are introduced. In addition, nanoparticles as emitting materials and luminescence sensitizers are reviewed.

2.2 Low Temperature Synthesis of Powder Phosphors

Phosphor powders are commercially produced by solid state reactions. Their synthesis involves several process steps such as raw material blending, high temperature calcination, washing, milling, classification (control of particle size), filtering, drying and sieving [JUS98, SHI98]. Also, a surface modification step may be added for a particular application. Conventional phosphor synthesis techniques could be improved by elimination of time consuming multiple steps and the need for high temperatures. Uniform, spherical phosphor powders favored in the screening process are desirable for high quality display devices. However, it is difficult to control the morphology of phosphor powders using high temperature solid state reactions. To achieve high resolution displays, small (< 5 μm) phosphor powders are needed. Grinding is required for this purpose because larger sized particles generally result from solid state reactions. However, grinding generally degrades luminescent efficiencies due to the introduction of surface defects that act as non-radiative recombination sites. Therefore, direct phosphor synthesis techniques overcoming the disadvantages of high temperature solid state reaction have been studied, such as combustion synthesis [BAC00, RAV99, SHE96], spray pyrolysis [KAN99], sol-gel methods [RAO96, RAV97, RUA98], co-precipitation methods [IHA02, MA97], and solvo-thermal methods [YU99].

Combustion synthesis is attractive due to direct crystallization of small sized particles, low process temperature, and reduced time consumption. During the exothermic decomposition of metal nitrates and organic fuel complexes at low temperature, sufficient heat is generated locally to form crystalline materials [SHE96]. This combustion synthesis has been used to produce complex oxides such as $Y_3Al_5O_{12}:Cr^{+3}$ [SHE96], $Y_3Al_5O_{12}:Tb^{+3}$ [SHE97], $Y_3Al_5O_{12}:Eu^{+3}$ [SHE97], $Y_3Al_5O_{12}:Tm^{+3}$ [LOP97], $Y_3Ga_5O_{12}:Tb^{+3}$ [SHE97], $Y_2O_3:Eu^{+3}$ [KOT96, SHE97], $(Gd,Y)_2O_3:Eu^{+3}$ [SUN00], $Y_2SiO_5:Ce^{+3}$ [SHE96], $CeMgAl_{11}O_{19}:Tb^{+3}$ [RAV99], $BaMg_2Al_{16}O_{27}:Eu^{+2}$ [BAC00, PAT97], $YAlO_3:Tb^{+3}$ [KIM01] and $BaMgAl_{10}O_{17}:Eu^{+2}$ [PAT97].

2.3 Field Emission Display (FED) Phosphors

2.3.1 Status of Field Emission Displays (FED)

Due to the large size and weight of cathode ray tubes (CRTs), developments of flat panel displays (FPDs) are of interest. Among several FPD technologies, liquid crystal displays (LCDs) already dominate the FPD market and plasma display panels (PDPs) are now commercially available in the large area TV market [BRO01, NOR02, POO01, WER01]. Recently, there has been excellent progress in improved performance of organic emissive displays (OEDs) [HAC02]. OEDs are now used in small area applications such as mobile phones, personal communication devices and automobile displays. Another FPD technology, field emission displays (FEDs), is still under development by Sony [BRO01, WER01], although there are several problems in commercialization, including poisoning of the cathodes and low efficiency phosphors [HOL99, HOP00, REU01].

FEDs offer a wider viewing angle (~ 170 °), faster response, higher tolerance to temperature and radiation, and sometimes lower power consumption when compared to LCDs. FEDs operate based on cathodoluminescence, similar to CRTs, but with very different architecture. The FED consists of an array of emitter tips that excite a phosphor screen. Due to close cathode-anode spacing (< 0.2 ~ 2 mm), the FED typically operates at a voltage below that of CRT (e.g., 0.5 ~ 10 vs. 15 ~ 30 kV) [TAL01]. FEDs are classified as low voltage (< 2 kV) or high voltage (2 ~ 10 kV) devices. At present, only two companies, the French based Pixtech and the Japanese based Futaba, are producing low voltage FEDs (LVFED) for commercial consumption [TAL01]. The products targeted by these companies constitute small volume, highly specialized applications, where FEDs have a distinct advantage in performance to LCDs and where the cost premium due to the small scale production of the FEDs is not a factor. Recently, the " Thin-CRT$^{\text{TM}}$," a high voltage FED (HVFED), was developed by Candescent [HOP00]. However, the FED development has slowed down due to several commercialization problems.

LVFEDs are simpler to fabricate than HVFEDs because they do not require the additional features intended to handle the high anode voltage across the narrow vacuum gap. Therefore, LVFED prototypes were the first to appear at trade shows and have entered into a commercial production phase. Although the future use of monochrome LVFEDs is likely to grow to some extent, application of this technology beyond instrumentation is unlikely unless highly efficient, full color low-voltage phosphors are developed. Despite on-going research on low-voltage phosphor development, presently no suitable candidates are available with the required brightness and color coordinates.

Despite the complicated fabrication process, every FED company has been pursuing a high voltage design. This decision was based on the premise that the challenges of fabricating HVFEDs with commercially available phosphors were less severe than those posed by the advent of synthesizing new phosphors for LVFEDs. In addition to readily available phosphor materials, HVFEDs approach offers other important advantages over the LVFED, such as lower power consumption, improved beam focusing, lower gate voltage, longer phosphor life, ability to use a reflective aluminum coating and larger anode-to-cathode gap [ITO00, TAL01]. However, the HVFED design requires a substantial increase in complexity of the display components in order to insure stable panel operation for many thousands of hours. The high anode voltage applied across a ~1 mm gap can cause both sudden catastrophic failures and a rapid decrease in emission current [REU01]. Typical catastrophic failures in HVFEDs include vacuum arcs across the anode-to-cathode gap, spacer flashover, and row-to-column burnout. These failure mechanisms, in addition to phosphor aging, limit the usable lifetime of the panel. While the solutions to several problems may not yet be optimal, high-quality high-voltage displays have been demonstrated by Candescent [HOP00] and Motorola [TAL01].

2.3.2 Problems of FED Phosphors

The screen prepared by fine grain powder phosphor has lower resolution due to light scattering on the particles and poor thermal conductivity associated with the small contact area between spherical particles. Due to these reasons, thin film phosphors were introduced [SEL82]. Also, thin film phosphors have a high contrast, long term operation, lower out-gassing [CHA97], low degradation due to small surface area and insensitivity to surface contamination. Furthermore, less saturation at high excitation densities is anticipated compared to powder phosphors. Therefore, various methods such as sputtering [MAP73, SEL82], sol-gel [CHO01, RAB87, RAV97], PLD [CHO98, CHO99, JON99], e-beam evaporation [NAK99], aerosol spray pyrolysis [GIB99] and liquid phase epitaxy [ROB80] were used for the deposition of luminescent thin films. However, the major disadvantage of thin film phosphor is low brightness compared to powder phosphors. Due to the light piping by the higher refractive index of the phosphor films causing a small critical angle for transmission, a large fraction of the radiation light is trapped internally [JON99, MAP73]. Various techniques were used in order to improve these phenomena. These techniques included using a segmented thin film by photolithography etching [MAP73], use of ground glass or Si substrate [CHO99, SEL82], surface roughing by introduction of a diamond buffer layer [CHO98] or nodular surface microstructure by controlling deposition conditions such as oxygen pressure [JON99]. However, to date, thin film phosphors have not shown comparable brightness of powder phosphor.

The low efficiency at low voltage is a common problem for powder and thin film phosphors. To date, it is uncertain as to why phosphors have low efficiency at low voltage [HOL99]. The lower efficiency is known to result from the reduced electron penetration depth and CL from the near surface which has a high density of non-radiative site. However, another reason is suggested, e.g., an enhanced interaction [SEA00a, SEA00b]. The density of electron-hole (e-h) pairs increases with decreasing electron beam energy due to electron penetration depth dependency on the electron beam energy. Therefore, the high e-h pair densities correspond to high densities of excited activators. This results in quenching due to ground state depletion or increased activator interactions.

Phosphor efficiency typically decreases faster than linear with a decrease of the operating voltage from 15~30 kV to 2 kV [HOL99]. For FEDs to achieve brightness comparable to CRTs, the power is increased at low voltage by increasing the current density. Generally, current density ranges from 75 ~ 100 mA/cm^2 per pulse in low voltage FEDs, and from 1~10 μA/cm^2 per pulse in high voltage FEDs [CHA97, ITO00]. As a result, FED phosphors suffer from a number of problems that occur at high excitation densities. It is known that the degradation of phosphors occurs at coulombic loads between 20 and 200 C/cm^2 [HOL00a]. Also, degradation of sulfide phosphors has been shown to occur via electron stimulated surface chemical reactions (ESSCR) between the phosphor and reactive residual vacuum gas molecules such as H_2O, CO_x, H_2, etc., with generation of volatile species such as SO_2 and H_2S [HOL00a]. Evolution of gases from the vacuum system walls and phosphors leads to poisoning of the field emitter tips. In addition to degradation, luminescence quenching may occur at high current densities. Quenching is defined as the reduction of phosphor efficiency with changes of operating parameters or time. It is known that the phosphor efficiency decreases with increasing temperature (thermal quenching) and increasing activator concentration (concentration quenching) [ITO00]. CL efficiency may decrease with surface charging of phosphors [ITO00, HOL00b, SEA97], which may occur due to the high resistance of the phosphor layer. Electron beam heating at high current densities can lead to thermal quenching, and high excitation densities can result in quenching due to saturation of luminescence.

2.3.3 Luminescence Quenching at High Excitation Densities

There are many reports related to the decrease of CL efficiency with increasing current density at high (e.g. > 10 kV) or low (e.g. < 5 kV) electron energies [DEL83, IMA80, KUB80, LEE98, MCC82, ROB76, STO00, YAN98a, YAN98b]. Phenomena that have been postulated to explain this decrease in efficiency include ground state depletion, activator interaction and thermal quenching. Mechanisms that lead to quenching of CL brightness at high current densities still lack for details. Robbins [ROB76] measured the luminescence spectra and the intensities of $^5D_j \Rightarrow {}^7F_j$ transitions from $Y_2O_2S:Eu^{3+}$ phosphor as a function of current density at 20 kV for powder phosphors. Also, photoluminescence (PL) was measured when an AC voltage was applied. The data suggested that saturated intensities could result from space charge field effects. Imanaga et al. [IMA80] also studied saturation effects in $Y_2O_2S:Eu^{3+}$ powder phosphor by measuring intensities and relaxation times from $^5D_j => ^7F_j$ transitions as a function of the intensity of a pulsed N_2 laser (337 nm) or pulsed electron beam (10 kV). They suggested that interactions between excited states of Eu^{3+} ions gave rise to an energy loss causing saturation. Tallant et al. [TAL02] measured the PL decay times of $^5D_j => ^7F_j$ as a function of Eu concentration in $Y_2O_3:Eu^{3+}$ powder phosphors and suggested that the dominant mechanisms for energy transfer and relaxation could change from sequential relaxation (multi-phonon relaxation) to first order interactions (interactions between excited and ground state activators), to second order activator interactions (interactions between excited state activators) with increasing activator concentration. They proposed that the efficiency of phosphors subjected to second order activator interactions (in phosphors having high activator concentrations) would decrease as the excitation intensity increased. Yang et al. [YAN98a] measured and calculated the efficiency of $Y_2O_3:Eu^{3+}$ powder phosphor versus current density at a low voltage (e.g., 2 kV). The saturation observed at high current densities was attributed to interactions between excited states of Eu^{3+} ions.

2.4 Activator Interactions

2.4.1 Optical Transitions

Optical transitions such as absorption and emission often result from the vibration of electronic dipole in the systems such as a molecule, atom and ion. These optical transitions are also expressed in terms of perturbations of the system energy by an electronic dipole moment in the presence of electromagnetic radiation (i.e., an electric dipole transition) [SHI98]. Optical transitions also result from higher order perturbations such as changes of magnetic dipole and electronic quadrupole moments [SHI98]. Eu^{3+} doped Ln_2O_2S (Ln = Y, La, Gd) phosphors show characteristic emission peaks, which correspond to f-f transitions such as magnetic dipole and forced electric dipole (due to forbidden transitions being allowed due to asymmetry) transitions. Among the characteristic emissions from Eu^{3+} are $^5D_0$=>$^7F_2$, $^5D_1$=>$^7F_3$, $^5D_2$=>$^7F_4$, and $^5D_3$=>$^7F_5$ transitions that correspond to forced electric dipole transitions [BLA94, SHI98]. The intensities from these transitions depend on the density of Eu^{3+} activators existing at each excited state, ^5D_j (j = 0, 1, 2, 3). Note that excited activators finally lose their energy via either radiative or non-radiative decay. The emission intensities are only proportional to the density of each exited state that results in a radiative decay, and information about non-radiative decay must be deduced or measured by other approaches.

When Eu^{3+} doped Ln_2O_2S (Ln = Y, La, Gd) is excited by an electron beam (EB), the density of each excited state depends on the crossover between the charge transfer level and each excited f level (^5D_j). This crossover position depends on the host material which causes different dependency of the ^5D_j emissions on temperature [FON70, STR70]. For example, emissions from the $^5D_2$ state of $La_2O_2S:Eu^{3+}$ are not observed at room temperature [FON66]. Also, the density of each excited state (^5D_j) is a function of the Eu^{3+} activator concentration due to the host-activator and activator-activator energy transfer efficiencies

2.4.2 Multipolar Resonant Energy Transfer and Interaction Quenching

An activator interaction is defined as the communication of energy directly between activator ions. Such interactions generally occur between a ground and an excited state activator, or between two activators in excited states. One activator (the donor) is de-excited (emission) while another activator (the acceptor) is excited (absorption). This is called a multi-polar resonant interaction or resonant energy transfer [UIT66] when there is overlap between the donor emission and acceptor absorption spectrum. Because multi-polar resonant interactions involve two optical transitions, they are classified into magnetic dipole-dipole (generally called an exchange energy transfer), electric dipole-dipole, electric dipole-quadrupole, and electric quadrupole-quadrupole interactions according to the characteristics of each optical transition. The donor activator transfers energy resonantly to the neighboring acceptor activator, which is generally in an excited state and ground state, respectively.

Forster [FOR48] and Dexter [DEX53, DEX54] developed the theoretical expressions for multi-polar resonant interaction. Multi-polar resonant interactions have been used to explain phenomena such as non-exponential luminescence decay, concentration quenching and sensitized luminescence [INO65, KUB96, OZA71, UIT66, UIT67a, UIT67b, ZIE72]. Generally, electric quadrupole-quadrupole, dipole-quadrupole and dipole-dipole, and magnetic dipole-dipole interactions act sequentially to quench the emission intensities from given manifold when the activator concentration is increased (i.e., with a decrease of the inter-activator distance). Based on the emission time-resolved decay and emission intensity versus Eu^{3+} concentration, energy transfer to neighboring activators from $^5D_0$, $^5D_1$, $^5D_2$, or $^5D_3$ states are known to result from magnetic dipole-dipole and electric dipole-dipole, dipole-quadrupole, or quadrupole-quadrupole interactions [OZA71, OZA90]. Emissions from higher excited states (e.g., $^5D_2$) showed faster quenching than lower excited states (e.g., $^5D_1$ or $^5D_0$) with an increase of activator concentration. This implies that the densities of higher excited states involved in radiative decay decrease faster than those of lower excited states when the activator concentration is increased.

2.5 Surface Modification of Powder Phosphors

Development of field emission displays (FEDs) has slowed due to several commercialization problems, including packaging, poisoning of the cathodes and selection of phosphors for the anode [HOL99]. In order to improve FED phosphors, two approaches have been studied. One is development of new phosphors having high cathodoluminescence (CL) efficiency at low voltages and high current densities, and the second is surface modification of phosphors to improve FED phosphor efficiency and maintenance.

Surface modification of powder phosphors has been used to improve their use in fluorescent lamps, cathode-ray tubes (CRT), and plasma display panels (PDP). For example, the surface of CRT phosphors is generally coated with iron oxide or cobalt aluminate for the improvement of contrast [SHI98]. In addition, colloidal silica, silicate, zinc oxide or phosphate is used to enhance the photosensitivity and adhesion on the glass panel during the CRT screening process [FEL00, MER00, SHI98]. Finally, surface modifications of FED phosphors have been studied to reduce degradation or improve CL efficiency at low voltages.

2.5.1 Reduction of Degradation

As stated above, degradation occurs via electron stimulated surface chemical reactions (ESSCR) and results in formation of non-luminescent surface layers accompanied by generation of defect centers and volatile species [HOL00a]. In addition, evolution of gases from the phosphors may lead to poisoning of field emitter tips [ITO00]. To reduce degradation from surface reactions, phosphors have been coated by $TaSi_2$ [FIT98], MgO

[LEE01, SOU00, THO02], ITO [KOM97, SOU00], phosphate [SOU00], SiO_2 [WAG00] and ZnO [IGA01]. Igarashi et al. [IGA01] reported that surface oxidation of ZnS:Ag,Cl phosphors was suppressed by ZnO nanoparticle coating due to increased electrical conduction and associated protection from local heating. Wagner et al. [WAG00] reported that SiO_2 coating on ZnS:Cu green phosphors resulted in improved degradation properties. However, Abrams et al. [ABR00] reported that SiO_2 promoted H_2 dissociation under electron beam bombardment and accelerated CL degradation of ZnS under reducing conditions.

2.5.2 Improvement of Cathodoluminescent (CL) Efficiency

It has been reported that CL efficiency decreases with surface charging, which may occur due to the high resistance of phosphor materials [ITO00]. Coating on phosphor surfaces with conductive layers has been studied to improve CL efficiency at low voltages. Kominami et al. [KOM97, KOM98] reported that In_2O_3 coating on ZnS:Ag,Cl phosphors improved CL efficiency under 500 eV electron beam irradiation, and that conducting layers eliminated charging based on measurement of surface potential. Lee et al. [LEE01] reported that coating materials changed the electron backscattering factor and subsequently increased CL efficiency of $Y_2SiO_5:Ce^{3+}$ phosphors coated with Si compounds. Wagner et al. [WAG00] reported that SiO_2 coatings passivated surface defects or resulted in free electrons/holes moving to the bulk with a subsequent increase in the CL efficiency of ZnS:Cu green phosphors. Bukesov et al. [BUK01, BUK02] reported that surface coating enhanced the luminescence efficiency of vacuum fluorescent display (VFD) phosphors, and explained this phenomenon by postulating and modeling an increased surface electric field with the subsequent motion of minority carriers (holes) into the bulk where the defect density and non-radiative recombination rate were lower. They postulated that re-adsorption of secondary electrons and development of a positive space charge resulted in the formation of a surface double layer with electric fields that could accelerate holes formed below the double layer toward bulk. In contrast, Souriau et al. [SOU00] reported that coating of MgO, In_2O_3 or polyphosphate on $SrGa_2S_4:Eu^{2+}$ or ZnS:Ag,Cl phosphors lowered the CL efficiency. Also, Thomes et al. [THO02] reported and modeled reduced CL intensities from MgO or Al_2O_3 coatings on $Y_2O_3:Eu^{3+}$ or $Y_2SiO_5:Tb^{3+}$

2.6 Characteristics of Nanoparticles

There has been increased interest in the scientific and technological aspects of nanometer-sized particles. These particles exhibit unique chemical and physical properties, differing substantially from those of the corresponding bulk solids. These differences are associated with the quantum confinement effect and existence of a relatively large percentage of atoms at the surface.

2.6.1 Quantum Confinement

Quantum confinement is known to be the influence of the quantum size on the electronic (e.g., band-gap shift) and vibrational (e.g., structural restriction of phonons) states [MUR93, MUR00]. Semiconductor nano-crystals (NC), smaller than the Bohr radius of the bulk exciton, strongly confine electronic excitations in all three dimensions. Photo-excitation of the NC creates an e-h pair that is confined to and delocalized over the volume of the NC. The photo-physical properties of the NC are analogous to those of a large molecule. Three-dimensional confinement effects collapse the continuous density of states of the bulk solid into the discrete electronic states of the NC. The finite size of the NC quantizes the allowed k (wave number) values. Decreasing NC diameter shifts the first state to larger k values and increases the separation between states. This is observed spectroscopically for a series of CdSe NC samples as a blue shift in the absorption edge and a larger separation between electronic transitions with decreasing NC diameter [EFR96, MUR00, MUR03]. Figure 2-1 shows those behaviors. In the case of metal NCs, the continuous density of electronic states is also broken up into discrete energy levels.

As the size of metal NCs decreases to length scales smaller than the wavelength of incident radiation, a surface plasmon resonance develops. For noble metals, it lies within the visible [MUR00]. The surface plasmon resonance is a dipolar excitation of the entire particle between the negatively charged free electrons in the NC and its positively charged core. The energy of the surface plasmon resonance depends on both the free electron density and the dielectric medium surrounding the NC.

2.6.2 Interactions between Nanoparticles

Coupling between transition dipoles is known to occur when an excited NC is placed in the near field of a ground state NC. At inter-particle separations between 5 and 100 Å, dipole-dipole interactions lead to electronic energy transfer, also known as long-range resonance transfer (LRRT) [KAG96]. LRRT is a radiation-less energy transfer process that arises as resonant transition dipoles in an excited NC and a ground state NC couple through their generated electromagnetic fields. This coupling causes the excitation in the excited NC (donor of the excitation) to be transferred to the ground state NC (acceptor of the excitation), with return of the excited NC to its ground state and promoting the ground state NC to a higher excited state. The discrete optical absorption and sharp band-edge emissions are characteristic of the size-dependent, quantized electronic transitions for CdSe NC samples dispersed in solution. For individual NCs in the solids, the absorption spectra remain unchanged. However, the emission spectra for close-packed and dispersed NCs differ and can be understood by accounting for energy transfer between NCs in the solids. Fig.2-2 shows the variation of emission intensity in dispersed and close packed NCs [KAG96]. For LRRT to occur and be observed, two conditions must be satisfied. The acceptor must have a transition in resonance with the energy of donor emission and a lower energy state in which the transferred excitation could be trapped. Once the transferred excitation is trapped (at rates of typical vibrational relaxation) in the lower energy states of the acceptor, the excitation cannot be transferred back because the donor is transparent to the lower energy excitation. In a mixed solid, the PL quantum yield (QY) for the small NCs is quenched and the PL QY for large NCs is enhanced when exciting both small and large NCs [CRO02, KAG96]. These observations are signatures of electronic energy transfer from the small to the large NCs in the close-packed NC solid.

As the distance between NCs is reduced to separations of 5 Å, exchange interactions become significant. As the distance between CdSe NCs is reduced, from 7 to 0 Å, the optical absorption spectrum red shifts and approaches the absorption spectrum for bulk CdSe [MUR00]. The strength of the interaction is the same as in the bulk. Electronic excitations are delocalized over many NCs or many unit cells in bulk CdSe. The organic ligands coordinating the metal NCs in the solids mediate electronic coupling between NCs and therefore the properties of the solids. At inter-particle distances of 5 Å, exchange interactions and electronic delocalization become significant. From the study of preparing and compressing monolayers of alkanethiol-capped Ag NCs, it is reported that there is an insulator-to-metal transition as the distance between metal NCs is decreased [MUR00].

2.6.3 Effects of Large Surface Area on Material Properties

In nanoparticles, the quality of the surfaces or interfaces and their influence on the physical properties still present a major concern. The large fraction of surface atoms leads to the existence of a large number of dangling bonds or external defects. These play a key role in structural transformations, solubility, melting point of the materials, localization of carriers and light emission processes.

For example, XRD studies of ZnS NCs show a significant reduction in the zinc-blende (cubic) to wurtzite (hexagonal) phase transition temperature (~ 400 °C), as compared to the bulk value (~ 1020 °C) [QAD99]. The particles also show some lattice distortion with decreasing particle size. There is also a monotonic reduction in the specific volume as the particle size decreases from about 240 Å (500°C) to about 30 Å (27°C) [QAD99].

2.7 Applications of Nanoparticles

2.7.1 Nanoparticle Phosphors

2.7.1.1 Developments of nanophosphors

Nano-particles highlight the new developments in luminescence materials for lighting and displays. The effect of quantum confinement on the impurity was studied for the first time in ZnS : Mn^{+2} NCs, which resulted in high luminescent efficiency and a shortening of the radiative lifetime to nanosecond range [BHA94]. These results were explained on the basis of hybridization of the s-p electrons and holes with the localized d-states of the Mn^{+2}. Additionally, the large changes in the luminescent decay time was attributed to a relaxation in the selection rules for the internal d-d transition of Mn^{+2} from forbidden to allowed [BHA94]. Since this report, considerable attention has been paid to optical properties of doped NCs. In the case of $ZnS:Tb^{+3}$ and $ZnS:Eu^{+3}$ NC, the decay time of glass coated NC was reported to be at least one order of magnitude shorter than that of the bulk sample. The photoluminescent intensities of these NCs were reported to be about three times higher than those of bulk phosphors [IHA02].

However, there were controversies related to nanosecond order decay time of $ZnS{:}Mn^{+2}$. From lifetime measurements and time-resolved spectroscopy, it was concluded that the Mn^{+2} emission in $ZnS{:}Mn^{+2}$ NC did not show a shortening of the decay time upon decreasing particle size. The nanosecond decay times reported for the Mn^{+2} emission were most likely due to the tail of broad defect related ZnS emissions which overlaps with the Mn^{+2} emission at around 590 nm [BOL00].

Tanaka et al. [TAN00a] reported that the temperature quenching of the $ZnS{:}Mn^{2+}$ NCs was much weaker than that of the bulk powder under inter-band excitation. Several causes for this difference were suggested. First, the excitons (e-h pairs) in the NC cannot be thermally dissociated because of the spatial confinement, unlike the excitons in the bulk crystal. Second, the interaction of the excitons with phonons in the NC is weaker than that in the bulk crystal. And last, the energy transfer from the excitons to Mn^{2+} in the NC is faster than that in the bulk crystal. The similar effect was reported in $CdS{:}Mn^{2+}$ [TAN00b].

2.7.1.2 Importance of surfaces in nanoparticle phosphors

In NCs, the rate of non-radiative recombination of e-h pairs at the surface is believed to be very high due to the large surface to volume ratio. However, there were many reports in which ZnS:Mn NCs are more efficient compared to bulk crystals [BHA94]. It may depend on surface passivation. It was reported that the brightness of ZnS:Mn NCs in colloids were enhanced several times by the presence of surfactants [CHU95]. Therefore, nanoparticles are generally prepared with a capping agent in colloidal solutions or embedded in solid and transparent media, such as glasses and polymers. Stabilizing agents must be present during growth to prevent aggregation and precipitation of the NCs. When the stabilizing molecules are attached to the NC surface as a monolayer through covalent or ionic bonds, they are referred to as capping groups [BHA94]. These capping groups serve to mediate NC growth, sterically stabilize NCs in solution, and passivate surface electronic states in semiconductor NCs. As stated above, several studies showed an attempt to passivate the surface of colloidal nanoparticles by disordered organic capping. However, this still leaves unsaturated bonds and sensitivity to photo-oxidation. Therefore, epitaxial hetero-structure of nanoparticles has been studied.

Methods for overcoating a semiconductor NC with a second semiconductor material of wider band-gap are well developed. For example, CdSe NCs have been overcoated with ZnS, ZnSe and CdS, which resulted in dramatic improvements in luminescence efficiency [ROD97]. The quantum yield of CdSe quantum dots, as prepared, is about 10 ~ 15 % with the yield typically being limited by the existence of surface defects, which lead to non-radiative pathways for the electron-hole pair recombination. Solution chemistry growth of a thin ZnS overlayer on the surface of the CdSe particles passivates the defects and raise the quantum yield to values between 40 ~ 50 % for the particles ranging in size from 2 ~ 6 nm in diameters. Also, the ZnS matrix is deposited by OMCVD from diethyl zinc and hydrogen sulfide while the NCs are delivered to the film surface by electro-spray. The ZnS shell provides electronic and chemical passivation of the CdSe core improving its luminescence and thermal stability. The variation in the PL wavelength is caused by alterations (i.e., alloying) of the NCs due to heating during thin film synthesis [HEI98]. CL and PL are dominated by the sharp band edge emission. The emission wavelength can be tuned in a broad window (470 ~ 650 nm) by varying the size of the dots. The CL intensity is known to depend on the crystallinity of the ZnS matrix and the voltage and current density applied [ROD97].

In addition, embedding in the solid media diminishes the surface reactivity of a nanoparticle and supplies a stable chemical environment. However, the nanoparticles still consist of large surface and interface areas that influence the electronic properties of the materials.

2.7.1.3 Cathodoluminescence from nanoparticle phosphors

Even though there have been many studies related to doped NC phosphor, few CL studies have been reported. ZnS:Mn^{+2} NC with a thin layer of ZnO around the particles was reported to have 40 % efficiency of a commercial micron-sized phosphors when the electron beam energy ranged between 500 and 3500 eV [DIN99]. The NCs also exhibited less current saturation than micron-sized phosphors. The fact that the nanoparticles exhibit less current saturation than micron-sized phosphors is an important feature for the use in FEDs.

Ihara et al. [IHA02] reported that glass ingredients enhanced luminescence and reduced phosphor degradation under bombardment of electron-beams. Glass coated ZnS:Tb^{+3} and ZnS:Eu^{+3} NCs showed ten times higher CL than those of uncoated NCs and appeared to be protected from surface oxidation.

2.7.1.4 Luminescence properties from ZnO nanoparticles

Among the nano-sized semiconductor materials, ZnO nanoparticles have been studied for the application of photo catalyst, chemical sensors and phosphors [LOO01], and usually prepared from hydrolysis of Zn ion with NaOH or LiOH in non-aqueous solvent such as ethanol and i-propanol [MEU98, MON98, WON98]. ZnO NC without capping agents showed dominant green emission [DIJ00], while ZnO NC with capping agents showed dominant UV emission [GUO00, MAH99]. Mahamuni et al. [MAH99] reported dominant UV emission at 378 nm from TOAB capped ZnO, and Guo et al. [GUO00] showed PVP passivation on ZnO NC to enhance UV emission and diminish green emission.

Even though many results have been reported on emissions from ZnO, emission mechanisms still lack understanding, especially those related to green emission. An UV emission near 385 nm results from exciton recombination such as free exciton and bound exciton, and their phonon-replica [BAG98, REY97, SHI98], and is observed at room temperature due to high exciton binding energy (~ 59 meV) [SHI98]. In contrast, green emission ranging from 490 ~ 600 nm has been reported to be from defects involving $V^+(O)$. Vanheusden et al. [VAN96] showed an increase of the green emission intensity with an increase of the electron paramagnetic resonance (EPR) signal of $V^+(O)$ and suggested emission to be from recombination of electrons captured in $V^+(O)$ with captured hole in shallow levels near the valance band. In contrast, Dijken et al. [DIJ00, DIJ01] reported the red shift of green emission with an increase of particle size and suggested green emission was from recombination of holes captured by $V^+(O)$ with captured electron in shallow level near the conduction band. In addition, they reported quantum efficiency for green emission from uncapped ZnO decreased from 20 % at 7 Å to 12 % at 10 Å.

2.7.2 Nanoparticles as Luminescence Sensitizer

2.7.2.1 Energy transfer from embedded nanoparticles to activators

The development of field emission displays has slowed down due to several commercialization problems such as sudden catastrophic failures, rapid decrease in emission current and availability of phosphors [REU01, HOP00]. Among the several problems with phosphors (e.g., degradation, saturation and temporal CL quenching at high excitation density, light piping in thin film phosphor, and low efficiency at low voltage) [HOL99], a low efficiency at low voltage is a critical issue which prevents successful commercialization of FEDs, especially low voltage FEDs (LVFED).

It has been reported that the quantum efficiency of nano phosphors is higher than that of bulk phosphor [BHA94]. This suggests a new direction for developments of full color FEDs in which commercialization has been slowed due to low efficiency phosphors at low voltages. In fact, NC phosphors that are passivated by inorganic materials show higher CL efficiency when compared to bulk sized phosphors [DIN99]. However, it is anticipated that there is a difficulty for making full color screen using NC phosphor due to re-aggregation, cross contamination and residue that occur in the screening process. In addition, the higher efficiency of NC phosphor is not confirmed and depends on surface passivation. Nano composites (i.e., phosphors embedded in a transparent matrix) can be used as alternatives for CL phosphors. But this method has the disadvantage of a small luminescent volume to incident electron beam due to small loading quantities for nano phosphors in sol-gel films.

The fact that a nano-particle transfers energy to another nano-particle via electronic interaction (e.g., long range resonance transfer) [KAG96] suggests another way to improve the luminescence, especially photoluminescence. Nanoparticles could behave like sensitizers (donor) or activators (acceptor) in a host matrix (e.g., sol-gel thin film). This energy transfer mechanism is very similar to energy transfer between activator ions in a host matrix. Thus, nano-particles could also transfer energy to activator ions in a host matrix or vice versa. Therefore, luminescence from activator ions in a host matrix could increase by embedding nano-particles into the host matrix with activators.

It has been reported that an increase in the emission intensities from Eu^{3+} or Tb^{3+} doped sol-gel ZrO_2 thin film occurs when CdS NCs are co doped [REI00]. This is explained by energy transfer from CdS NCs to activator ions. It is also suggested that PL intensity increases due to the segregation of Eu^{3+} or Tb^{3+} at the interface between NC and matrix. But, direct evidences such as photoluminescence excitation (PLE) have not been provided. Also, Tb_2S_3 NCs created in situ in sol-gel silica thin films are known to act as a good activator and sensitizer for radiative recombination of the sol-gel silica xerogel [YAN02]. From this, it is suggested that there is a sensitized energy transfer from Tb_2S_3 NCs to the sol-gel matrix.

Recently, it was reported that embedded Si nanoparticles played a role as sensitizers in the Er^{3+} doped SiO_2 thin films [FRA00, RAN01]. Si NCs were produced by high-temperature annealing of sub-stoichiometric SiO_x thin films grown by plasma enhanced chemical vapor deposition. Samples were subsequently implanted with Er^{3+} ion. From the photoluminescence of three different samples (Er and O implanted crystalline Si, Er implanted SiO_2, and Er implanted and Si NC embedded SiO_2), the emitting Er^{3+} ions in the Er implanted and Si NC embedded SiO_2 were shown to be in the SiO_2 or at the Si NC/SiO_2 interface.

2.7.2.2 Nanoparticle embedding

Several studies showed an attempt to passivate the surface of colloidal nanoparticles by disordered organic capping [CHU95, BHA94]. However, this still leaves unsaturated bonds and sensitivity to photo-oxidation. Therefore, embedding method has been used in order to diminish the surface reactivity of a nanoparticle and supply a stable chemical environment. Usually, nanoparticles were embedded in sol-gel glasses or polymers, [YAN02, TAN00a, TAN00b] and nanocomposites were prepared by sol-gel process due to the advantage of simple mixing or impregnation.

Up to now, sol-gel nano-composite coatings containing metal oxide particles and noble metal colloids are used for application where antireflective properties as well as electrostatic or electromagnetic wave shielding properties are important [UHL97]. In this sol-gel coating, sol-gel film was formed after mixing the precursor of SiO_2 sol with nano-particles prepared separately (*ex-situ* embedding). For example, many researchers have used Si alkoxide solution containing TiO_xN_y, TiO_2, Ta_2O_5, ZrO_2, ZnS, MgF_2, ATO, ITO, silver, copper and gold nanoparticles [ABE01, UHL97]. This method features high loading amounts of NCs in a sol-gel matrix. Due to the difficulties of homogeneous dispersion, an in-situ embedding method has recently been used [GOR97, ZEL01]. In this method, nanoparticles are formed with the sol-gel matrix at the same time.

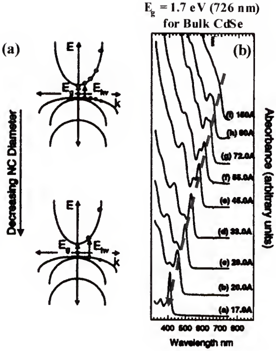

Figure 2-1. Optical properties of CdSe NC. (a) Energy diagram of CdSe NC versus NC diameter. (b) Blue shift in the absorption edge for a homologous size series of CdSe NC dispersions at RT [MUR00].

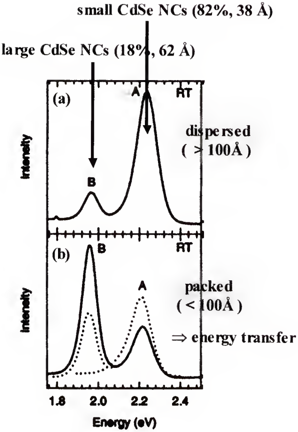

Figure 2-2. Luminescent properties of CdSe NC. PL spectra for dispersed NCs of 82% 37.5 Å (small) and 18% 62 Å (large) CdSe at RT (a), and close-packed into a glassy solid at RT (b) under the excitation at 2.762 eV. Dotted lines show PL for isolated small (label A) and large (label B) NC solids under the excitation at 2.762 eV and at 2.143 eV [KAG96].

CHAPTER 3
COMBUSTION SYNTHESIS OF Eu^{3+}, Tb^{3+} AND Tm^{3+} DOPED Ln_2O_2S (Ln = Y, La, Gd) PHOSPHORS

3.1 Introduction

Although sulfide or oxy-sulfide phosphors generally have higher luminescence efficiencies compared to oxide phosphor, there are few reports of their preparation by combustion reactions. Mishenina et al. reported the self-propagating synthesis of rare earth oxy-sulfide phosphors such as $Y_2O_2S:Eu^{3+}$ and $Y_2O_2S:Tb^{3+}$ using rare earth oxide and sulfidizing agents [MIS94]. In this work, low temperature direct synthesis of phosphors with the general formula of $Ln_2O_2S:RE^{3+}$ (where Ln = Y, La, Gd and RE = Eu, Tb, Tm) are reported using combustion reactions with metal nitrate and sulfur containing organic fuels.

3.2 Experimental Section

3.2.1 Combustion Synthesis of Rare Earth Element doped Ln_2O_2S

Powder phosphors of $(Y_{1-x}RE_x)_2O_2S$, $(La_{1-x}RE_x)_2O_2S$, and $(Gd_{1-x}RE_x)_2O_2S$ where RE = Eu^{3+}, Tb^{3+}, or Tm^{3+}, and x ranges from 0.0005 to 0.032 were prepared by combustion reactions. The reactants consisting of $Y(NO_3)_3$-$6H_2O$ (Alfa, 99.99+% purity), $La(NO_3)_3$-$6H_2O$ (Aldrich, 99.999+% purity), $Gd(NO_3)_3$-$6H_2O$ (Aldrich, 99.999+% purity), $Eu(NO_3)_3$-$6H_2O$ (Alfa, 99.99+% purity), $Tb(NO_3)_3$-$6H_2O$ (Aldrich, 99.999+% purity), or $Tm(NO_3)_3$-$5H_2O$ (Aldrich, 99.9+% purity) were dissolved in water and mixed in stoichiometric amounts. Due to their low melting point, the metal nitrates were molten during drying in an oven at 100 °C. During cooling of the mixed metal nitrate reactants, the appropriate amounts of organic fuel, such as dithiooxamide ($(CSNH_2)_2$, Aldrich, 98+% purity) were added, mixed and ground along with the nitrates. The organic fuel to oxidizer (metal nitrate) ratio was controlled by varying the amount of fuel added. After a 24 hr dehydration step in a desiccator, the mixtures were heated in an air tube furnace to the ignition temperature of $T_i = 300 \sim 350$ °C. During heating, there was a decomposition reaction to form precursors. Due to the large amounts of heat that were released from the exothermic reaction between the metal nitrates and fuel, the reactants were locally heated to a high temperature that was called the flame temperature, T_f, and the metal oxysulfide rapidly formed. After the combustion reaction, the powder product was gently crushed with an alumina mortar and pestle. To evaluate the effects of heat treatment, the combustion prepared powders were also heated to 500 ~ 700 °C in air or to 900 °C in Ar (99.999+% purity).

3.2.2 Characterization

The combustion synthesized powders were characterized by X-ray diffraction (XRD) using a Philips Model APD 3720 diffractometer with Cu Kα radiation, by thermogravimetric analysis (TGA) using a Netzsch Model STA 449C, by scanning electron microscopy (SEM) using a JEOL model 6400, by photoluminescence (PL) using a HeCd laser (325 nm) and monochromator/PMT, and by cathodoluminescence (CL) using a Kimball Physics electron gun and Ocean optics S2000 fiber optic spectrometer with a CCD array detector in a vacuum demountable test system.

3.3. Result and Discussion

3.3.1 Morphology and Structure of as-Synthesized Powders

As shown in Fig.3-1, the XRD pattern from as-synthesized Eu doped La_2O_2S powder combusted with dithiooxamide was that from hexagonal La_2O_2S with lattice constants of a = 0.4047 nm and c = 0.6944 nm (JCPDS #27-263). No other phases were detected. The combustion reaction to synthesize crystalline $(Ln_{1-x}RE_x)_2O_2S$ powders can be written as:

$$a[(1\text{-}x)Ln(NO_3)_3 + xRE(NO_3)_3] + b[(CSNH_2)_2] \Rightarrow a/2[(Ln_{1-x}RE_x)_2O_2S] + \text{by-products}$$

where b/a = fuel to oxidizer molar ratio (F/O). The powder shown in Fig.3-1 was synthesized with a F/O = 2.0.

Both low and high magnification scanning electron microscope (SEM) images of as-combustion synthesized $La_2O_2S{:}Eu^{+3}$ powders are shown in Fig.3-2.(a) and (b), respectively. Similar to previous reports [LOP97, RAV99, SHE97], the powder morphology consisted of a foamy, porous agglomerated continuous three-dimensional network. The pores are probably due to the rapid release of gaseous by-products. Particle growth was hindered presumably because evolved gases rapidly transport heat and quench the temperature. Therefore, small primary particles agglomerated to form a porous interconnected network. The agglomerates ranged in size between 10 μm and 30 μm, while the primary particles ranged in size between 100 nm and 200 nm. The SEM image of powders, which were ground with a mortar and pestle in ethanol for 5 min, is shown in Fig.3-3. The large agglomerates easily fractured down to small 1 ~ 2 μm diameter agglomerates.

3.3.2 Effect of Fuel to Oxidizer Ratio on as-Synthesized Powders

The XRD patterns for as-combusted powder prepared from $Y(NO_3)_3$ and $Tb(NO_3)_3$ with dithiooxamide (F/O = 1.0 ~ 2.0) showed that both Y_2O_2S and Y_2O_3 were produced by combustion. Figure 3-4 shows weight loss and the ratio of the intensity of the (101) Y_2O_2S peak to the sum of intensities of (101) Y_2O_2S and (222) Y_2O_3 peaks versus the fuel to oxidizer (F/O) ratio. The weight loss was measured using thermogravimetric analysis (TGA). At a F/O = 2.0, a crystalline Y_2O_2S single phase was obtained, but an amorphous black residue containing C, N, O, H and S, was also present. At a lower F/O ratio, less black residue were present, but the relative amount of crystalline Y_2O_3 phase increased. At a very low F/O ratio ~ 1.0, the intensity of the (222) Y_2O_3 peak was greater than the (101) Y_2O_2S peak, suggesting that Y_2O_3 was the dominant phase, and the black residue increased again. These data result from the fact that the F/O ratio affects the adiabatic flame temperature [SHE97], amount of carbon to form by-products such as amorphous black residue, and amount of sulfur available to form the metal oxy-sulfide. During the combustion reaction, a white smoke was generated, which is believed to be high molecular gaseous by-products containing C, N, O, H and S. These by-products could be oxidized to CO_x, SO_x, NO_x and H_2O in an adequate supply of oxygen and sufficiently high flame temperature. (e.g., F/O ~ 1.8) However, they could remain on the combustion synthesized phosphors as an amorphous black residue during cooling if the supply of carbon was high or the flame temperature was too low. (e.g., high F/O or low F/O, respectively) The presence of the Y_2O_2S phase and amorphous black residue at F/O = 2.0 shows that enough sulfur was supplied for the formation of Y_2O_2S, but that too much carbon was present and generated non-oxidized gaseous by-products. The presence of Y_2O_3 for $1.4 < F/O < 2.0$ is due to the quantity of sulfur being insufficient to form

Y_2O_2S, and the decrease of amorphous black residue is due to contents of carbon being oxidized. At a low F/O ratio (< 1.4), the amorphous black residue increased because the adiabatic flame temperature was too low to completely oxidize the carbon in the fuel. In contrast to yttrium, a crystalline La_2O_2S or Gd_2O_2S single phase formed with a negligible amorphous black residue from combustion reactions with a F/O = 2.0. The weigh loss from TGA measurement was below 1 wt %. Presumably these differences result from the dependence of the adiabatic flame temperature on the metal nitrate. (i.e., La, Gd, versus Y nitrate)

3.3.3 Oxidation Stability of as-Synthesized Powders

The XRD patterns showed that as-combusted oxysulfide powder (e.g., yttrium oxysulfide) was converted to oxysulfate (e.g., yttrium oxysulfate) after heat treatment at 600 °C for 30min in air. The presence of $Y_2O_2(SO_4)$ was confirmed by the CL spectrum (Fig.3-5) which shows peaks from $Y_2O_2S:Eu^{3+}$ (626 nm and 615 nm), $Y_2O_2(SO_4):Eu^{3+}$ (615 nm, 617 nm and 619 nm), and $Y_2O_3:Eu^{3+}$ (612 nm). Previous research has shown that Y_2O_2S and La_2O_2S are oxidized to oxysulfate ($Y_2O_2(SO_4)$ and $La_2O_2(SO_4)$) above 750 °C and to oxide (Y_2O_3 and La_2O_3) above 950 °C [HAY68, OZA77, TSA94]. Conversion to a oxysulfate at temperatures as low as 600 °C is thought to result from either the presence of some partly crystallized powders due to a rapid reaction, or the high surface area of the combustion synthesized material.

3.3.4 Effect of Water on Combustion Reaction

In order to maximize production of the oxysulfide host phase, de-hydration of the reactants was crucial. During heating to the ignition temperature, the hydrated water may be reduced, however complete removal is dependent on the amount of hydrated water and the gas flow rate. Hong et al. [HON94] reported that higher water content led to increased surface area of combustion synthesized powders. Because heat is required to vaporize water, less heat is available for particle growth, consistent with a large surface area. Shea et al. [SHE96] also reported that water increased the amount of crystalline Al_2O_3 formed in competition with YAG during a combustion reaction. To quantify the effects on combustion synthesis of metal oxysulfide, an amount of water equivalent to the amount of reactants was intentionally added to the combustion synthesis with a F/O ratio of 2. Comparison of XRD data in Fig.3-1 and Fig.3-6 show crystalline $La_2O_2(SO_4)$ formed with La_2O_2S upon addition of water. In other words, oxygen from water with a sufficient supply of sulfur favored the formation of La oxysulfate instead of oxide. As reported above, a low F/O ratio (deficiency of sulfur) with dry nitrates led to crystalline Y_2O_3 and Y_2O_2S phases. It is expected that hydrated reactants would lead to crystalline La_2O_3 and $La_2O_2(SO_4)$ (or Y_2O_3 and $Y_2O_2(SO_4)$) at a low F/O ratio.

3.3.5 Luminescence from Eu^{3+}, Tb^{3+} and Tm^{3+} doped Ln_2O_2S

The as-synthesized phosphor powders exhibited good cathodoluminescence (CL) and photoluminescence (PL) with a spectrum characteristic of the particular rare earth [ABD92, SHI98, STR70]. Fig.3-7, 3-8 and 3-9 show cathodoluminescent spectra of as-synthesized $Ln_2O_2S:Eu^{3+}$ (Ln = La, Gd), $Ln_2O_2S:Tb^{3+}$ (Ln = Gd, Y), and $La_2O_2S:Tm^{3+}$ phosphor powders measured at 2 kV and 30 $\mu A/cm^2$. As shown in Fig.3-7, the emission from the $^5D_2 \Rightarrow {}^7F_j$ transition was observed in $Gd_2O_2S:Eu^{3+}$ (0.5 mole%) but not in $La_2O_2S:Eu^{3+}$ (0.5 mole%). These results from the energy crossover between the f energy level and the charge transfer state (CTS) are consistent with previous results [FON66, STR70, STR71]. Fonger et al. [FON66] reported that no luminescence was found from

$^5D_2$ in $La_2O_2S:Eu^{3+}$ at room temperature due to thermal quenching of $^5D_2$ excited state and provided an explanation based on the configurational coordinate model. The host material affects the energy level of the CTS and its crossover with f energy level, suggesting change of the relative emission intensities with temperature and host. Similar phenomena were observed from Tb^{3+} doped phosphors. As shown in Fig.3-8, emission from $^5D_3 \Rightarrow {}^7F_j$ was observed in $Y_2O_2S:Tb^{3+}$ (0.2 mole %) but not in $La_2O_2S:Tb^{3+}$ (0.2 mole %). This observation is also consistent with previous results [SHI98, STR71]. In the case of $Ln_2O_2S:Tb^{3+}$ phosphor, it was reported that the relative intensity of $^5D_3$ emission increased dramatically as the lanthanide element was changed from La to Gd to Y to Lu. Multi-phonon relaxation and the crossover between the f energy level and the 4f-5d absorption energy level in the configurational coordinate model explains these observations on Tb^{3+} doped phosphors.

The emission intensity from the $^5D_0 \Rightarrow {}^7F_2$ transition of $La_2O_2S:Eu^{3+}$ is shown in Fig.3-10 along with the peak height ratio of D_1/D_0 transitions as a function of Eu^{3+} concentration in $La_2O_2S:Eu^{3+}$. The peak height ratio of D_1/D_0 was defined as the emission intensity from the $^5D_1 \Rightarrow {}^7F_3$ transition (at 587 nm) divided by the emission intensity from the $^5D_0 \Rightarrow {}^7F_2$ transition (at 626 nm). The emission intensity from the $^5D_0 \Rightarrow {}^7F_2$ transition exhibited a maximum at 0.5 mole % of Eu, consistent with previous reports [OZA90]. For $La_2O_2S:Eu^{3+}$ made by traditional solid state reactions, the optimum activator concentration was known to be about 0.5 ~ 1.0 mole %. The peak height ratio of D_1/D_0 decreased with increasing Eu^{3+} concentration due to concentration quenching [BLA94, OZA90].

3.3.6 Comparison with Commercial Phosphors

The relative CL efficiencies of $Gd_2O_2S:Tb^{3+}$ (1.0 mole %) produced by combustion reaction or of powders purchased from Osram Sylvania (type 2616, d = 7 μm) versus primary beam energy are shown in Fig. 3-11, along with the ratio of CL efficiencies for combustion versus the commercial phosphor. The efficiency of as-combusted, mildly ground (no anneal) phosphors was lower than that of commercial phosphors at all electron beam energies (30 to 15 % at 1 to 4 kV) and the ratio of efficiencies decreased with increasing electron beam energy. The decrease in ratio of efficiency with increasing electron beam energy may result from the small grain size (~ 100 nm) of combustion synthesized powders. The electron-hole pairs generated by incident electrons over the penetration range may diffuse outside this range and suffer non-radiative recombination at a boundary, surface or defect. For Gd_2O_2S, the penetration range may be calculated from $R_p = K(E_b)^a$ where K = 8.05 and a = 1.608 [YAN98a] and found to be ~ 100 nm at 5 kV. This range would allow many electrons to reach a grain or external boundary, and subsequently non-radiative surface recombination to increase with an increase of electron beam energy. Therefore, it is reasonable that the efficiency of phosphors with ~ 100 nm sized grains increase less with increasing electron beam energy compared to the commercial phosphors with large sized grains. In addition, since annealing has not been applied and the rare earth concentration has not been optimized contrary to the case of the commercial powders, CL efficiencies are considered to be encouraging.

3.3.7 Effect of Grinding and Heat Treatment

The PL spectra for combustion synthesized $La_2O_2S:Eu^{3+}$ (1.0 mole %) powders in the "as-synthesized", "as-synthesized and heat-treated", "ground" and "ground and heat-treated" conditions are shown in Fig. 3-12. Combustion synthesized powder phosphors were gently ground in an alcohol slurry by mortar and pestle for 5 min and/or heat treated at 900 °C for 60 min in Ar. While grinding reduced the PL intensities by about 43 % (compared to as-synthesized), heat treatment alone increased them about 40 %, and heat treatment after grinding increased them back to about the same as before grinding. In contrast to PL, neither grinding nor heat treatment at 900 °C had any effect on the CL intensities from these samples. In addition, the XRD FWHM data of (101) peak showed that grinding or heat treatment did not change crystallite size. The monochromatic excitation wavelength for PL was 325 nm and was near the reported value of the CTS energy level of Eu doped La_2O_2S (335 nm) [RED96]. In the case of CL, the main excitation route is known to be via the CTS [OZA81]. Therefore, the different results for PL and CL should not be due to different excitation routes (e.g., direct f-f excitation). Even though amorphous black residues were not visible in as-synthesized $La_2O_2S:Eu^{3+}$ powder, there was some color differences when compared to powders heat-treated at 900 °C for 60 min in Ar. These observations suggest that the effects of heat treatment on PL and CL intensities could be due to removal of a surface amorphous carbon layer, not annealing effects such as the removal of defects or improvement of the crystallinity. This suggestion is consistent with the lack of change in the XRD FWHM data. A small surface residue with appropriate functional groups capable of absorbing UV could lead to lower phosphor excitation in PL. Heat treatment to 900 °C could lead to removal of surface residues, improving PL intensities. Recovery of PL from ground phosphor by heat treatment could also result from removal of the surface residue. The reduction of PL intensity by grinding can be understood in terms of surface damage in combination with light scattering from small particles versus agglomerated powder. While surface damage acts as a luminescent quenching site, the disintegration of agglomerated powder modifies the scattering of incident UV or emitted light. However, surface damage is difficult to reconcile with the lack of change in the CL intensities and in the XRD FWHM of the (101) peak with grinding. If surface damage has large effects on luminescence, it should have greater influence on CL as compared to PL due to the shallow excitation depth of electron in CL. Therefore, the decrease of intensity observed only for PL suggests that the changes in the excitation light scattering process from grinding of the agglomerates are dominant. Differences in light scattering due to changes of particle size, size distribution, shape and the number of particle layers can affect the amount of incident light absorbed by the particles.

3.4 Conclusion

Powder phosphors of $(Y_{1-x}RE_x)_2O_2S$, $(La_{1-x}RE_x)_2O_2S$, and $(Gd_{1-x}RE_x)_2O_2S$, where RE = Eu^{3+}, Tb^{3+}, or Tm^{3+} and x ranges from 0.0005 to 0.032, were prepared by combustion reactions from mixed metal nitrate reactants and dithiooxamide ($(CSNH_2)_2$) organic fuel. The XRD pattern of as-synthesized powder revealed that the Ln_2O_2S (Ln = Y, La, and Gd) phase crystallized directly from the combustion reaction with various fuel to oxidizer ratios (typically F/O ~ 2.0) at ignition temperatures of 300 ~ 350 °C. Powders synthesized with a lower F/O ratio, especially for $(Y_{1-x}RE_x)_2O_2S$, were contaminated by residual carbonaceous material. De-hydration of the reactants was crucial for the successful synthesis of the oxysulfide phase. Intentionally added water with a sufficient supply of sulfur favored the formation of lanthanum oxysulfate instead of oxide. SEM images of as-synthesized powders showed that the morphology consisted of a foamy, porous agglomeration and a continuous three-dimensional network. The agglomerates ranged in size between 10 μm and 30 μm, while the primary particles ranged in size between 100 nm and 200 nm.

The phosphors prepared by combustion reaction were cathodoluminescent (CL) and photoluminescent (PL), exhibiting characteristic emission spectra of Eu^{3+}, Tb^{3+}, or Tm^{3+}. The emission intensity from the $^5D_0 \Rightarrow {}^7F_2$ electronic transition (at 626 nm) exhibited a maximum at 0.5 mole % of Eu^{3+}. The CL efficiency of as-combusted $Gd_2O_2S:Tb^{3+}$ phosphors was lower than that of commercial phosphors at all electron beam energies (30 to 15 % at 1 to 4 kV) and the ratio of efficiencies decreased with increasing electron beam energy. This ratio is considered to be good since the synthesis parameters for combustion synthesized phosphor were not optimized. While grinding and heat treatment (900 °C, Ar, 60 min) decreased and increased the PL intensity, respectively, the CL intensity was not changed by these treatments. Possible reasons for these observations were discussed.

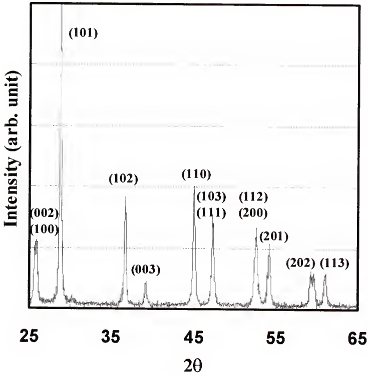

Figure 3-1. X-ray diffraction pattern of as-synthesized La_2O_2S:Eu (3.2 mole %) powder prepared by combustion reaction with dithiooxamide (F/O = 2.0). The peak location and identification agrees with that of JCPDS #27-263 for La_2O_2S.

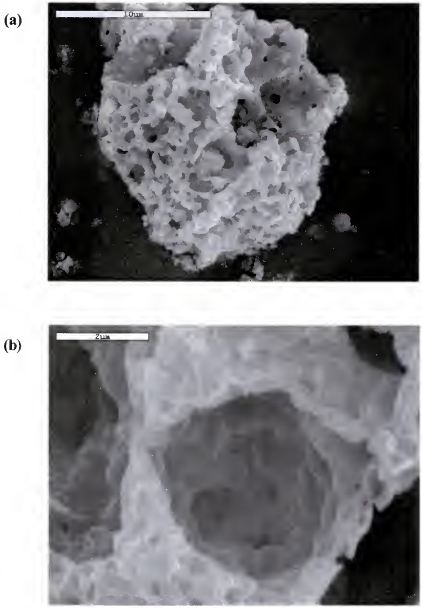

Figure 3-2. Morphology of as-synthesized La_2O_2S:Eu (1 mole %) powder prepared by combustion reaction with dithiooxamide (F/O = 2.0). (Scale bar: 10 µm for (a), 2 µm for (b))

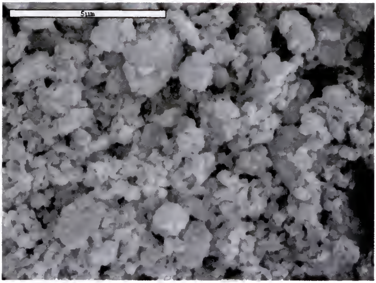

Figure 3-3. Morphology of ground La_2O_2S:Eu (1 mole %) powder prepared by combustion reaction with dithiooxamide (F/O = 2.0). (Scale bar: 5 µm)

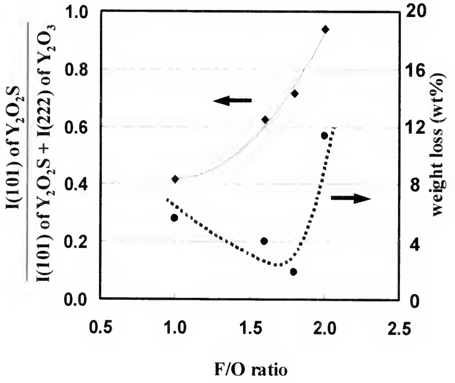

Figure 3-4. The effect of fuel (dithiooxamide) to oxidizer (F/O) ratio on the formation of Y_2O_2S and Y_2O_3 prepared by combustion reaction with $Y(NO_3)_3$, $Tb(NO_3)_3$ and dithiooxamide The weight loss was measured using thermogravimetric analysis (TGA). The peak location and identification of X-ray diffraction patterns agree with that of JCPDS #24-1424 for Y_2O_2S and #25-1200 for Y_2O_3.

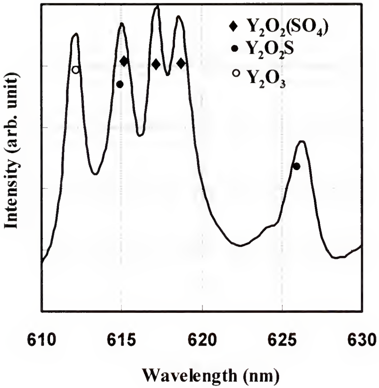

Figure 3-5. Cathodoluminescence (2 kV, 30 μA/cm^2) spectrum of powder after heat-treatment at 600 °C for 30 min in air. The as-synthesized powders, Y_2O_2S and Y_2O_3, were from the combustion reaction with $Y(NO_3)_3$, $Eu(NO_3)_3$ and dithiooxamide (F/O = 1.6) with an Eu content of 3.2 mole %.

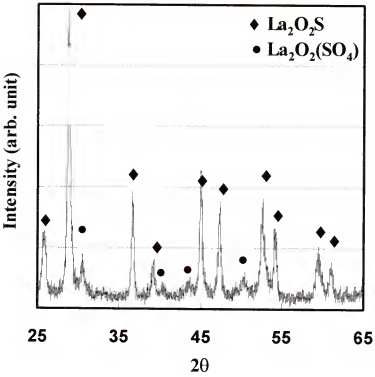

Figure 3-6. X-ray diffraction pattern of as-synthesized powder prepared by a combustion reaction of $La(NO_3)_3$, $Eu(NO_3)_3$ and dithiooxamide(F/O = 2.0) with water intentionally added. The peak location and identification agrees with that of JCPDS #27-263 for La_2O_2S and #16-1501 for $La_2O_2(SO_4)$.

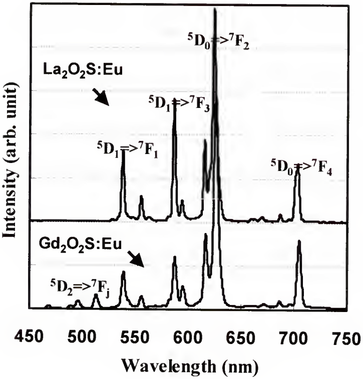

Figure 3-7. Cathodoluminescence spectra from La_2O_2S:Eu (0.5 mole %) and Gd_2O_2S:Eu (0.5 mole %) measured at 2 kV and 30 μA/cm^2.

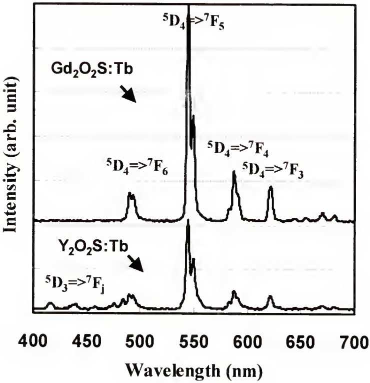

Figure 3-8. Cathodoluminescence spectra from Gd_2O_2S:Tb (0.2 mole %) and Y_2O_2S:Tb (0.2 mole %) measured at 2 kV and 20 μA/cm^2.

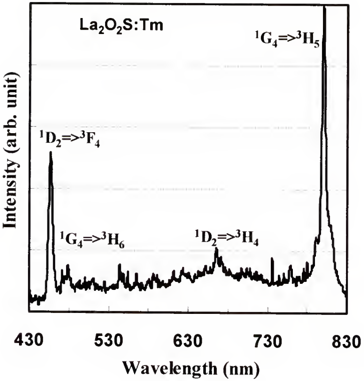

Figure 3-9. Cathodoluminescence spectrum from La_2O_2S:Tm (3.2 mole %) measured at 2 kV and 20 μA/cm^2.

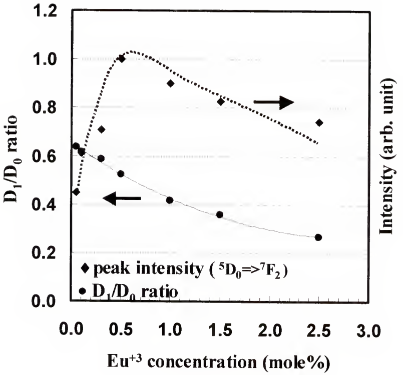

Figure 3-10. The CL emission intensity (2 kV, 30 μA/cm^2) from the $^5D_0$=> $^7F_2$ electronic transition of La_2O_2S:Eu phosphor and the peak intensity ratio D_1/D_0 (see text) observed from La_2O_2S:Eu phosphor as a function of Eu concentration.

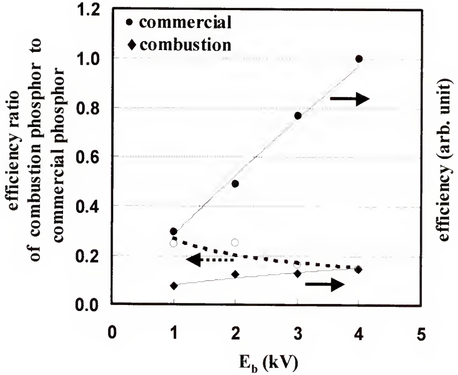

Figure 3-11. Relative efficiency and the ratio of the relative efficiencies of combustion prepared phosphors (1 mole %) to that of commercial phosphors for Gd_2O_2S:Tb as a function of electron beam energy (20 μA/cm^2).

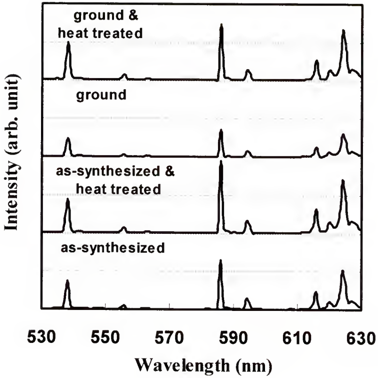

Figure 3-12. Photoluminescence spectra of "as-synthesized ", "as-synthesized and heat-treated", "ground" and "ground and heat-treated" La_2O_2S:Eu (1.0 mole %) powder phosphors (λ_{exc} = 325 nm). The heat treatment was at 900 °C for 60 min in Ar.

CHAPTER 4
TEMPORAL CATHODOLUMINESCENCE QUENCHING FROM Eu^{3+} DOPED La_2O_2S

4.1 Introduction

Temporal decay or rise times for CL peaks ranging from nsec. to msec. give information about the saturation mechanisms, such as ground state depletion and higher order energy transfer [IMA80, KUB80, STO00, TAL02]. Variations of luminescence over several hours or longer generally result from degradation. However, Seager reported variations of the CL luminescence over times in the range of sub-second to seconds due to applied external electric fields [SEA98].

The temporal CL quenching behavior of $La_2O_2S:Eu^{3+}$ powder phosphors prepared by combustion reaction are reported and discussed in this chapter. CL decays with the range of seconds were measured during DC electron beam bombardment. Intensities from $^5D_j \Rightarrow {}^7F_j$ electronic transitions are reported as a function of current density. It is suggested that the mechanisms affecting CL quenching are thermal quenching due to electron beam heating, and enhanced interactions (the first and second order effects discussed above) between activators from redistribution of charge carriers due to induced internal electric fields.

4.2 Experimental Section

$La_2O_2S:Eu^{3+}$ powder phosphors were prepared by combustion reaction with metal nitrate and dithiooxamide ($((CSNH_2)_2)$) fuel [BAN04]. The Eu^{3+} concentration ranged from 0.05 mole % to 3.2 mole %. CL measurements were made in two UHV systems (I and II). For CL measurements in system I, the powder samples were pressed into 3 mm deep, 13 mm wide holes in a stainless steel holder. An electron beam from a Kimball Physics electron gun (Model EGPS-7H) excited the samples with energies ranging from 1 to 5 kV and DC current densities ranging from 10 to 200 μA/cm^2. The emission spectrum and peak intensities were measured in reflection using an Ocean Optics S2000 fiber optic spectrometer with a CCD array detector. For system II, the powder samples were pressed into 4 mm deep, 6 mm wide holes in a stainless steel holder. The samples were excited by an electron beam from the electron gun in a PHI Model 545 scanning Auger electron spectrometer (AES) with energies ranging from 1 to 5 kV and DC current densities ranging from 50 to 800 μA/cm^2. The emission spectrum and peak intensities were measured in reflection using an Oriel 77400 Multi-spectrometer with a CCD array detector. Figure 4-1. shows the CL spectrum of $La_2O_2S:Eu^{3+}$ (0.5mole%) measured at 2 kV and 50 μA/cm^2. The peaks and their transition assignments are those normal for Eu^{3+} ion [ABD92]. For measurement of temporal behavior, CL data were acquired every 0.15 second. To measure CL as a function of temperature, the powder samples were pressed into 4 mm deep, 6 mm wide hole in a copper holder which housed a button heater [ABR01]. After heating to 350 °C as measured by a thermocouple attached to the holder, CL was measured as the sample was cooled back to room temperature. AES data were collected in system II with a PHI Model 545 scanning Auger Electron Spectrometer.

For PL measurements, powder samples pressed into 2 mm deep, 3 mm wide holes in a stainless steel holder were excited by 325 nm UV from a Omnichrome HeCd laser (Model 74, 30 mW). The emission spectra were measured in reflection using an

Instruments SA monochromator (Model HR-320, 0.3 m) and Hamamatsu GaAs photomultiplier tube (Model R943-02).

4.3 Results

4.3.1 Effect of Time, Temperature and Current Density on CL Intensities

The temporal dependence of CL intensity was measured versus current density for $La_2O_2S:Eu^{3+}$ powder phosphors excited by a 2 kV electron beam. As shown in Fig. 4-2(a), the normalized emission intensity corresponding to the $^5D_0 \Rightarrow ^7F_2$ (626 nm) transition of Eu^{3+} did not change at a low current density (65 μA/cm^2). However, it did decay over the first 5 seconds, approaching a normalized steady state intensity of 0.18, at a high current density (500 μA/cm^2). Fig.4-2(b) shows the variation of the initial and steady state intensities as a function of current density at 2 kV. The initial intensity increased linearly as the current density was increased, whereas the steady state intensity decreased at higher current densities. The emission intensity from the $^5D_0 \Rightarrow ^7F_2$ transition of Eu^{3+} was also measured as a function of temperature as shown in Fig. 4-3. As expected, a decrease of intensity from unity at room temperature to 0.3 at 350 °C was observed. This thermal quenching is explained by a crossover between the ^5D_j levels or ^5D_j and ^7F_j via the La_2O_2S charge transfer state (CTS), which leads to both decreased emission intensity and changes in the peak height ratios from ^5D_j (j = 0, 1, 2) transitions.

4.3.2 Effect of Current Density on $^5D_1/^5D_0$ Peak Height Ratios

The emission intensities from $^5D_1 \Rightarrow ^7F_3$ (591 nm) transitions of Eu^{3+} also changed with time of electron beam bombardment, decreasing faster than did $^5D_0 \Rightarrow ^7F_2$ transitions. Therefore, the peak height ratio designated $^5D_1/^5D_0$ and equal to the emission intensities from $^5D_1 \Rightarrow ^7F_3$ divided by $^5D_0 \Rightarrow ^7F_2$, changed with time. Fig. 4-4(a) shows that the $^5D_1/^5D_0$ ratio changed little with time at 65 μA/cm^2, but decreased from 0.53 to 0.27 at

500 μA/cm^2. Fig. 4-4(b) shows the variation of the initial and steady state $^5D_1/^5D_0$ ratios as a function of current density of a 2 kV beam. The initial $^5D_1/^5D_0$ ratio was independent of current density, but the steady state $^5D_1/^5D_0$ ratio decreased with increasing current density. Data in Fig. 4-4(a) and (b) show that quenching of the CL intensities results in an emission color change in addition to reduced luminescence efficiency.

4.3.3 Effect of Surface Potential on $^5D_1/^5D_0$ Peak Height Ratios

To evaluate why the CL intensities and peak height ratios were a function of current density, the carbon and oxygen AES peak energies were measured with an electron beam incident at three different locations: (A) upon the grounded metal sample holder, (B) near the phosphor/sample holder edge, or (C) well within the powder phosphor sample (see Fig. 4-5). There was no AES peak shifts at position A, (C: 272 eV, O: 510eV) whereas there was ~ 30 eV shifts to higher energies (C: 302 eV, O: 543eV) at position B, and ~ 60eV shifts (C: 330 eV, O: 567 eV) at position C. These shifts are most easily interpreted as negative charging of the phosphor surface which is dependent on the resistance to electron flow (leakage current) through the phosphor powder to electrical ground. The corresponding steady state $^5D_1/^5D_0$ ratio was 0.52 at position B and 0.56 at position C. Therefore the electrical charging measured by the shifts of the Auger peak energies (and which would retard the primary electron beam) does not explain changes in the CL peak intensities nor the peak height ratio.

4.3.4 Effect of Electon Beam Energy on $^5D_1/^5D_0$ Peak Height Ratios

The CL intensity decay over the first ~ 5 sec. of irradiation, which was larger at higher current densities (Fig. 4-2(a)) was also larger at higher electron beam energies. While the intensity of the $^5D_0 \Rightarrow {}^7F_2$ transition did not change with time at a low electron beam energy (1 kV), it decayed between time zero and ~ 5 sec. at high electron beam energies

(5 kV). The initial CL intensity was higher than that at steady state (t > 5sec), and this difference increased as the electron beam energy was increased from 1 to 5 kV. Fig. 4-6(a) shows the $^5D_1/^5D_0$ ratio at time zero and steady state versus electron beam energy at a moderate current density of 135 μA/cm^2. The initial $^5D_1/^5D_0$ ratio did not change, but the final $^5D_1/^5D_0$ ratio decreased with increasing electron beam energy. In contrast, the steady state $^5D_1/^5D_0$ ratio versus electron beam energy did not change at low current densities (30 μA/cm^2), as shown in Fig. 4-6(b).

4.3.5 Effect of Eu^{3+} Concentration on $^5D_1/^5D_0$ Peak Height Ratios

Data in Fig. 4-7(a) show that the behavior of the $^5D_1/^5D_0$ ratio versus current density has been classified into three regions (I, II, or III). In regions I and III there is no change of the $^5D_1/^5D_0$ ratio, whereas there is a change with current density in region II. As shown in Fig. 4-7(b), the current density at which the behavior of the $^5D_1/^5D_0$ ratio was classified as region I or II was dependent upon the Eu concentration. Fig. 4-8 shows the CL and PL $^5D_1/^5D_0$ peak height ratios as a function of Eu concentration. Note that the ratio from CL was lower than for PL. The difference between the ratios from CL and PL increased with decreasing Eu^{3+} concentration.

4.4 Discussion

4.4.1 CL Quenching at High Electron Beam Current Densities

4.4.1.1 Thermal quenching by electron beam heating

Electron beam heating at high current densities could potentially explain the quenching represented by decreased brightness. The initial intensity is measured so quickly that a temperature rise has not occurred. However, any temperature rise will have occurred and stabilized when the steady state intensity is recorded. Struck et al. reported that the emission intensity of $La_2O_2S:Eu^{3+}$ phosphor decreased with increasing temperature due to crossover between excited and ground states via the charge transfer state (CTS) [FON70, STR70, STR76]

Due to poor thermal contact between the phosphor particles, it is reasonable to assume that energy loss of the particles under electron beam bombardment occurs only by radiation. The temperature rise due to electron beam heating can be calculated by assuming heat is only lost by radiation from the visible transitions or as a black body, i.e. neglecting conduction in the packed powder bed and molecular transport in the vacuum. Stefan's equation is used for radiative transfer from a black body [ABR01, GES68]. The heat loss rate (Q_{T1}(W)) from a particle at T_1 can be expressed as

$$Q_{T1} = \sigma\ \varepsilon\ 4\pi r^2\ T_1^4$$

where σ = Stefan-Boltzmann constant (5.67×10^{-8} W/m^{2}K^4), ε = emissivity of the phosphor (unitless, 1 for black body radiation), r = radius of a particle (m), and T_1 = temperature of a particle before electron beam bombardment (K). Under electron beam excitation, the power (Q_e(W)) added to a particle from the electron beam and the heat loss rate (Q_{T2}(W)) from a particle at T_2 can be expressed as

$$Q_e = E_b\ I\ \pi r^2$$

where E_b = electron beam voltage (V), I = electron beam current density (A/m^2), and

$$Q_{T2} = \sigma\ \varepsilon\ 4\pi r^2\ T_2^4$$

where T_2 = temperature of a particle during electron beam bombardment (K).

Equating the power into and radiated out of a powder particle leads to

$$Q_e = (Q_{T2} - Q_{T1}) + L$$

where L = the CL radiant flux from a powder particle during electron bombardment (units of W).

Therefore, T_2 can be expressed as

$$T_2 = \{ (Q_e - L) / (\sigma\, \varepsilon\, 4\pi r^2) + T_1^4 \}^{1/4}.$$

T_2 corresponds to the upper limit of temperature from electron beam irradiation because a small amount of thermal conduction is expected from the packed powder bed. L is the power loss from the particle in the form of light emission, the value of which depends on current density (Fig. 4-2(b)). A quenching ratio, F, can be defined that is equal to the steady state emission intensity divided by the initial emission intensity from the $^5D_0 \Rightarrow {}^7F_2$ transition. This ratio, shown in Fig. 4-9, is equal to the relative luminescence efficiency because the initial emission intensity is proportional to electron beam current density (Fig. 4-2(b)). The quenching ratio F can be expressed as a function fitted to the data in Fig. 4-2(b), therefore L can be expressed as

$$L = (E_b\, I\, \pi r^2)\, L_1\, F$$

where L_1 = luminescence conversion factor when I approaches zero (reported value of 0.1 for $La_2O_2S:Eu^{3+}$ is used for the calculation [ALI77]) and F = quenching ratio at each current density.

Therefore, T_2 is simplified to

$$T_2 = \{ E_b I (1 - L_1 F) / (4\, \sigma\, \varepsilon) + T_1^4 \}^{1/4}$$

where T_1 = RT = 298 K (25 °C).

The reduction in emitted intensity due to thermal quenching from electron beam heating can be estimated using the value of T_2 at each electron beam current density and the temperature dependence of emitted intensity shown in Fig. 4-3. Then,

$$\mathrm{Int}_{(E)} = \mathrm{Int}_{(I)}\, R \quad \text{---- (1)}$$

where $Int_{(I)}$ = initial emission intensity from the $^5D_0 \Rightarrow {}^7F_2$ of Eu^{3+} at T_1 (25 °C), $Int_{(E)}$ = calculated emission intensity at T_2, and R = thermal quenching ratio at T_2 (i.e., Int_{T2}/Int_{RT}).

The value of R was calculated using the function fitted to data in Fig. 4-3 and applied to the data in Fig. 4-2(b). Figure 4-10 shows the intensity obtained from eq.(1), i.e., corrected for thermal quenching (middle curve), along with the initial (top curve) and steady state (bottom curve) emission intensity versus electron beam current density. It is assumed that the initial intensities are intrinsic to the phosphor being studied. On the other hand, the steady state intensities are influenced by a number of factors to be determined, including electron beam heating, charging and activator interactions. Note that the reduced intensity from thermal quenching due to electron beam heating does not completely explain the low steady state CL intensities. The difference between the value estimated from electron beam heating and the steady state values must result from additional quenching mechanisms.

4.4.1.2 Temporal CL quenching from induced internal electric fields

An incident electron beam loses its energy through inelastic interactions with the electrons of the solid phosphor, producing large numbers of electron and hole charge carriers in proportion to the incident electron beam energy and current density [SHI98]. The generated electrons and holes diffuse in the phosphor, and their diffusion lengths are governed by activator concentration and crystalline defects and strain. Charge carrier transport will also be strongly affected by electric fields [SEA98, YAN98a]. While some of generated electrons and holes recombine at defects acting as non-radiative recombination sites, others may recombine and transfer the recombination energy to the activator. The latter process is the main mechanism for activator excitation, and the efficiency of the transfer is a major factor that determines the CL phosphor efficiency. Excited activators experience non-radiative and radiative relaxations, and in addition may interact with neighbor activators. Higher electron beam current densities will produce higher densities of excited activator, and if activator interactions are possible and important, this may result in decreased CL intensity and a decreased peak height ratio $^5D_1/^5D_0$. However, the different behavior of initial and steady state values versus current densities shown in Fig. 4-2(b) and 4-4(b) suggests that a mechanism consisting only of increased activator interactions cannot explain the decay of emission intensity over the first 5 sec. This is true since the rate at which activators interact should be dependent upon the density of excited states. Without another mechanism to modify this density, it should reach a steady state value in times << 1 sec. Therefore a mechanism of pure activator interactions leading to quenching of CL efficiency would be applicable to both "initial" as well as "steady state" values. The present data show that initial state values are not quenched, but steady state values are quenched. This leads to the conclusion that higher densities of excited activator are induced in steady state with subsequent quenching of steady state values. Thus additional effects, e.g., internal electric fields, lead to a time dependence for the accumulation of excited activators to a density sufficiently high that luminescence is quenched in the steady state.

When the primary electron beam is incident on a phosphor, secondary, back-scattered and Auger electrons are emitted from the surface at a rate different from the primary beam current, and this rate is dependent upon the beam energy and phosphor properties. Therefore, positive or negative charges may accumulate on and below the surface to develop a space charge layer. If the integration of charge with depth is zero (i.e., the positive charge equals the negative charge) there is no net charge on the sample and no shift of the energy of the Auger electrons, even if an internal electric field exist beneath the surface over the range of the primary electrons. In the case of a metal, accumulated charge and the space charge layer are negligible because of the high electrical conductivity to ground. But in the case of an insulator like $La_2O_2S:Eu^{3+}$, the non-zero accumulated charge will produce a surface voltage (charging that affects the Auger electron energies). Charge separation (emission of true secondary electrons versus implantation of primary electrons) will also produce an internal electric field, as shown in Fig. 4-11 [CAZ91, MEL95, SEA97, VON85]. The shift to higher energies for the Auger electrons reported above suggests that for the present samples, the net charge relative to ground is negative. An internal electric field may form within an insulator in addition, independent of whether there is zero, positive or negative charging relative to ground. Furthermore, the internal electric field may increase with an increase of electron beam current density.

The fact that an internal electric field is induced during electron bombardment of phosphors and that diffusion of charge carriers is affected by electric fields suggest a possible mechanism for the CL quenching observed with time and increasing current density. As soon as the internal electric fields form, charge carriers start to redistribute under their influence until the generation and recombination rates reach a steady state condition. Because electrons have a much higher mobility as compared to holes, it is reasonable to assume that only electrons are affected by the induced internal electric field. Electrons generated inside the penetration range may move to and be localized at the (relatively) positively charged surface. The CL intensity decay over the first 5 sec., shown in Fig. 4-2(a), would correspond to the time required to establish a stable internal electric field and achieve a steady state charge carrier (electron) distribution. This localization of generated electrons near surface may increase the fraction of non-radiative surface recombination. Seager reported that there was a change in emission intensity with an applied external electric field due to electrons moving to the surface [SEA98]. The decreased intensity was consistent with the fact that non-radiative recombination at defects competed with radiative recombination, and that many defects exist at the surface. But if only internal electric fields were influencing quenching by non-radiative surface recombination, changes of the $^5D_1/^5D_0$ peak height ratio (Fig. 4-4(a) and (b)) would not be expected to accompany the overall reduced CL intensity (Fig. 4-2(a) and (b)). This also suggests that increased densities of excited activators due to induced internal electric fields affect the extent of quenching with increasing time and current density. During the first 5sec, the recombination rate of electrons and holes would be expected to increase due to the localization of generated electrons with a subsequent increased excited activator density. It is believed that the reduced emission intensity and decreased $^5D_1/^5D_0$ peak height ratio over the first 5 sec is a result of increased activator interactions. A change in the peak height ratio with applied voltage or frequency was reported in powder alternating current electroluminescnt (AC EL) Tb^{3+} doped Gd_2O_2S phosphor [SHA92]. Thus our postulate that an internal electric field can affect the $^5D_1/^5D_0$ peak height ratio of Eu^{3+} doped La_2O_2S phosphor is reasonable.

The data in Fig. 5 showing the lack of correlation between charge shifts of Auger peak energies and quenching of CL intensities and peak height ratios strongly suggest that surface charging (i.e., the internal electric field resulting from a net accumulation of charge and subsequent minor reduction of the incident electron beam energy) cannot explain these changes in CL. These data suggest that the relative strength of an internal electric field produced by net accumulated charge is not important to CL quenching until they become sufficiently large to change the primary beam energy and/or localized generated electrons. On the other hand, another internal electric field formed by penetrating electrons and positive charges from secondary electron emission can easily and dramatically change the CL intensities and efficiencies. It would seem reasonable to postulate that the total strengths of internal electric fields should be dependent on each strength of two kinds of internal electric field, but the present data are not sufficient to establish such a relationship. In fact, the absence of a correlation of quenching with the shift of Auger peak energies suggest that the strength of an internal field generated by net charge accumulation are only weakly correlated with the internal electric field generated by differential charge generation near the phosphor surface. However the data by Seager [SEA98] show that an applied external voltage (field) can influence the internal electric field.

4.4.2 Effect of Electron Beam Energy on Temporal CL Quenching

An increase of the peak height ratio $^5D_1/^5D_0$ with decreasing electron beam energy has been reported previously by Yang [YAN98a] and Jones et al. [JON99], and was attributed to a low concentration of the activator near the surface of the $Y_2O_3:Eu^{3+}$ phosphor. It has been reported that the $^5D_1$ transition is more sensitive to concentration quenching than is the $^5D_0$ transition [OZA71, SHI98]. Because the electron beam penetration depth decreases with decreasing electron beam energy, more of the luminance comes from the surface region at low voltages [SHI98]. The high $^5D_1/^5D_0$ ratio at low voltages is consistent with less concentration quenching of the $^5D_1$ transition if the surface is truly depleted in Eu^{3+}. However, Ozawa et al. [OZA90] used etching and inductively coupled plasma (ICP) analysis to determine that the concentration of Eu^{3+} was actually higher at the phosphor surface. Segregation of activators at the surface is therefore not consistent with the data shown in Fig. 4-6(a) and (b). In addition, attributing the change in the $^5D_1/^5D_0$ ratio to Eu^{3+} depletion at the surface is inconsistent with the lack of dependence of this ratio on electron beam energy at low current density (30 $\mu A/cm^2$) (see Fig. 4-6(b)). The penetration range of primary electrons only depends upon the beam energy, not the current density, therefore the ratio should vary with primary beam energy at any current density if the Eu concentration changes with depth.

Anticipating the conclusion that activator interactions increase at higher excited activator densities, it is interesting to consider how the charge carrier or excited activator density changes with beam energy and density. The density of charge carriers (electrons and holes) is directly proportional to the rate of charge carrier generation, and inversely proportional to the distribution range of charge carriers. The number of generated electron-hole pairs increases linearly with increased beam energy (E_b). The distribution range of charge carriers is generally governed by the electron penetration depth (R_p) which changes according to the relation "$R_p = K(E_b)^a$ where $K = 8.05$ and $a = 1.608$" [YAN98a]. Therefore, at lower beam energy, the density of charge carriers is higher. This argument is consistent with the conclusion of Seager et al. [SEA00a, SEA00b] that the density of electrons and holes increased with decreasing electron beam energy, and that this high density of excited activators resulted in a low CL efficiency at low electron beam energy.

While it is generally true that the density of excited activators will increase at lower beam energies, it is unreasonable to think that this density will always exhibit an increase. Based on the facts that more defects exist at the surface as compared to the bulk, and that charge carriers are generated near the surface at low voltages, it is assumed that more charge carriers will recombine non-radiatively at surface defects, and that a lower fraction of charge carriers recombine at activators at lower voltages. Based on this argument, the distribution of excited activators is not exclusively dependent on the relation between the penetration depth and electron beam energy. Under some conditions, the density of excited activators may also increase with increasing electron beam energy. Due to the negligible activator interactions at low current densities, surface defects that affect the excited activator density will not change the $^5D_1/^5D_0$ peak height ratios, consistent with the data in Fig. 4-6(b). However, at high current densities, stronger internal electric field will be induced and affect the diffusion of the generated charge carriers. Under these conditions, the surface defects will reduce the density of excited activator and increase the $^5D_1/^5D_0$ peak height ratios with decreasing electron beam energies, as shown in Fig. 4-6(a). Note that the density of excited activators may be sufficiently high to result in significant activator interactions at high current densities, even though surface defects decrease the density of excited activators.

4.4.3 Enhanced Activator Interaction by Induced Internal Electric Fields

As discussed above, the observed quenching behaviors are only partially explained by thermal quenching due to electron beam heating. It has been suggested above that this quenching is enhanced by a large density of excited activators from the redistribution of charge carriers under the induced internal electric field. Luminescence quenching may result from the activator interactions, in which excitation energy transfers from one activator to another and eventually to a defect acting as an energy sink (non-radiative site). This implies that luminescence quenching should increase with an increase of activator concentration or defect density. Two kinds of activator interactions are known to occur [BLA94, OZA71, SHI98, TAL02]. First, excited state activators (^5D_j level) may return to the ground state through the interaction with ground state activators (^7F_j level) which are raised to the excited state. During a series of activator interactions (i.e. energy transfer), quenching will occur if the energy transfer is to a non-radiative site. In addition, another possible result from this kind of cross relaxation is feeding to a lower excited state. For example, an activator in the $^5D_1$ level may return to the ground state resulting in a ground state activator being raised to the $^5D_0$ level, even though this feeding effect is usually screened by quenching of $^5D_0$ states on Eu^{3+} activators. An alternative mechanism is an interaction between excited activators. In this kind of cross relaxation, the activator interaction leads to an excited activator (^5D_j) transferring its energy to a neighboring excited activator (^5D_j) and returning to the ground state (^7F_j), while the neighboring excited activator is further excited into the charge transfer state (CTS) of Eu^{3+}. Decreased CL efficiency from such an up-conversion process has been discussed by Tallant et al. [TAL02]. They suggest that the excited Eu^{3+} in the CTS relaxes to an excited ^5D_j state, resulting in both reduced activator efficiency and reduced $^5D_1/^5D_0$ peak height ratio after up-conversion.

As shown in Fig. 4-7(a), the behavior of the $^5D_1/^5D_0$ ratio versus current density has been classified into three regions. In region I, the interaction between excited and ground state activators is considered to be dominant. This is confirmed by the fact that the $^5D_1/^5D_0$ ratio in region I changes with Eu^{3+} concentration as shown in Fig. 4-7(b) (compare data from 0.5 and 1.0 mole % Eu at constant current density). Further for region I, the constant $^5D_1/^5D_0$ ratio even with changes in current density implies that there is no significant change of interaction rate versus current densities, therefore the luminescence efficiency and the peak height ratio are constant. Note that the first order activator interaction rate is governed by the distance between activators (i.e., concentration), density of ground state activators, and density of excited state activators. With increasing Eu^{3+} concentrations, the distance between activators will decrease and the density of excited state activators will increase for the increased or constant transfer activator efficiency. At lower Eu^{3+} concentration, lower activator transfer efficiencies and larger charge carrier (electron and hole) diffusion lengths are expected with subsequent lower densities of excited activator. In addition, the density of excited and ground state activators will depend on current densities. Therefore, it is reasonable that at lower Eu^{3+} concentrations, the transition between region I and region II behavior occurs at higher current densities, as shown in Fig. 4-7(b). For region II, the $^5D_1/^5D_0$ peak height ratio will change because the rate of interactions between excited and ground state activator is increasing with increases in electron beam current density, resulting in a reduced peak height ratio $^5D_1/^5D_0$. In region III, interactions between excited state activators become dominant because the distance between excited state activators is sufficiently short, i.e., the density of excited state activators is large. The up-conversion processes discussed above dominate and result in a lower efficiency and constant $^5D_1/^5D_0$ ratio. After up-conversion, the excited Eu^{3+} in the CTS relaxes to an excited ^5D_j state, apparently returning this population to the same as before up-conversion, resulting in reduced activator efficiency and a constant $^5D_1/^5D_0$ peak height ratio with increasing current densities. Table 4-1 summarizes the characteristics of region I, II and III and the dominant relaxation mechanisms.

To better understand the effects of electric fields and excited activator densities upon CL, consider the effects of PL versus CL on the $^5D_1/^5D_0$ ratio, as shown in Fig. 4-8. The excitation wavelength for PL was 325 nm and corresponds to the CTS energy level of Eu^{3+} doped La_2O_2S, since the CTS absorption maximum is reported to be at 335 nm [RED96]. In PL, the $^5D_1/^5D_0$ ratio can be changed by changing the excitation wavelength e.g., direct, host band or CTS excitation. For CL, the main excitation route is known to be via the CTS [OZA81], therefore the different $^5D_1/^5D_0$ ratio for PL and CL (Fig. 4-8) is not due to different distributions of the excited ^5D_j states. Higher PL or CL excitation intensities also produce lower $^5D_1/^5D_0$ ratios, presumably due to quenching by activator interactions. However, the parameters used for CL data in Fig. 4-8 (2 kV, 30 $\mu A/cm^2$) correspond to region I, as defined in Fig. 4-7(a) and (b). At first thought, the $^5D_1/^5D_0$ ratio should have been constant under these conditions. As discussed above, the first order activator interaction rate is governed by the distance between activators (i.e., concentration), density of ground state activators, and density of excited state activators. But, the exact dependence upon these parameters is unknown. From the data, the peak ratio (e.g., interaction rate) depends on activator concentration but not on current densities in the region I. Apparently the effects of increased Eu concentrations on activator interactions is larger than that of increased current density in the region I. The origin of this effect requires further study.

Excited activators lose their energy via three routes: (i) luminescent decay, (ii) energy transfer (interaction) to a neighboring activator (in an excited or ground state), and (iii) non-radiative decay. In the case of luminescent decay, the Eu^{3+} emission peaks at 626 nm and 591 nm correspond to $^5D_0 \Rightarrow {}^7F_2$ and $^5D_1 \Rightarrow {}^7F_3$ transitions, respectively, and both occur by electric dipole transitions (forced electrostatic dipole transitions) [SHI98]. However, in the case of energy transfer, the interaction mechanisms is dependent upon the excited state ($^5D_0$ and $^5D_1$). These mechanisms are magnetic dipole-dipole for $^5D_0$ and electrostatic dipole-dipole for $^5D_1$ [OZA71, OZA90]. These differences suggest another possible reason for quenching of the $^5D_1/^5D_0$ ratio. Under an external or internal electric field, the electrostatic interactions may increase, whereas the magnetic dipole-dipole interaction may be unchanged. Increased energy transfer will result in less emission, consistent with emissions from $^5D_1$ decreasing and resulting in lower $^5D_1/^5D_0$ peak height ratios. Since an internal electric field should be induced only by CL excitation, the data in Fig. 4-8 are consistent with the $^5D_1/^5D_0$ ratios being reduced by the effects of internal electric fields on energy transfer between ground and excited state activators.

4.5 Conclusion

The effects of Eu concentration, primary beam energy and current density upon the cathodoluminescent (CL) intensity and color from $La_2O_2S:Eu^{3+}$ prepared by a combustion reaction has been studied. It was shown that the emission intensity and peak height ratio from the $^5D_1 \Rightarrow {}^7F_3$ and $^5D_0 \Rightarrow {}^7F_2$ (i.e., the $^5D_1/^5D_0$ ratio) decayed over the first several seconds of electron beam irradiation. The extent of the intensity decay and ratio change increased with increased electron beam current density and energy. A significant fraction of the CL quenching was shown to result from thermal quenching due to electron beam heating. However, this could not completely explain the amount of quenching nor the color change. To explain these changes, it was postulated that local redistribution of charge carriers over the range of the primary electron beam resulted from induced internal electron field and modified the interactions of activators. Specifically, first and second order activator interactions (between ground and excited state activators, and between excited state activators) modified by the induced electric fields, were postulated to be significant and controlling at higher excitation densities (e.g., at high primary beam energy and high current densities). Further, the internal electric field was speculated to change the interactions of the excited ^5D_j state of Eu^{3+} and thereby affect the $^5D_1/^5D_0$ ratio. These mechanisms were used to explain the difference between PL and CL results. The dependence of CL quenching upon current density, beam energy and Eu^{3+} activator concentration was classified into three regions dependent upon whether first or second order activation interactions were dominant in the luminescent relaxation process.

Table 4-1. Characteristics of region I, II, and III

	[a]peak height ratio	[a] luminescence efficiency	interaction type	[a] interaction rate change
Region I	*constant, high*	*constant*	[b] $G \Leftrightarrow E$	*negligible*
Region II	*decrease*	*decrease*	$G \Leftrightarrow E$	*yes*
Region III	*constant, low*	*decrease*	$E \Leftrightarrow E$	*yes*

a. Variations with increasing electron beam current density,
b. G : ground state activator E : excited state activator

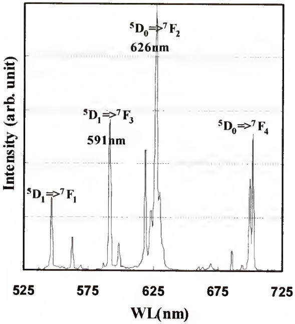

Figure 4-1. Cathodoluminescence spectrum of La_2O_2S:Eu^{3+} (0.5 mole %) measured at 2 kV and 50 μA/cm^2.

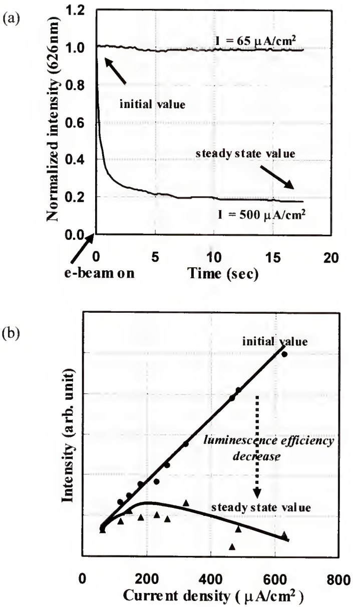

Figure 4-2. Emission intensity versus time or current density. (a) The temporal behavior of emission from the $^5D_0 \Rightarrow {}^7F_2$ transition of $La_2O_2S:Eu^{3+}$ (0.5 mole %) excited by a 2 kV electron beam. (b) The initial and steady state emission intensity from the $^5D_0 \Rightarrow {}^7F_2$ transition of $La_2O_2S:Eu^{3+}$ (0.5 mole %) as a function of electron beam current density with a 2 kV electron beam.

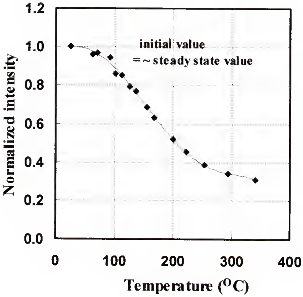

Figure 4-3. Temperature dependence of the $^5D_0$=>$^7F_2$ transition from $La_2O_2S:Eu^{3+}$ (0.5 mole %). (2 kV, 75 μA/cm^2)

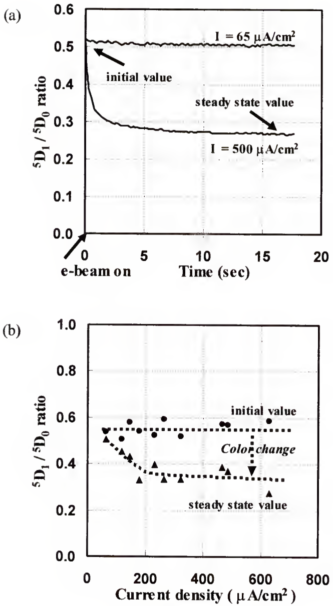

Figure 4-4. Peak height ratio versus time and current density. (a) The temporal behavior of peak height ratio $^5D_1/^5D_0$ observed from $La_2O_2S:Eu^{3+}$ (0.5 mole %) phosphor with a 2kV electron beam. (b) The initial (t = 0) and steady state peak height ratio $^5D_1/^5D_0$ observed from $La_2O_2S:Eu^{3+}$ (0.5 mole %) as a function of electron beam current density at 2 kV.

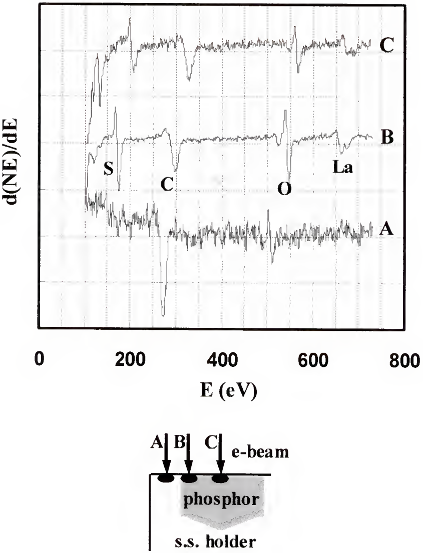

Figure 4-5. Auger electron spectra of $La_2O_2S:Eu^{3+}$ (0.5 mole %) phosphor measured at position A, B and C. (2 kV, 60 μA/cm^2) The correspondent steady state peak height ratio $^5D_1/^5D_0$ is 0.52 at B and 0.56 at C.

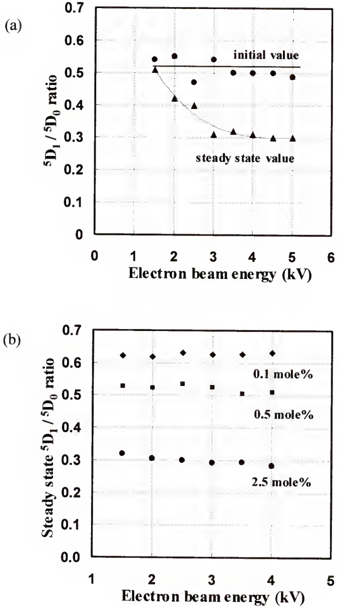

Figure 4-6. Peak height ratio versus electron beam energy. (a) The initial (t = 0) and steady state $^5D_1/^5D_0$ peak height ratio observed from $La_2O_2S:Eu^{3+}$ (0.5 mole %) as a function of electron beam voltage at 135 $\mu A/cm^2$. (b) The steady state $^5D_1/^5D_0$ peak height ratio observed from $La_2O_2S:Eu^{3+}$ phosphor as a function of electron beam energy at 30 $\mu A/cm^2$.

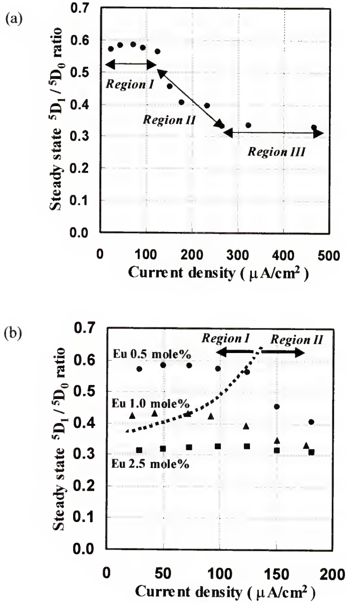

Figure 4-7. steady state peak height ratio versus current density. (a) The steady state $^5D_1/^5D_0$ peak height ratio observed from $La_2O_2S:Eu^{3+}$ (0.5 mole %) phosphor as a function of electron beam current density. The electron beam voltage was 2 kV. (b) The steady state $^5D_1/^5D_0$ peak height ratio versus electron beam current density. The electron beam voltage was 2 kV and Eu concentrations were 0.5, 1.0 or 2.5 mole %.

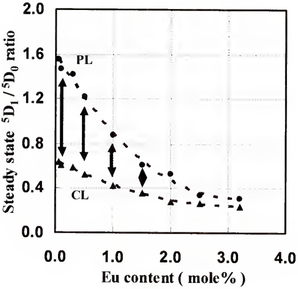

Figure 4-8. The steady state peak height ratio $^5D_1/^5D_0$ observed in $La_2O_2S:Eu^{3+}$ phosphor as a function of Eu concentration (CL condition: 2 kV, 30 μA/cm^2 , PL condition: λ_{ex} = 325nm from He-Cd laser).

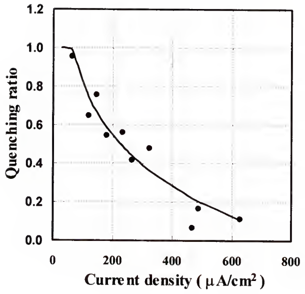

Figure 4-9. The quenching ratio, F, observed from $La_2O_2S:Eu^{3+}$ (0.5 mole %) as a function of electron beam current density at 2 kV. These ratios were calculated from data in Fig. 4-2(b).

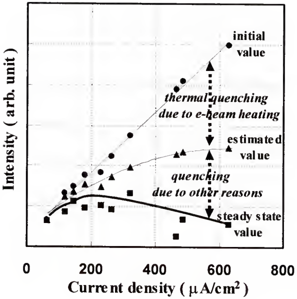

Figure 4-10. The estimated intensity corrected for thermal quenching from the $^5D_0 \Rightarrow {}^7F_2$ transition from $La_2O_2S:Eu^{3+}$ (0.5 mole %) as a function of electron beam current density at 2 kV.

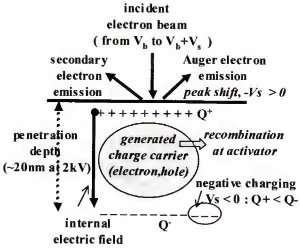

Figure 4-11. Schematic of charge distribution and internal electric field in Eu^{3+} doped La_2O_2S phosphor during electron beam bombardment.

CHAPTER 5

EFFECTS OF ENERGY FEEDING AND FUNNELING ON PEAK HEIGHT RATIOS $^5D_J/^5D_0$ FROM CATHODOLUMENSCENC OF $Ln_2O_2S:Eu^{3+}$ (Ln = La, Gd)

5.1 Introduction

With respect to cathodoluminescence, reducing the operating voltage from 15 ~ 30 kV to 2 kV causes the phosphor efficiency to drop by more than a factor of ten. Since it is desirable for field emission displays (FEDs) to operate at such low voltages, the current density must be increased to achieve brightness comparable to cathode ray tubes (CRTs). At high current densities, FED phosphors suffer from quenching of the cathodoluminescent (CL) efficiency. Bang et al. [BAN03] reported temporal CL quenching of $La_2O_2S:Eu^{3+}$ (0.5 mole %) powder phosphors with increasing current density. While the CL intensity was constant at low current densities, the intensity decreased from a high initial intensity to a lower steady state value over times ~5-15 sec at high current densities (500 μA/cm²). During temporal CL quenching, the intensity of the $^5D_1 \Rightarrow ^7F_3$ (591 nm) Eu^{3+} transition also decreased faster with time than did the $^5D_0 \Rightarrow ^7F_2$ transition (626 nm). The change in the peak height ratio of $^5D_1/^5D_0$ (i.e., the emission intensity from the $^5D_1 \Rightarrow ^7F_3$ divided by $^5D_0 \Rightarrow ^7F_2$ transitions) resulted in a change in the emission color. The time (t_{ini}) to reach the initial maximum CL intensity (I_{ini}) is in the range of nanoseconds to milliseconds. The initial maximum CL intensity and subsequent time dependence is a function of activator concentration, density of non-radiative center, excitation density and temperature. In contrast to the rise to I_{ini}, the time (t_{quench}) to quench the initial intensity (I_{ini}) to the steady state intensity (I_{ss}) is several seconds due to a variety of reasons. Bang et al. [BAN03] suggested that temporal CL quenching of $La_2O_2S:Eu^{3+}$ resulted from the localized redistribution of charge carriers by the induced internal electron field and the subsequent increased activator interactions.

In this paper, the effects of electron beam current density on the CL emission intensities from each Eu^{3+} excited state, ^5D_j, of $Ln_2O_2S:Eu^{3+}$ (Ln = La, Gd) were studied. Uitert et al. [UIT66] reported that multi-polar resonant interactions equally quenched all of the emission transitions (e.g. $^5D_1 \Rightarrow {}^7F_1$, $^5D_1 \Rightarrow {}^7F_3$ etc.) originating from a given manifold (e.g. $^5D_1$). Also, both emission intensities from $^5D_1 \Rightarrow {}^7F_3$ and $^5D_1 \Rightarrow {}^7F_1$ (540 nm) of Eu^{3+} transition decreased at the same rate during temporal CL quenching. Therefore, the effects in this study are based on the relative emission intensities of the $^5D_2 \Rightarrow {}^7F_3$ (516 nm) and $^5D_1 \Rightarrow {}^7F_3$ to $^5D_0 \Rightarrow {}^7F_2$ transition, which are denoted in this paper by $^5D_2/^5D_0$ and $^5D_1/^5D_0$. In particular, the feeding from a higher ^5D_j to a lower $^5D_0$ excited state was reported as the peak height ratios, $^5D_j/^5D_0$, versus electron beam current densities and thermal quenching.

5.2 Experimental Section

Eu^{3+} doped La_2O_2S and Gd_2O_2S (Eu^{3+} = 0.1 ~ 2.5 mole %) powder phosphors prepared by combustion reaction [BAN04] or commercial $Gd_2O_2S:Eu^{3+}$ (0.4 mole %) powder phosphors were used for experiments. The phosphors behaved similarly therefore are not distinguished below. CL data were collected using two ultra-high vacuum (UHV) systems (I and II). For CL measurements in system I, the powder samples were pressed into 3 mm deep, 13 mm wide holes in a stainless steel holder. An electron beam from a Kimball Physics electron gun (Model EGPS-7H) excited the samples with 2 keV energy and DC current densities ranging from 10 to 200 μA/cm^2. The emission spectrum and peak intensities were measured in reflection using an Ocean Optics S2000 fiber optic spectrometer with a CCD array detector. For system II, the powder samples were pressed into 4 mm deep, 6 mm wide holes in a stainless steel holder. The samples were excited by an electron beam from the electron gun in a PHI Model 545 scanning Auger electron spectrometer (AES) with 2 keV energy and DC current densities ranging from 10 to 1000 $\mu A/cm^2$. The emission spectrum and peak intensities were measured in reflection using an Oriel 77400 Multi-spectrometer with a CCD array detector. The CL spectra of $La_2O_2S:Eu^{3+}$ (0.5 mole %) and $Gd_2O_2S:Eu^{3+}$ (0.5 mole %) measured at 2 kV and 30 $\mu A/cm^2$ are shown in Fig.5-1. The peaks and their transition assignments are those normal for Eu^{3+} [ABD92, STR70]. Note that emissions from $^5D_2$ state were not observed in $La_2O_2S:Eu^{3+}$ due to thermal quenching at RT. To characterize the temporal behavior, CL data were acquired every 0.15 second. To measure CL as a function of temperature, the powder samples were pressed into 4 mm deep, 6 mm wide hole in a copper holder which housed a button heater [ABR01]. After heating to 350 ^oC as measured by a thermocouple attached to the holder, the CL was measured as the sample was cooled back to room temperature.

5.3 Results and Discussion

5.3.1 Temporal CL Quenching at Lower Eu^{3+} Concentration

The temporal dependence of CL intensity was measured versus current density for $La_2O_2S:Eu^{3+}$ (0.1 mole %) powder phosphors excited by a 2 kV electron beam. The intensities of the $^5D_0 \Rightarrow ^7F_2$ (626 nm) or $^5D_1 \Rightarrow ^7F_3$ (591 nm) transitions did not change with time at a low current density (28 $\mu A/cm^2$). However, they did decay over the first 5 seconds and approach a lower steady state intensity at high current densities. The temporal quenching ratios (I_{ss}/I_{ini}) versus current densities were calculated for the $^5D_0$=>$^7F_2$ or $^5D_1$=>$^7F_3$ transitions of Eu^{3+}. As shown in Fig. 5-2, each temporal quenching ratio decreased with an increase of current density. Note that the temporal quenching ratios from the $^5D_1$=>$^7F_3$ transition of Eu^{3+} decreased faster than did $^5D_0$=>$^7F_2$ transition with an increase of current density (0.40 for $^5D_0$=>$^7F_2$ and 0.18 for $^5D_1$=>$^7F_3$ at 820 μA/cm^2). These results were consistent with previous results [BAN03], which were reported for 0.5 mole % Eu^{3+} doped La_2O_2S.

Since the temporal quenching ratios are a function of the specific transition and current density, the ratio of intensities (e.g., $^5D_1/^5D_0$ which is equal to the emission intensities from $^5D_1$=>$^7F_3$ divided by $^5D_0$=>$^7F_2$) are also a function of time and current density. For example, the initial and steady state peak height ratios, $^5D_1/^5D_0$, both increased at low current densities (0.66 and constant at 28 μA/cm^2, 0.75 for initial and 0.72 for steady state at 110 μA/cm^2), and both decreased at high current densities (0.72 for initial and 0.33 for steady state at 820 μA/cm^2), as shown in Fig. 5-3. The increase of peak height ratio, $^5D_1/^5D_0$, at lower current densities resulted from the fact that the emission intensity from the $^5D_0$=>$^7F_2$ transition decreased faster with increased current density than the intensity of the $^5D_1$=>$^7F_3$ transition.

An increased peak height ratio, $^5D_1/^5D_0$, with increased current density was also observed from Eu^{3+} doped Gd_2O_2S powder phosphors. Figure 5-4 shows the initial and steady state $^5D_1/^5D_0$ ratios from commercial $Gd_2O_2S:Eu^{3+}$ (0.4 mole %) phosphors as a function of current density, as well as similar data, $^5D_2/^5D_0$, for transitions originating from the $^5D_2$ and $^5D_0$ states. Due to the weak emission intensity of the $^5D_2$=>$^7F_4$ (543 nm) transition and its overlap with the emission from the $^5D_1$=>$^7F_1$ (540 nm) transition, the values of $^5D_2/^5D_0$ are from the $^5D_2 \Rightarrow ^7F_3$ (516 nm) and the $^5D_0 \Rightarrow ^7F_2$ (626 nm) transitions. The increases of $^5D_1/^5D_0$ ratios versus current densities (0.26 at 14 μA/cm^2 to 0.38 at 386 μA/cm^2) are similar to those observed in $La_2O_2S:Eu^{3+}$ (0.1 mole %). While the initial $^5D_2/^5D_0$ ratio increased only slightly (0.08 ~ 0.11) for current densities in the range of 14 ~ 770 μA/cm^2, the steady state ratio decreased from 0.08 at 14 μA/cm^2 to 0.02 at 770 μA/cm^2.

The increase of $^5D_1/^5D_0$ and $^5D_2/^5D_0$ initial peak height ratios with current density is in contrast to the general rule of increased activator interactions at higher excitation densities, i.e. higher current densities as reported by Bang, et al. [BAN03]. For example, Bang, et al. [BAN03] reported that for La_2O_2S phosphors with higher Eu^{3+} concentration (e.g., 0.5 ~ 2.5 mole %), the emission intensities from $^5D_1 \Rightarrow ^7F_3$ decreased faster than from $^5D_0 \Rightarrow ^7F_2$ with an increase of current density. Ozawa et al. [OZA71] reported that the activator efficiency (defined to be the emission intensity from $^5D_j \Rightarrow ^7F_j$ divided by activator concentration) of Eu^{3+} doped Y_2O_3 phosphors excited by 365 nm radiation decreased faster with increased Eu concentration as the excited state changed from $^5D_0$ to $^5D_1$ to $^5D_2$.

5.3.1.1 Feeding from a higher to lower excited states

For the 1st order activator interaction as shown in Fig. 5-5, the Eu^{3+} activator with $^5D_2$ energy state (donor, middle left) goes to a lower energy state either a $^5D_1$, $^5D_0$ or ^7F_j and the energy is transferred to the neighboring Eu^{3+} activator (acceptor, middle right) that is in ^7F_j ground state and converts it to a higher energy excited state such as ^5D_j or $^7F_j^*$. This energy transfer to the neighboring Eu^{3+} activator occurs by various interaction mechanisms such as a magnetic dipole-dipole, electric dipole-dipole, electric dipole-quadrupole, and electric quadrupole-quadrupole interactions discussed above.

Due to the dependence of multi-polar interactions on the strength of the transition and the distance between activators, emissions from higher excited experience significant quenching at a lower activator concentration. This results in a decrease of the peak height ratio $^5D_2/^5D_0$ with an increase of Eu^{3+} activator concentration. Activator interactions also result in energy feeding of lower (e.g., $^5D_1$) by higher excited state (e.g., $^5D_2$), with the subsequent increase of the peak height ratio $^5D_1/^5D$ at selected concentration. Due to energy feeding increasing the concentration of lower excited states, the concentration dependence for multi-polar resonant interactions may be complex [BLA94, OZA71], but this energy feeding by activator interactions has been confirmed from emission time-resolved decay for each ^5D_j state [STR70, TAL02].

In the above discussion, luminescence quenching and feeding by activator interactions have been considered in terms of activator concentration. However, luminescence quenching from an increased excitation density (i.e., increased electron beam current density) has been explained by activator interactions [BAN03]. The feeding phenomena are supposed to occur with an increase of current density.

5.3.1.2 Competing process: feeding vs. funneling

The density of excited state ^5D_j (e.g., $^5D_1$) is increased by the rate of feeding from a higher excited state (e.g., $^5D_2$) and decreased by the rate of funneling (quenching) to a lower excited state (e.g., $^5D_0$) or ground state (e.g., ^7F_j). The feeding rate is dominant over the funneling rate at low Eu^{3+} concentrations or low current densities, while the funneling rate dominates at high Eu^{3+} concentrations or current densities. Dominance of the feeding process causes the increase in the initial and steady state intensity ratio of $^5D_1/^5D_0$ in Fig.

5-3. In contrast, at higher current densities where funneling processes dominated, the initial and steady state intensity ratios of $^5D_1/^5D_0$ decreased (Fig. 5-3). Note that the difference between the initial and steady state intensity values is zero at low current densities (28 μA/cm^2), but is larger at high current densities (820 μA/cm^2). This results from higher induced internal electric fields at higher current densities and the subsequent increased activator interactions [BAN03].

At selected combinations of Eu^{3+} concentration (e.g., 0.4 % in Fig. 5-4) and current density (e.g., >200 μA/cm^2 in Fig. 5-4 for $Gd_2O_2S:Eu^{3+}$ phosphors), significant activator interactions with funneling to the $^5D_1$ state led to a decrease in the steady state $^5D_2/^5D_0$ ratio, while the steady state $^5D_1/^5D_0$ ratio continued to increase due to feeding from the $^5D_2$. The fact that the initial $^5D_2/^5D_0$ ratio is only slightly changed implies that the feeding from the higher excited state, $^5D_3$, to the lower excited state, $^5D_2$, is compensated by the funneling from the higher excited state, $^5D_2$, to the lower excited state, $^5D_1$, in the current densities ranging from 10 ~ 800 μA/cm^2. In addition, the decrease of the steady state $^5D_2/^5D_0$ ratio suggests that the activator interactions of the $^5D_2$ state is very sensitive to the density of excited activators, as compared to that of $^5D_1$ or $^5D_0$ state activators. It is speculated that the density of excited activator at the steady state is higher than that in the initial state due to induced internal electric fields. In contrast to $Gd_2O_2S:Eu^{3+}$, a decrease of the $^5D_2/^5D_0$ ratio resulting in the increase of the $^5D_1/^5D_0$ ratio can not be observed from $La_2O_2S:Eu^{3+}$ because emissions from $^5D_2$ state are completely thermal quenched at room temperature. It is supposed that that the energy of the $^5D_2$ state, which is going to be thermally quenched by non-radiative decay, is transferred to $^5D_1$ state by activator interactions.

To demonstrate that feeding and funneling phenomena can be created and controlled at higher excited activator densities, the steady state $^5D_1/^5D_0$ ratio is shown as a function of Eu^{3+} concentration in La_2O_2S for a given current density (between 22 to 176 $\mu A/cm^2$) in Fig. 5-6. While the peak $^5D_1/^5D_0$ height ratios from La_2O_2S with low Eu^{3+} concentration (e.g., 0.3 mole %) increased from 0.59 to 0.65 when the current density was increased, those from La_2O_2S with higher Eu^{3+} concentrations (e.g., from 1.0 mole %) decreased from 0.43 to 0.33. This result suggests that the feeding and funneling phenomena are simultaneous functions of both current density and Eu^{3+} concentration.

5.3.2 Thermal versus Activator Interaction Quenching

While the quenching discussed above are concluded to result from activator interactions at high excited state densities resulting from the appropriate combinations of Eu concentration and current densities, it was also pointed out that thermal quenching is important to the processes, e.g., the absence of $^5D_2$ emissions from $La_2O_2S:Eu^{3+}$. To further explore the role of thermal quenching, the steady state $^5D_2/^5D_0$ and $^5D_1/^5D_0$ ratios from commercial $Gd_2O_2S:Eu^{3+}$ (0.4 mole %) phosphors are shown in Fig. 5-7 versus temperature. At 2 kV and 15 $\mu A/cm^2$, temporal CL quenching of emission from ^5D_j (j = 0, 1, 2) was not observed at room temperature. With increasing temperature, the $^5D_2/^5D_0$ ratios decreased (from 0.09 at 30 °C to 0.01 at 130 °C) while the $^5D_1/^5D_0$ ratio was constant to within experimental error (0.26 ~ 0.28 at 30 ~ 130 °C). To investigate the effects of excited state densities, the steady state $^5D_2/^5D_0$ and $^5D_1/^5D_0$ ratios versus current densities at each Eu^{3+} concentration are shown in Fig. 5-8. While the $^5D_2/^5D_0$ ratio at 18 $\mu A/cm^2$ decreased with increasing Eu^{3+} concentration (0.08, 0.04 and 0.02 for 0.5, 1.0 and 2.5 mole %, respectively), the ratio converged to ~ 0.01 at high current densities (e.g., 193 μA/cm^2), independent of Eu^{3+} concentration. In contrast, the $^5D_1/^5D_0$ ratios increased with all current densities and did not show convergence at high current densities.

To interpret the data in Figs. 5-7 and 5-8, consider that a higher excited state may be more quickly converted to a lower excited or ground state (^7F_j) through a charge transfer level (assuming crossover by excited f levels (^5D_j) or ground f levels (^7F_j)) and multi-phonon relaxation with an increase of temperature [FON70, SHI98]. Even though the effects of temperature and activator interactions upon emissions from ^5D_j states are from different mechanisms, the effects of a temperature change are similar to those from activator interactions. Emissions from the ^5D_j states of Eu^{3+} doped phosphors generally decrease when temperature is increased (thermal quenching), similar to the decreased emission from ^5D_j states when the excited state density is too high [BOS02, FON70, ROB76].

However, the quantitative effects of temperature and current density on the $^5D_1/^5D_0$ peak height ratios were different. As shown in Fig. 5-7 and 5-8 for Gd_2O_2S:Eu^{3+}, temperature had little effect, while increased current density resulted in an increased steady state $^5D_1/^5D_0$ ratio, in contrast to a decrease of the steady state $^5D_2/^5D_0$ ratios. The different behavior of the $^5D_2/^5D_0$ versus $^5D_1/^5D_0$ peak height ratios results from the different mechanisms for thermal and interaction quenching.

With respect to temporal quenching in La_2O_2S:Eu^{3+} (0.5 mole %) phosphors, Fig. 5-9 shows the initial and steady state $^5D_1/^5D_0$ ratios versus temperature. Both the initial and steady state $^5D_1/^5D_0$ ratios decreased with temperature and finally approached a ratio of ~0.1 at 350 °C. In contrast, the $^5D_1/^5D_0$ ratio versus current density converged to a larger value of ~ 0.3, as shown previously [BAN03] and in Fig. 5-3. The different convergent values result from the different quenching mechanisms for temperature versus activator interactions. This observation of different effects for thermal versus excited state densities suggests that the temporal CL quenching of emissions from ^5D_j of $Ln_2O_2S:Eu^{3+}$ (Ln = La, Gd) at higher current densities do not result from electron beam heating, but result instead from activator interactions

5.4 Conclusion

The effects of excited state densities and temperature on the temporal quenching of the $^5D_2$=>$^7F_3$, $^5D_1$=>$^7F_3$ and $^5D_0$=>$^7F_2$ cathodoluminescent transitions from $Ln_2O_2S:Eu^{3+}$ (Ln = La, Gd) have been studied. The decrease of the emission intensities with time, i.e. temporal quenching, was characterized by the initial (t = 0) and the steady state (t = ~5-15 sec) intensity ratios of these transitions, designated as $^5D_2/^5D_0$ and $^5D_1/^5D_0$. For $Gd_2O_2S:Eu^{3+}$ (0.4 mole %), the steady state $^5D_1/^5D_0$ ratios increased (from 0.26 to 0.38) at lower current densities (from 14 to 386 μA/cm^2) and decreased (from 0.38 to 0.34) at higher current densities (from 386 to 772 μA/cm^2). These data were explained by postulating that the $^5D_1$ state was fed by non-radiative relaxation of the $^5D_2$ excited state at low current densities, resulting in an increased $^5D_1/^5D_0$ ratio. However, at high current densities, energy was funneled from the $^5D_1$ to the $^5D_0$ or ground state (e.g., ^7F_j), resulting in a lower $^5D_1/^5D_0$ ratio. Consistent with this interpretation, the steady state $^5D_2/^5D_0$ ratios decreased (from 0.08 to 0.03) as the current densities were increased from 14 to 386 μA/cm^2. This suggests that the feeding from the higher $^5D_2$ to the lower excited state $^5D_1$ also result in the decrease of $^5D_2/^5D_0$, along with the increase of $^5D_1/^5D_0$. The dependence of feeding upon current density was also dependent on the Eu^{3+} concentration, and the rate decreased at steady state due to increased activator interactions induced by internal electric fields. In addition, the feeding and funneling phenomena was shown to be simultaneous functions of both current density and Eu^{3+} concentration The effects of temperature versus activator interactions upon CL quenching was studied and it was shown that the $^5D_1/^5D_0$ was constant (versus temperature) or increased (versus current density), while the $^5D_2/^5D_0$ ratio from $Gd_2O_2S:Eu^{3+}$ phosphors decreased as either the temperature or current density was increased. The different behavior of the $^5D_1/^5D_0$ versus $^5D_2/^5D_0$ peak height ratios results from the different mechanisms for thermal and interaction quenching. The $^5D_1/^5D_0$ ratio from $La_2O_2S:Eu^{3+}$ (0.5 mole %) phosphors versus temperature and current densities were also reported and different limiting values (~ 0.1 at high temperatures and ~ 0.3 at high current densities) suggest that temporal CL quenching does not result from heating by the electron beam.

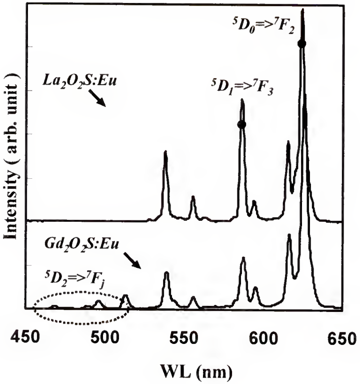

Figure 5-1. Cathodoluminescent spectra from $La_2O_2S:Eu^{3+}$ (0.5 mole %) and $Gd_2O_2S:Eu^{3+}$ (0.5 mole %) measured at 2 kV and 30 μA/cm^2.

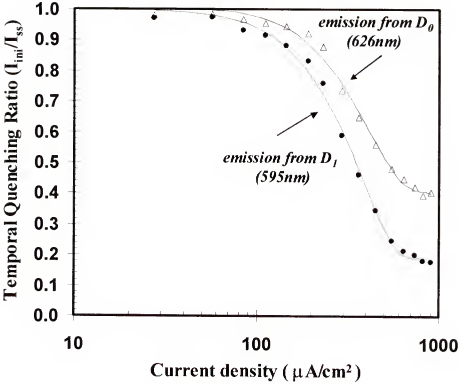

Figure 5-2. Temporal CL quenching factors versus electron beam current densities for the $^5D_0$=>$^7F_2$ (626 nm) or $^5D_1$=>$^7F_3$ (591 nm) transition of $La_2O_2S:Eu^{3+}$ (0.1 mole %) measured at 2 kV.

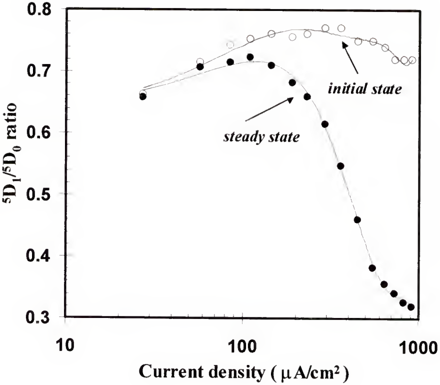

Figure 5-3. The initial (t = t_{ini}) and steady (t = t_{quench}) state peak height ratio, $^5D_I/^5D_0$, observed from $La_2O_2S:Eu^{3+}$ (0.1 mole %) as a function of electron beam current density at 2 kV.

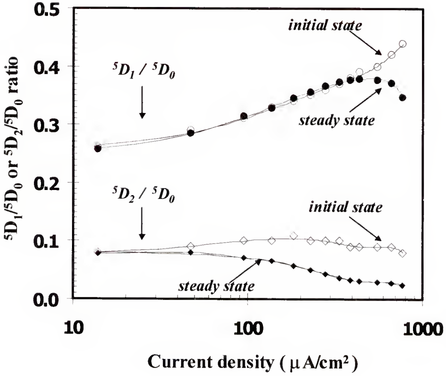

Figure 5-4. The initial (t = 0) and steady (t = t_{quench}) state peak height ratios, $^5D_1/^5D_0$ and $^5D_2/^5D_0$, observed from $Gd_2O_2S:Eu^{3+}$ (0.4 mole %) as a function of electron beam current density at 2 kV.

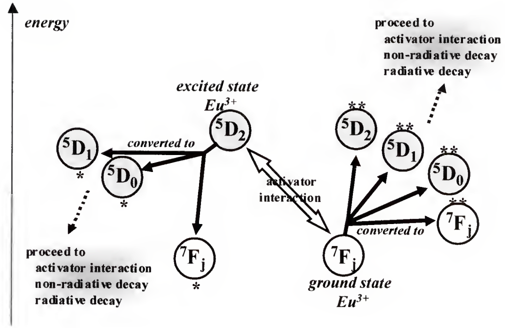

Figure 5-5. A schematic diagram of activator interaction between an excited and ground state Eu^{3+} activator. The markers, * and **, show the energy states of activators after interaction.

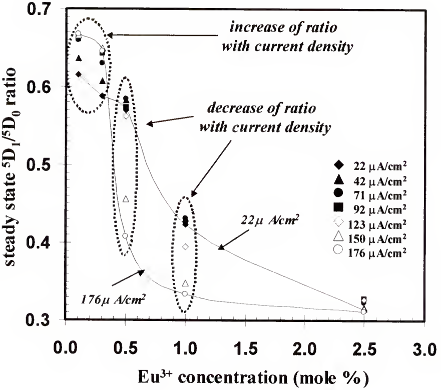

Figure 5-6. The steady state peak height ratio, $^5D_1/^5D_0$, versus Eu^{3+} concentration observed from $La_2O_2S:Eu^{3+}$ at 2 kV and 22 ~ 176 μA/cm^2.

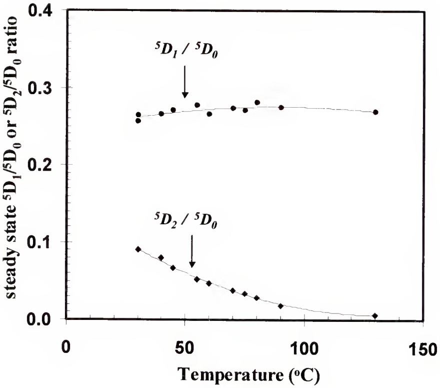

Figure 5-7. Temperature dependence of the steady state peak height ratio, ${}^5D_1/{}^5D_0$ and ${}^5D_2/{}^5D_0$, from $Gd_2O_2S:Eu^{3+}$ (0.4 mole %). (2 kV, 15 μA/cm^2)

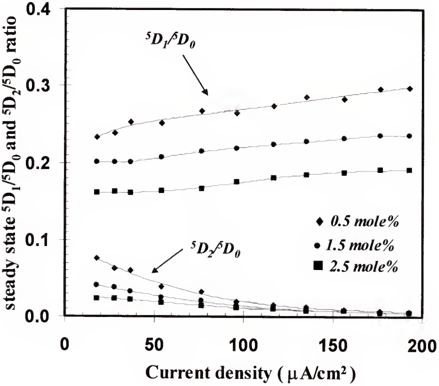

Figure 5-8. The steady state peak height ratio, $^5D_1/^5D_0$ and $^5D_2/^5D_0$, observed from $Gd_2O_2S:Eu^{3+}$ (0.5, 1.5 and 2.5 mole %) as a function of electron beam current density at 2 kV.

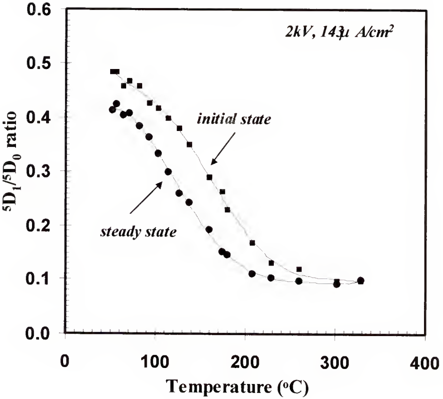

Figure 5-9. Temperature dependence of the initial and steady state peak height ratio, $^5D_1/^5D_0$, from $La_2O_2S:Eu^{3+}$ (0.5 mole %). (2 kV, 143 μA/cm^2)

CHAPTER 6
EFFECTS OF COATINGS ON TEMPORAL CATHODOLUMINESCENCE QUENCHING IN ZnS:Ag,Cl PHOSPHORS

6.1 Introduction

Upon reducing the FED operating voltage from 15~30 kV to 2 kV, the phosphor efficiency drops by more than a factor of ten. In order for FEDs to achieve brightness comparable to CRTs, the current density must be increased. At high current densities, FED phosphors suffer from quenching of both the CL brightness and efficiency. While the CL intensity is constant at low excitation densities, the intensities decreases with time at high excitation densities, as shown schematically in Fig. 6-1. The time to reach the initial maximum CL intensity (t_{ini}), the time to quench (t_{quench}) the initial intensity (I_{ini}) to the steady state intensity (I_{ss}), and the ratio of I_{ss}/I_{ini} can be defined as shown in Fig. 6-1. The value of t_{ini} is in the range of nanoseconds to milliseconds, and the initial or maximum CL intensity and corresponding time dependence is a function of activator concentration, density of non-radiative center, excitation density and temperature. In contrast to the rise to I_{ini}, it takes several seconds for the emission intensity to fall to the steady state value due to a variety of reasons such as electron beam heating and effects of induced internal electric field [BAN03]. The effects of coatings on the temporal CL quenching of ZnS:Ag,Cl powder phosphors from I_{ini} to I_{ss} at low and high current densities are reported and discussed in this paper.

6.2 Experimental Section

6.2.1 Surface Modification of ZnS:Ag,Cl Phosphors

Powdered ZnS:Ag,Cl (Osram Sylvania, type1330) phosphors were coated with commercial SiO_2, SnO_2 or Al_2O_3 by mixing the phosphor with colloidal silica or dispersed particles (SnO_2 or Al_2O_3) in a MeOH slurry, centrifuging and drying in air at 120 °C. Table 6-1 shows some properties of the coating materials.

6.2.2 Characterization

Coatings on the phosphor surface were examined using a JEOL model 6400scanning electron microscope (SEM). For CL measurements, the powder samples were pressed into 4 mm deep, 6 mm diameter holes in a stainless steel holder and excited by a 2 kV, 50 to 800 $\mu A/cm^2$ electron beam from the coaxial electron gun in a PHI Model 545 scanning Auger electron spectrometer (AES). The emission spectrum and peak intensities were measured in reflection using an Oriel 77400 Multi-spectrometer with a CCD array detector. For temporal CL quenching, data were acquired every 0.15 sec during electron beam irradiation. Auger data were collected with the cylindrical mirror analyzer of the Auger electron spectrometer. For PL measurements, powder samples pressed into 2 mm deep, 3 mm wide holes in a stainless steel holder were excited by 325 nm UV light from an Omnichrome HeCd laser (Model 74, 30 mW). The emission spectra were measured in reflection using an Instruments SA monochromator (Model HR-320, 0.3 m) and Hamamatsu GaAs photomultiplier tube (Model R943-02). In addition, PL decay times were measured with 8 nsec pulsed excitation by the third-harmonic of a Nd:YAG laser (335nm) and a multichannel plate (MCP) CCD array detector having a gate delay of 1 μsec and gate width of 100 μsec. CL decay times were measured with a 50 μsec pulsed electron beam and PMT having a response time of 40 nsec.

6.3 Results and Discussion

6.3.1 Morphology and Luminescence of Oxides Coated ZnS:Ag,Cl

Fig. 6-2 shows a scanning electron microscope (SEM) image of a discontinuous nanoparticulate coating of SiO_2 (average nanoparticle size of 130 nm) on ZnS:Ag,Cl powder phosphors (average powder particle size ~ 5 μm). Fig. 6-3 shows the CL and PL emission spectra from non-coated and 130 nm SiO_2 nanoparticle coated ZnS:Ag,Cl powder phosphors. As shown in Fig. 6-3, there was no difference in CL and PL spectrum before and after coating. However the PL spectrum showed only one emission band with a 445 nm peak, while the CL spectrum showed two emission bands. Peak de-convolution showed one CL emission band was at 445 nm and the second was at 480 nm. Also, the emission band at 480 nm retained a greater intensity as compared to the emission band at 445 nm upon an increase of temperature. Two kinds of blue emission have been reported previously from ZnS host phosphors [OZA90]. A peak at 455 nm is reported to be from a radiative acceptor-donor recombination between $Ag^{2+}(Zn)$ and $Cl^{2-}(S)$, while a 473 nm peak results from recombination between $V^{3+}(Zn)$ and $Cl^{2-}(S)$. The latter is known as self activated luminescence [OZA90, SHI98]. The ratio of these two blue emission peaks is known to control emission color and brightness for CRT phosphors. Therefore, the two de-convoluted emission bands at 445 nm and 480 nm are assigned to these two mechanisms. The difference in emission between CL and PL can be understood from the difference in the penetration depths of an electron beam versus an UV photon. For ZnS, the penetration range of an primary electron beam may be calculated from $R_p = K(E_b)^a$ where K = 16.95 and a = 1.541 [YAN98a] and is found to be ~50 nm at 2 kV. In contrast, the UV absorption range is known to be ~ 1 μm [OZA90]. Therefore, if radiative centers such as Zn vacancies (defects) are concentrated near the surface, they should influence the CL spectrum more than the PL spectrum. In addition, non-radiative centers, such as dangling bonds, could be concentrated near the surface.

6.3.2 Temporal CL Quenching from Oxides Coated ZnS:Ag,Cl

The temporal dependence of CL emission intensity was measured versus current densities for the ZnS:Ag,Cl powder phosphors. As shown in Fig. 6-4(a), the emission intensity of non-coated ZnS:Ag,Cl powder phosphors did not change during an electron beam irradiation either at low (72 $\mu A/cm^2$) or high (564 $\mu A/cm^2$) current densities. Fig. 6-4(b) shows that both the initial and steady state CL emission intensities increased nearly linearly as a function of current density. However, 130 nm nanoparticulate SiO_2 coated ZnS:Ag,Cl behaved very differently, as shown in Fig. 6-5(a). While the emission intensity did not change with time at low current densities (72 $\mu A/cm^2$, 2 kV), it did decay over the first ~ 15 seconds and approach a steady state intensity at high current densities (564 $\mu A/cm^2$, 2 kV). Fig. 6-5(b) shows the initial (I_{ini}) and steady state (I_{ss}) emission intensity as a function of current density. The initial intensity monotonically increases as current density increases, whereas the steady state intensity initially increases but decreases above current densities of ~ 300 $\mu A/cm^2$. From the initial and steady state intensities, the temporal quenching factor (I_{ss}/I_{ini}) versus current densities were calculated for non-coated and 130 nm nanoparticulate SiO_2 coated ZnS:Ag,Cl powder phosphors. As shown in Fig. 6-6(a), the amount of quenching increases (i.e., decrease of temporal quenching factor) with an increase of current density for 130 nm nanoparticulate SiO_2 coated ZnS:Ag,Cl powder phosphors, while the factor remained at unity for non-coated phosphor. In addition, ZnS:Ag,Cl coated with SiO_2 (22 nm nanoparticles), SnO_2 or Al_2O_3, and commercial ZnS:Ag,Cl phosphors coated with SiO_2 (produced by Kasei) all show very similar temporal CL quenching behaviors. Even though the value of the temporal quenching factors versus current densities are slightly different for each coated phosphor, they are in the range of 0.1 ~ 0.3 with a quenching time of ~ 15 seconds at 2kV and 600 $\mu A/cm^2$, as shown in Fig. 6-6(b). Bang et al. [BAN03] showed that temporal CL quenching of $La_2O_2S:Eu^{3+}$ powder phosphors with increasing current density resulted from several effects, one of which was thermal quenching due to electron beam heating. Since thermal quenching could not explain all of the CL quenching, Bang et al. [BAN03] suggested that other factors were important, including (1) localized redistribution of charge carriers by the induced internal electron field and the subsequent increased activator interactions, and (2) different effects of the induced internal electric field on the activator interaction for different excited ^5D_j state of the Eu^{3+} activators.

Coatings on phosphor surfaces could affect both the thermal conductivity of packed powders and their emissivity, leading to changes of the steady state temperature and thermal quenching under electron beam bombardment. Yamamoto et al. [YAM91] reported that a potassium silicate coating on $InBO_3:Tb^{3+}$ powder phosphors decreased the packing density with a subsequent increase of surface temperature in the sedimented phosphor layer under electron beam bombardment. The packing density decreased from 2.5 to 1.8 g/cm^3 and the measured surface temperature increased from 220 °C to 250 °C with the silicate coating.

The temperature rise due to electron beam heating can be calculated using the Stefan equation by assuming heat is only lost by radiation from a black body, i.e., neglecting conduction in the packed powder bed and molecular transport in the vacuum [GES68]. The maximum temperature (T_2) under electron beam irradiation is expressed as [BAN03]

$$T_2 = \{Q_e / (\sigma\ \varepsilon\ 4\pi r^2) + T_1^4\}^{1/4}$$

$$= \{E_b\ I / (4\ \sigma\ \varepsilon) + T_1^4\}^{1/4}$$

where Q_e = power added to a particle from the electron beam (W), σ = Stefan-Boltzmann constant (5.67 x 10^{-8} W/m^{2}K^4), ε = emissivity of phosphor (unitless, 1 for black body radiation), r = radius of the particle (m), T_1 = temperature of a particle before electron beam bombardment (K), E_b = electron beam voltage (V) and I = electron beam current density (A/m^2). The maximum temperature attainable in ZnS:Ag,Cl with an electron beam of 2 kV, 600 μA/cm^2 is 200 °C. The degree of thermal quenching from electron beam heating can be estimated based on the reported activation energy for thermal quenching, i.e. 0.52 eV [ABR01], and the following equation [BHU88].

$$I(T_2) / I(T_1) = 1 / \{1 + C \exp(-E_a/k(1/T_2-1/T_1))\}$$

where I = emission intensity, E_a = activation energy for thermal quenching and k = Boltzman constant (8.616 x 10^{-5} eV/K). The estimated intensity of the thermal quenching factor for the calculated maximum attainable temperature of 200 °C is 0.40, i.e., I(200°C)/I(RT) = 0.4. However, the normalized steady state emission intensity (i.e., temporal quenching factor) of SiO_2, SnO_2 or Al_2O_3 coated phosphors were between 0.1 and 0.3 at 2 kV, 600 μA/cm^2. Thus the different quenching behavior of coated versus non-coated ZnS:Ag,Cl powder phosphors can only be partially explained by electron beam heating. Furthermore, as shown in Fig. 6-6(a), the emission intensity of non-coated ZnS:Ag,Cl powder phosphors did not change over the first ~ 15 sec. (i.e., over the time that coated phosphors approached steady state emission intensities). If thermal quenching is occurring, the lack of intensity quenching for non-coated ZnS:Ag,Cl suggests that any electron beam heating was completed in times << 1 sec and therefore only affects the initial state emission intensity. Presumably, the temperature difference between non-coated and coated phosphors is not large, and it is concluded that electron beam heating effects are minor in temporal CL quenching of coated ZnS:Ag,Cl powder phosphors.

6.3.3 Effects of Induced Internal Electric Fields and Surface Voltages

Figure 6-7 shows a schematic diagram of the development of charging and internal electric fields that can develop in the phosphor particles. An incident electron beam loses its energy through inelastic interactions with the electrons of the solid host material and activators, producing a large concentration of 'free' electron and hole charge carriers over the electron penetration range. In addition, secondary and Auger electron emission from the phosphor creates an unbalance in the charge at the surface (Q_s) versus the charge at the end-of-range (Q_{eor}). In general, the end-of-range charge is negative relative to the surface charge due to penetration and stopping of the incident electron beam. This will create an internal electric field (E_{int}) shown in Fig. 6-7, that will move electrons towards the surface and holes away from the surface, i.e., will result in a separation of charge carriers. In addition, if we assume that i_p electrons penetrate into solid, i_s secondary or Auger electrons are emitted from the surface, i_g electrons flow to ground, and before steady state operation is established that $i_p > (i_s + i_g)$, a negative charge, ΔQ, will accumulate on the sample and induce a surface voltage (V_s) relative to ground. The internal electric field, E_{int}, will depend on the electron beam current density, and the charges (Q_{eor} and Q_s) will recombine rapidly after the electron beam is turned off. The surface voltage (V_s) will depend on the charge unbalance between Q_{eor} and Q_s (i.e., ΔQ)

and will again "bleed off" when the electron beam is turned off. The magnitude of V_s, plus the rate of "bleed off" will depend on temperature, electrical conductivity and the degree of contact between particles. Similar to this model, Seager et al. [SEA97] also suggested that substantial space charge is present in the phosphors without an induced surface potential, i.e., E_{int} without significant V_s.

During continuous electron beam irradiation for ~ 6 hr on ZnS:Ag,Cl phosphor coated with 130 nm nanoparticle SiO_2, the electron beam of 2 kV, 330 $\mu A/cm^2$ was turned off for ~ 1 to 2 sec at coulombic doses of $Q_L = 0, 0.72, 1.53, 3.83$ and $5.73\ C/cm^2$ in order to measure the temporal CL quenching behavior versus electron fluence. Fig. 6-8 shows the initial and steady state emission intensities as a function of electron fluence (in Coulombs/cm^2). In addition to the CL intensity, the energy shift for the 152 eV S Auger peak, which is a measure of V_s, is also shown. Without prior exposure to the electron beam, i.e., for $Q_L = 0\ C/cm^2$, there was no charging (i.e., no shift of the S Auger peak), but there was significant (~ 28%) quenching of the steady state CL intensity versus the initial intensity. Greeff et al. [GRE02, SWA99] reported that charge-induced electric fields would separate electrons and holes with a subsequent decrease of radiative recombination. However, our results showed that CL emission intensity decreased over ~ 15 seconds without a measurable V_s. This result implies that an induced internal electric field exists independent of the existence of uncompensated charge, i.e., even when $\Delta Q = 0$, and supports the existence of E_{int}, as shown in Fig. 6-7. The significant temporal CL quenching at $Q_L = 0\ C/cm^2$ is a result of the development of the internal electric field, E_{int}. With an increase of coulombic loading, Q_L, to ~ 5.7 C/cm^2, charging increased V_s to ~ 2.6 eV and both the initial and steady state CL intensities decreased. Negative surface charging could potentially change CL emission intensities by a reduction of the incident electron beam energy (at large V_s), but the reduction in primary beam energy from surface charging (from 2000 V at $Q_L = \sim 0$ C/cm^2 to 1997.5 V at $Q_L = 5.8$ C/cm^2 as shown in Fig. 6-8.) is too small to be significant. Note that the temporal quenching factor (i.e., steady state emission intensity divided by initial state emission intensity) is smaller (temporal quenching is larger) at larger coulombic loading (e.g., 0.72 at $Q_L = 0$ C/cm^2 and 0.55 at $Q_L = 5.73$ C/cm^2). Assuming that E_{int} is independent of coulombic loading, and therefore that this contribution to the temporal quenching factor is constant, the 'projected' steady state emission intensity affected only by E_{int} (i.e. I_{ss}^{Eint}) was calculated, and is shown in Fig. 6-8. Here $I_{ss}^{Eint} = I_{ini}^{QL} \times 0.72$ and I_{ini}^{QL} is the initial intensity after a Coulombic loading of Q_L, and 0.72 is the temporal quenching factor at $Q_L = 0$. The decrease of the initial and this 'projected' steady state emission intensity versus Coulombic loads shows the real degradation of phosphor (i.e., decrease of CL intensity) due to electron stimulated surface chemical reactions (ESSCRs) [HOL00a, HOL00b]. The difference between the measured and projected I_{ss} (i.e., change of temporal quenching factors as a function of electron fluence) could result from changes in the induced internal electric fields, E_{int}, by ΔQ (i.e., development of V_s), and/or from phosphor degradation. Surface dead layers formed during prolonged electron beam irradiation could change the concentration of non-radiative surface centers, induced internal electric fields, and/or surface recombination velocities. The value of V_s at $Q_L > 0$ (e.g., ~2.6 eV at $Q_L = \sim 5.7$ C/cm^2) was nearly constant over the temporal quenching times of ~15 sec. (e.g., $dV_s/dt \sim 0.14$ mV/sec over the 15 sec in Fig. 6-8.), therefore the changes in the induced internal electric fields due to the development of V_s had a negligible effect on the temporal CL quenching factors, consistent with previous results [BAN03]. Therefore it is suggested that the creation of a surface dead layer by phosphor degradation affects the temporal CL quenching factors as a function of electron fluence.

6.3.4 Effects of Nonradiative Surface Centers

The data in Fig. 6-8 showed that E_{int} was the major contributor to the temporal CL quenching of coated ZnS:Ag,Cl powder phosphors. But, E_{int} would potentially be induced in both non-coated and coated ZnS:Ag,Cl powder phosphors. This suggests that other differences between non-coated and coated ZnS:Ag,Cl powder phosphors affect the temporal CL quenching.

An incident electron beam produces large concentrations of electron and hole charge carriers along with directly excited activators within the electron penetration range. Some of the electrons and holes recombine at defects acting as non-radiative centers, while the remaining carriers transfer the recombination energy to the activator. Excited activators lose their energy via three routes: luminescent decay, non-radiative decay (e.g., multi-phonon relaxation or energy transfer to non-radiative centers), or interactions (i.e., energy transfer) with a neighboring activator (in either an excited or ground state). During a series of activator interactions, interaction quenching will occur if the energy is eventually transferred to a non-radiative center or an excited state that decays non-radiatively. Consistent with this model, Dexter et al. [DEX54] explained concentration quenching as the migration of excitation energy from one activator center to another, and eventually to an imperfection that may act as an energy sink. Interaction quenching has also been explained in other ways. Kuboniwa et al. [KUB80, ZAK91] attributed it to three center Auger recombination (TCAR) to explain luminescence saturation of ZnS:Cu,Al phosphors versus increased current density with a high beam voltage (15kV).

Taylor [TAY62] reported quenching of α particle scintillation in ZnS crystal by the application of an electric field and explained the phenomena using selective extraction of holes from radiative center and recombination of electron with trapped holes at non-radiative center. In the present case of CL excited by a low energy electron beam, it appears that non-radiative centers affect the intensity both by electron-hole recombination at non-radiative center before carriers are trapped on donor-acceptor sites, and by energy transfer from excited activators to non-radiative center (i.e., interaction quenching). For the former, CL emission quenching rates are directly proportional to the concentrations of non-radiative centers. However, the CL emission quenching rates for the latter are proportional to the rate of activator interaction multiplied by the concentrations of non-radiative centers. Note that the increase of non-radiative center implies the decrease of excited activators with the subsequent decreases of activator interaction rate. Therefore, the rate of interaction quenching should decrease at higher concentrations of non-radiative centers.

This discussion leads to the conclusion that coated ZnS:Ag,Cl phosphors have higher densities of non-radiative surface centers than non-coated ZnS:Ag,Cl powder phosphors, relatively independent of the type of coating (Table 6-1). Since the concentration of non-radiative centers is known to affect the time constant for relaxation of the radiative intensity, this parameter was measured for coated and non-coated ZnS:Ag,Cl powder phosphors. The CL and PL emission intensity decay with time of non-coated and 130 nm nanoparticulate SiO_2 coated ZnS:Ag,Cl phosphors (Fig. 6-9) show that the luminescence decays were non-exponential and the time constants decrease with coating. Specifically, the time to decay to 0.2 of the initial intensity was 28 versus 37, 38 versus 42, and 55 versus 55 μsec for coated versus non-coated ZnS:Ag,Cl excited by 1 kV or 4kV electron beams or by UV photons, respectively. In addition, the decay time constant increased with increasing penetration depth (i.e., ~17 nm, ~140 nm and ~1 μm for 1kV and 4kV electrons and UV photons, respectively) [OZA90, YAN98a] consistent with the concentration of non-radiative centers being higher at the surface and higher on the coated phosphors.

To further evaluate the effects of surface conditions, Fig. 6-10(a) shows the temporal quenching factors of non-coated ZnS:Ag,Cl powder phosphors that were heat-treated at 300 °C or 500 °C for 3 hr in air. While phosphors heated to 300 °C did not, those heated to 500 °C did show temporal quenching similarly to the coated phosphors (~ 0.1 at 2 kV, 500 μA/cm^2). In addition, the initial CL emission intensity from non-coated ZnS:Ag,Cl powders that were heat-treated at 500 °C was 30 % (at 2 kV, 500 μA/cm^2) of that from non-coated ZnS:Ag,Cl powder phosphors (without heat treatment). As shown in the Auger electron spectrum of Fig. 6-10(b), there was a significant decrease of the S and an increase of the O Auger peak for non-coated ZnS:Ag,Cl powders that were heat-treated at 500 °C. In addition, XRD data showed that $Zn_3O(SO_4)_2$ formed during this 500 °C heat treatment, and it is postulated that this surface layer creates non-radiative centers that contribute to temporal CL quenching. These results support the conclusion that generation of non-radiative surface center by coating results in temporal CL quenching of coated ZnS:Ag,Cl phosphors at high current density. Of course, the presence of $Zn_3O(SO_4)_2$ on surfaces could also affect the value of E_{int}, as discussed below.

Degradation of ZnS:Ag,Cl powder phosphors under prolonged electron beam irradiation is known to result from formation of non-radiative surface layers such as ZnO dead layers by ESSCRs [HOL00a], defects by removal of radiative center[IGA02], or deterioration of crystallinity [KAJ03]. Data in Fig. 6-10 also suggest that phosphor degradation will affect temporal CL quenching after prolonged electron beam irradiation. Therefore, the temporal CL quenching fractions labeled A and B in Fig. 6-8, result from the effect of E_{int} in combination with non-radiative surface centers due to coating, and due to electron beam induced degradation, respectively.

6.3.5 Nonradiative Surface Recombination under Internal Electric Fields

From the above results, induced internal electric fields, E_{int}, and non-radiative surface centers are concluded to be the important factors leading to temporal CL quenching of coated ZnS:Ag,Cl powder phosphors. Generation of an electric field internal to the phosphor and its affect on diffusion of generated electron and hole charge carriers [YAN98a] are believed to be the mechanism for the temporal CL quenching and the dependence upon increasing current density. As soon as E_{int} forms, generated charge carriers start to redistribute under its influence until conditions finally reach steady state, at which no further CL changes are observed with time. Because electrons in ZnS have a much higher mobility as compared to holes (165 vs. 5 $cm^2/Vsec$) [SZE81], electrons will be affected more by E_{int}. Therefore electrons excited to the conduction band inside the electron penetration range will move preferentially towards the surface, since E_{int} will point from the surface (the surface is more positive due to emission of secondary electrons) towards the end-of-range of the electron. Seager [SEA98] reported that there was a change in the transient and steady state CL intensity with an applied external electric field due to electrons moving to the surface. This explanation assumes that capture of electrons at non-radiative surface states is the rate limiting step, and that many defects existed on the surface. Therefore, surface localization of generated electrons by

E_{int} would result in an increase of non-radiative surface recombination. The rate of non-radiative surface recombination would be expected to be higher as the electron beam current density was increased because of larger E_{int} and consequent faster transport of generated electrons to the surface. In the case of small concentrations of non-radiative centers at the surface (e.g., non-coated ZnS:Ag,Cl phosphor), non-radiative surface recombination rates would not be affected much by the localization of generated electrons. However, high concentrations of non-radiative centers at the surface (e.g., coated, electron beam-degraded, or heat-treated ZnS:Ag,Cl phosphor) will trap and localize electrons at a fast rate, resulting in the temporal CL quenching over the first ~ 15 sec. as shown in Fig. 6-5(a) and Fig. 6-10(a).

Note that the creation of a non-radiative surface dead layer during phosphor degradation or heat-treatment in air could also affect E_{int}. This is reasonable since the dead layer is known to be an oxide under these conditions, and a surface oxide layer would affect E_{int} by modifying the secondary electron emission, surface dielectric constant, and potentially the range and trapping of charge carriers. In addition, the coating material and non-radiative surface centers formed by surface coating would affect E_{int}. Therefore, any changes of E_{int} by coating materials and/or non-radiative surface centers/layers are postulated to enhance the non-radiative surface recombination rates, and lead to temporal CL quenching. Thus, changes in E_{int} in combination with changes in the concentration/character of non-radiative surface recombination centers are concluded to be important to temporal CL quenching of ZnS:Ag,Cl. The present data are not sufficient to determine whether one of these factors is predominant in causing this temporal CL quenching.

Bang, et. al. [BAN03] have reported that non-coated $La_2O_2S:Eu^{3+}$ and $Gda_2O_2S:Eu^{3+}$ powder phosphors show temporal CL quenching with increasing current density, whereas the present data show that non-coated ZnS:Ag,Cl powder phosphors do not exhibit temporal quenching. An induced internal electric field and subsequent increased activator interaction (i.e., interaction quenching) was suggested to be one of the reasons for temporal CL quenching of $Ln_2O_2S:Eu^{3+}$ powder phosphors. For a large density of non-radiative surface center (e.g., on coated ZnS:Ag,Cl phosphors), interaction quenching at high current densities is not anticipated due to the decreased concentration of excited activators by electron-hole recombination at non-radiative surface centers. Instead, increased electron-hole pair recombination at non-radiative surface centers under induced internal electric field is suggested to be the main reason for temporal CL quenching in coated ZnS:Ag,Cl phosphors. However, interaction quenching at high current densities would be anticipated even for a low concentration of non-radiative surface center (e.g., non-coated ZnS:Ag,Cl phosphors), presumably at higher current densities (i.e., >> 800 $\mu A/cm^2$) than those used in this experiment. The fact that activator interactions occur at lower current densities for non-coated $Ln_2O_2S:Eu^{3+}$ (Ln = La and Gd) than for ZnS:Ag,Cl powder phosphors may result from differences in the distance between activators. The activator concentration is a few mole percent for $Ln_2O_2S:Eu^{3+}$ versus 0.005 ~ 0.01 mole % for commercial ZnS:Ag,Cl phosphor. In addition, the induced internal electric field, E_{int}, and surface recombination velocities would be different for the different phosphors, leading to different mechanisms dominating the temporal CL quenching.

6.4 Conclusion

At high current density (e.g., 600 μA/cm^2, 2 kV), the CL emission intensity of ZnS:Ag,Cl powder phosphors coated with nanoparticulate SiO_2 (22 or 130 nm sized), SnO_2 or Al_2O_3 decayed by factors ranging from 70 % to 90 % (i.e., temporal quenching factors ranging from 0.3 to 0.1) over the first ~ 15 seconds of electron beam irradiation. This temporal CL quenching was shown to be consistent with an increase in the concentrations of non-radiative surface centers during surface coating, and/or enhanced non-radiative surface recombination induced by internal electric fields during CL. The internal electric field presumably resulted from the accumulation of primary electrons at the end of their penetration range and emission of secondary electrons from the surface. Localization of electrons at the surface due to the induced internal electric field, leads to higher non-radiative surface recombination rates between electrons and holes with a subsequent decrease of emission intensity. Based on temporal quenching even in the absence of an energy shift for Auger electrons, it was suggested that development of a surface potential on the phosphor did not result in significant temporal quenching. In addition, non-radiative surface layers formed during prolonged electron bombardment of coated phosphors or during heat treatment of non-coated phosphor also led to increased temporal CL quenching.

Table 6-1. Properties of coating materials

coating material	SiO_2	SiO_2	SnO_2	Al_2O_3
source	DevMer 4wt% sol'n	Dupont Ludox TM-A	Nanophase co. SN80810-RRX	Nanogram co. HDR ALO-98NP
size	130nm	22nm	15nm	70nm
coating amount	0.3wt%	0.3wt%	0.3wt%	0.3wt%

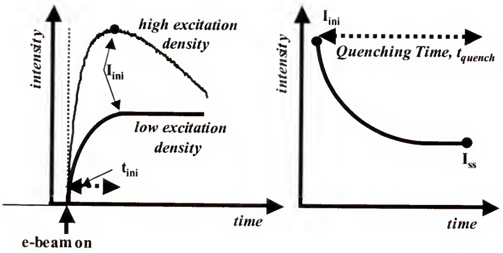

Figure 6-1. Schematic diagrams showing emission intensities versus time at low and high excitation density (left) and temporal CL quenching behavior (right).

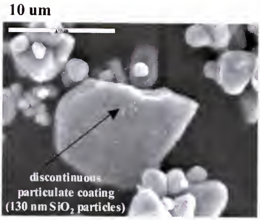

Figure 6-2. A SEM image of SiO_2 (130 nm sized) coated ZnS:Ag,Cl powder phosphors. (Scale bar: 10 μm)

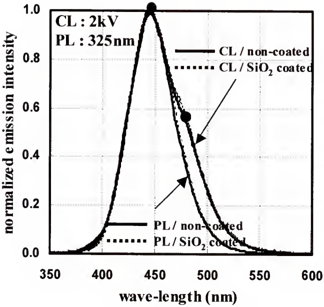

Figure 6-3. Cathodoluminescence (2 kV and 70 μA/cm^2) and photoluminescence (λ_{exc} = 325 nm) spectra of non-coated and SiO_2 (130 nm sized) coated ZnS:Ag,Cl powder phosphors.

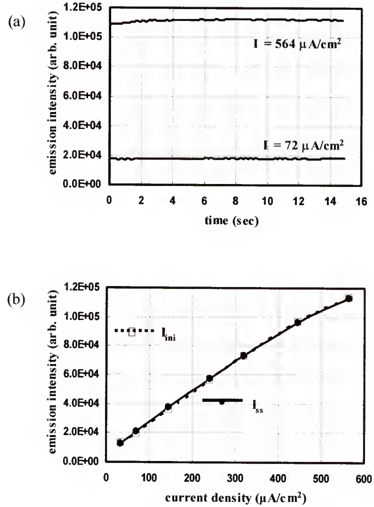

Figure 6-4. Emission intensity from non-coated ZnS:Ag,Cl versus time or current density. (a) The temporal behavior of emission from non-coated ZnS:Ag,Cl powder phosphors after incidence of a 2 kV DC electron beam. Each current density was 72 or 564 μA/cm^2. (b) The initial and steady state emission intensity from non-coated ZnS:Ag,Cl powder phosphors as a function of electron beam current density. The electron beam energy was 2 kV.

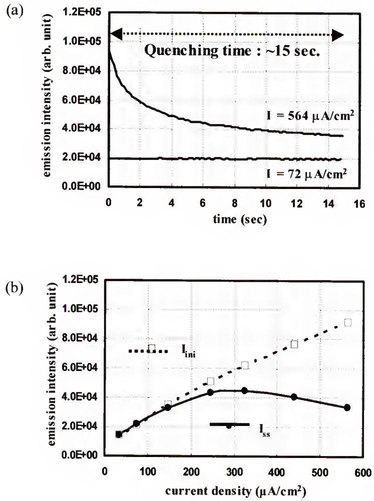

Figure 6-5. Emission intensity from coated ZnS:Ag,Cl versus time or current density. (a) The temporal behavior of emission from SiO_2 (130 nm sized) coated ZnS:Ag,Cl powder phosphors after incidence of a 2 kV DC electron beam. Each current density was 72 or 564 $\mu A/cm^2$. (b) The initial and steady state emission intensity from SiO_2 (130 nm sized) coated ZnS:Ag,Cl powder phosphors as a function of electron beam current density. The electron beam energy was 2 kV.

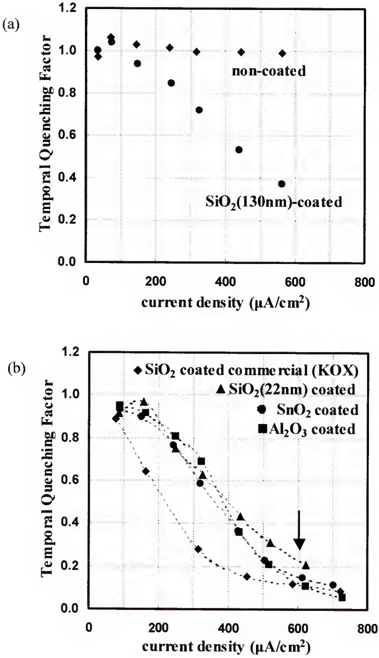

Figure 6-6. Temporal quenching factors versus current density. (a) Temporal quenching factors versus current density of non-coated and SiO_2 (130 nm sized) coated ZnS:Ag,Cl powder phosphors. (b) Temporal quenching factors versus current density of ZnS:Ag,Cl coated with SiO_2 (22 nm nanoparticles), SnO_2 or Al_2O_3, and commercial ZnS:Ag,Cl phosphors coated with SiO_2 (produced by Kasei).

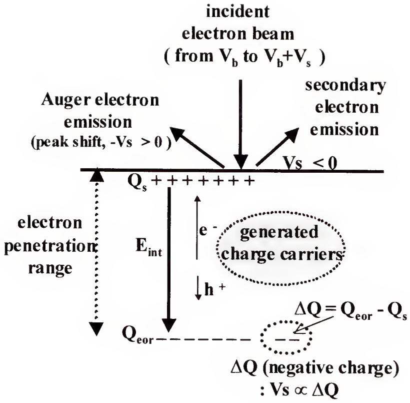

Figure 6-7. A schematic diagram of charging and induced internal electric field during electron beam bombardment.

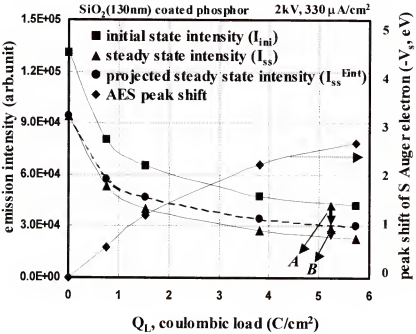

Figure 6-8. The initial and steady state emission intensity and peak shift of S Auger electron at each coulombic load (2 kV, 330 μA/cm^2). For the measurement of temporal emission behaviors, an electron beam was shortly turned off during electron beam irradiation on SiO_2 (130 nm sized) coated ZnS:Ag,Cl powder phosphors.

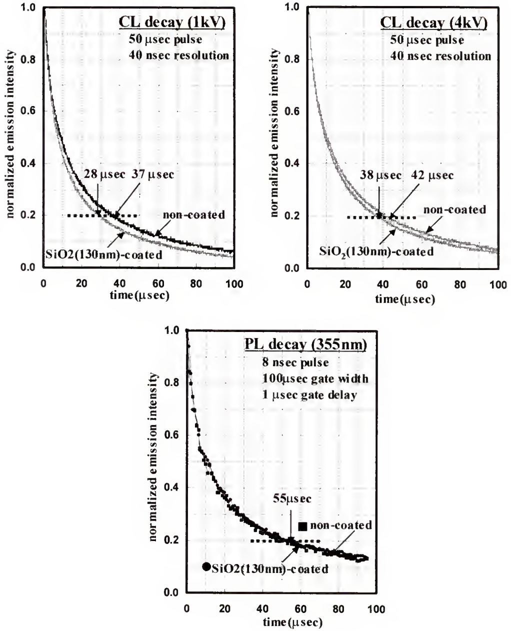

Figure 6-9. CL (E_b = 1 and 4 kV) and PL (λ_{exc} = 335nm) decay curves of non-coated and SiO_2 (130 nm sized) coated ZnS:Ag,Cl powder phosphors. (left: CL at 1 kV, middle: CL at 4 kV , right: PL)

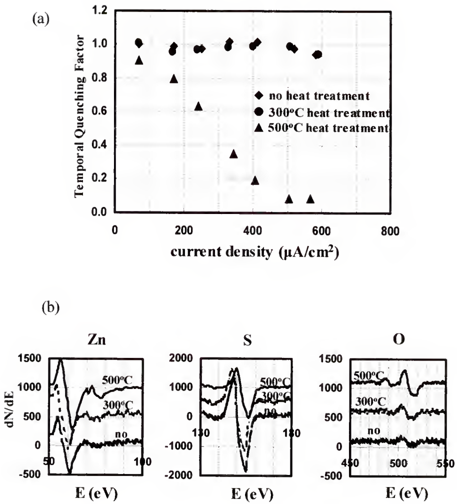

Figure 6-10. Temporal CL quenching and Auger electron spectra of heat-treated phosphors. (a) Temporal quenching factors versus current density of non-coated ZnS:Ag,Cl powder phosphors, which were heat-treated at 300 °C or 500 °C for 3 hr in air. The electron beam energy was 2 kV. (b) Auger electron spectra of non-coated ZnS:Ag,Cl powder phosphors, which were heat-treated at 300 °C or 500 °C for 3 hr in air. The electron beam energy was 2 kV. (left: Zn, middle: S, right: O)

CHAPTER 7
ENHANCED GREEN EMISSION FROM ZnO NANOPARTICLES BY SURFACE SEGREGATION OF Mg

7.1 Introduction

There has been increased interest in the scientific and technological aspects of nanometer-sized particles. These particles exhibit unique chemical and physical properties, differing substantially from those of the corresponding bulk solids [MUR00]. These differences are associated with the quantum confinement effect and existence of a relatively large percentage of atoms at the surface. From the viewpoint of luminescence, large surface results in large concentrations of surface defects, which may serve as nonradiative and radiative centers. It is known that green emission from ZnO is a defect emission resulting from oxygen vacancies [STU02, VAN96]. Previously green emission from ZnO nanoparticles was reported even without introduction of oxygen vacancies by heat treatment in H_2, suggesting that radiative oxygen vacancies are naturally present on the large surface area of ZnO nanoparticles.

It is also known that non-equilibrium $Zn_{1-x}Mg_xO$ ($x = 0 \sim 0.37$) thin films show bandgap widening from 3.3 eV to 4.3 eV as x increases [TAK03, MAT99]. If $Zn_{1-x}Mg_xO$ nanoparticles with a size less that the Bohr radius can be achieved, they will provide large window for bandgap tailoring plus quantum confinement shifts for luminescent applications. Alternatively, it is known that the surface properties of nanoparticles can be dramatically altered by surface segregation of elements, or even creations of a surface shell layer (e.g., MgO) over a core of a different composition (e.g., ZnO).

The formation of ZnO nanoparticles and the effects of Mg addition on green emission (i.e., defect emission) from ZnO nanoparticles were investigated in this study. A red shift of the green emission to ~ 600 nm will be reported from ZnO nanoparticles. In addition, new defect emissions will also be reported. The effect of precipitation medium on the luminescence from ZnO nanoparticles also will be discussed.

7.2 Experimental Section

7.2.1 Synthesis of Nanoparticles: ZnO and ZnO with Mg

Suspensions of ZnO nanoparticles was prepared by precipitation from $Zn(CH_3COO)_2$ and NaOH, as reported previously [MEU98, WON98]. For a typical preparation, 0.459g of $Zn(CH_3COO)_2$ and 0.2 g of NaOH were dissolved in 30 ml and 10 ml EtOH, respectively, with heating to ~70 °C. After preparation of, the OH^- solution was added into the Zn^{2+} solution in an ice bath with vigorous stirring. For preparation of suspended nanoparticles of ZnO with Mg (Zn:Mg = 9:1), 0.036g of $Mg(CH_3COO)_2$ dissolved in 5 ml EtOH was mixed into the Zn^{2+} solution (0.413g of $Zn(CH_3COO)_2$ in 25 ml EtOH) before adding the hydroxide solution. Based upon green emission under UV lamp excitation, a transparent suspension of ZnO nanoparticles formed immediately after addition of the OH^- solution. When Mg^{2+} was added, a transparent suspension also showed green emission under UV lamp excitation. The remaining ions such as CH_3COO^- and Na^+ were removed from the transparent suspension of nanoparticles by repeated precipitation by heptane, centrifuging and re-dispersion in EtOH. The as-synthesized and washed suspension of nanoparticles (0.06 ~ 0.10 M) were kept at either room temperature or 0 °C for characterization. In addition, powdered nanoparticles of ZnO and ZnO:MgO (Zn:Mg solutions = 9:1) were prepared from washed suspension of nanoparticles by precipitation through addition of heptane or water, centrifuging and drying at 100 °C.

7.2.2 Characterization

Powdered nanoparticles of ZnO and ZnO:MgO were characterized by X-ray diffraction (XRD) using a Philips Model APD 3720 diffractometer with Cu Kα radiation, by Fourier Transform Infrared (FT-IR) absorption analysis using Nicolet Model 20 SXB, by Auger Electron Spectroscopy (AES) using a PHI Model 545 scanning Auger Electron Spectrometer, by X-ray Photoelectron Spectroscopy (XPS) using a Kratos Model XSAM 800 spectrometer with Mg Kα radiation, by Energy Dispersive Spectroscopy (EDS) on a JEOL Model JSM 6400 scanning electron microscope, and by High Resolution Transmission Electron Microscopy (HRTEM) using a JEOL Model 2010F transmission microscope.

Optical absorption data were collected from suspended nanoparticles of ZnO and ZnO:MgO, in polystyrene curvet using a Perkin Elmer Lambda Model 800 spectrometer. Photoluminescence (PL) emission spectra from the suspended or powdered nanoparticles were collected using either a monochromatized Xe lamp (300 W) or a HeCd laser (325 nm) for excitation. PL excitation (PLE) data were collected using the monochromatized Xe lamp.

7.3 Results and Discussion

7.3.1 Formation and Growth of Suspended Nanoparticles

A typical absorption spectrum from suspended ZnO nanoparticles is shown in Fig. 7-1. This absorption spectrum with transparency in the visible ranges suggests that the synthesized nanoparticles are well dispersed without capping agents, and that absorption by surface defect states is negligible compared to bandgap absorption. In contrast to the present data, Chen et al. [CHE97] reported that ZnS nanoparticles synthesized without capping agents showed absorption by surface defect states. An absorption spectrum from suspended ZnO:MgO nanoparticles was same as that from ZnO, except absorption edge shift to lower wavelength. The bandgap energy was dependent upon the nanoparticle size, but the values reported in the literature are dependent upon the methodology used for its determination [MEU98, MON98, WON98]. In this study, the bandgap energy was determined by converting the absorbance (A) versus wavelength of incident light to [Ln $(1\text{-}A/I_0)]^2$ (see Fig. 7-1) because this value is proportional to (hν - E_g). The bandgap energy (E_g) or corresponding wavelength (λ_g) can be calculated from extrapolating the data to intersect the energy axis, which defines E_g or λ_g [MON98]. Figure 7-2 shows bandgap energy (E_g) or corresponding wavelength (λ_g) versus aging time (t_a) of suspended nanoparticles of ZnO and ZnO:MgO. The E_g or λ_g was 3.66 eV or 337 nm 3 days after preparation, and changed to 3.51 eV or 352 nm after 24 days of aging at RT in solution. The ZnO nanoparticles bandgap was increased by quantum confinement since the corresponding E_g or λ_g of micron-sized ZnO was 3.29 eV or 375 nm. The ZnO nanoparticle size calculated from a bandgap energy of 3.66 eV from the effective mass approximation [BRU86] was ~ 4.0 nm after 3 days of aging. The radius was calculated using the following parameters: ε (dielectric constant) = 8.6, a_B (Bohr radius) = 1.25, m_e (effective mass of electron) = 0.24 and m_h (effective mass of hole) = 0.45 [MON98]. Using the same calculation and data in Fig. 7-2, the ZnO nanoparticles grew from ~ 4.0 nm at 3 day to ~ 4.5 nm at 24 day at RT. Even though data are not shown, the growth was dependent upon the aging temperature and the thoroughness of removal of residual ions such as CH_3COO^- and Na^+. The growth of suspended ZnO nanoparticles observed in this study is consistent with previous results that were explained by Ostwald ripening or growth via surface catalyzed reactions [DIJ01, HU03]

In addition to ageing of ZnO nanoparticles, similar data for ZnO:MgO nanoparticles are shown in Fig. 7-2. The E_g for ZnO:MgO nanoparticles was 0.15 ~ 0.20 eV larger (i.e., λ_g 15 ~ 20 nm smaller) as compared to suspended nanoparticles of ZnO. This difference in bandgap may result from formation of a non-equilibrium $Zn_{1-x}Mg_xO$. In study near equilibrium, a phase separation has been reported for ZnO and MgO for $x > 0.03$. For pulsed laser deposited thin films of $Zn_{1-x}Mg_xO$, values of x up to 0.37 were reported before observation of phase separation [TAK03]. The bandgap energy of $Zn_{1-x}Mg_xO$ was reported to increase from 3.3 eV to 4.3 eV for x changing from 0 to ~ 0.37. However, evidence for formation of non-equilibrium $Zn_{1-x}Mg_xO$ ($x = \sim 0.1$) by precipitation of nanoparticles from solution is lacking, as described below. Instead, the data will be interpreted based on surface segregation of Mg in ZnO.

7.3.2 Surface Segregation of Mg on ZnO Nanoparticles

As shown in Fig. 7-3, the XRD patterns from powdered nanoparticles of ZnO and ZnO:MgO were consistent with the hexagonal phase of micron-sized ZnO powders. The particle sizes calculated from Debye-Scherrer broadening for ZnO and ZnO:MgO were ~ 3.2 nm and ~ 3.0 nm, respectively, no peak shifts or peaks from other phases (e.g., Zn(OH) and $Zn(OH)_2$) were detected. In addition, the images of particles and selected area diffraction (SAD) patterns from HRTEM did not show significant difference between ZnO and ZnO:MgO nanoparticles. As shown by the HRTEM image in Fig.7-4, as-synthesized ZnO nanoparticles were typically single crystalline with well-oriented lattice planes, even though the SAD pattern shows the ring patterns of ZnO due to the overlapped nanoparticles. Note that it is difficult to determine the average particle size from the HRTEM image due to overlapping of the nanoparticles.

The FT-IR spectra (diffuse mode) of both ZnO and ZnO:MgO nanoparticles, along with the spectrum from micron-sized ZnO powders are shown in Fig. 7-5. While micron-sized ZnO has a Zn-O stretching band at 597 cm^{-1} (74 meV), ZnO and ZnO:MgO nanoparticles with size of ~ 3.2 and ~ 3.0 nm has the band shifted to 570 cm^{-1} (70 meV). The Zn-O stretching at 570 to 597 cm^{-1} corresponds to the ZnO phonon energy reported from Raman data [RAJ00, UEK03, XIN03]. In addition, the decrease of phonon energy (i.e., the decreased wave-number for the Zn-O stretching mode) for nanoparticles versus micron-sized ZnO is consistent with Raman shifts with particle size. Note that the stretching frequency for ZnO and ZnO:MgO nanoparticles are the same. If non-equilibrium $Zn_{1-x}Mg_xO$ (x = 0.1) nanoparticles had been formed, the vibration energy should have changed from that of ZnO. Therefore the XRD, SAD and IR data suggest that the different bandgap energies measured for suspended ZnO versus ZnO:MgO nanoparticles result from different particle size (i.e., the quantum effect), not from the formation of non-equilibrium $Zn_{0.9}Mg_{0.1}O$ nanoparticles.

To determine if Mg was present in nanoparticles grown from a Zn-Mg solution, EDS and AES spectra (Fig. 7-6) were collected from ZnO:MgO dried powders. The Mg/(Mg + Zn) ratio measured by EDS was ~ 0.11, consistent with the ratio of the solutions of ~ 0.10. In contrast, the Mg/(Mg + Zn) ratio determined from the AES surface analysis was ~ 0.8, much higher in Mg than either the solution or bulk ratios. The Zn_1 peak at 995 eV and Mg_2 peak at 1150 V was used to determine the surface ratio, and these Auger electrons have an attenuation depth of ~ 1 nm [FEL86]. The high Mg concentration in AES analysis must result from segregation of Mg on the surface of the ZnO:MgO nanoparticles. However, the shift from ZnO to $Zn_{1-x}Mg_xO$ (x = 0.03 for equilibrium solid solution) nanoparticles would be difficult to detect. These data are consistent with the postulate that nanoparticles produced from the reactants of Zn^{2+} and Mg^{2+} are ZnO nanoparticles cores covered with amorphous MgO shells. In fact, if the size of core the ZnO is presumed to be proportional to the Zn^{2+} concentration in the solution, the smaller size of ZnO:MgO (~3.0 nm) compared to ZnO (~ 3.2 nm) is reasonable and consistent with XRD data. These data reinforce the conclusion that the difference of bandgap energy between suspended nanoparticles of ZnO and ZnO:MgO results from the difference in particle size.

7.3.3 Effects of Mg Surface Segregation on Luminescence from Suspended ZnO Nanoparticles

7.3.3.1 Stability of green emission

The emission spectra from suspended nanoparticles of ZnO and ZnO:MgO excited by 325 nm UV from the HeCd laser are shown in Fig. 7-7 after 28 and 138 days of storage at RT. While ZnO:MgO shows only a broad green emission peak at 520 nm, ZnO shows a broad green emission peak at 550 nm with a significant UV emission peak at 350 nm. The ratio of I(UV)/I(green) from ZnO increased from 0.3 at 29 days to 9.1 at 138 days, as shown in Fig. 7-8(a). This change in ratio of emission intensity results mainly from a decrease in the green emission rather than an increase of UV emission. Over this storage time period, the suspension of ZnO nanoparticles became turbid due to aggregation of ZnO nanoparticles There was no evidence for agglomeration of the ZnO:MgO nanoparticles.

For commercial ZnO phosphors, oxygen vacancies as radiative centers are intentionally introduced by a hydrogen reduction treatment [SHI98]. In the case of solution precipitation of nanoparticles, oxygen vacancies appear to be intrinsic and may result from either non-stoichiometric precipitation or from the high surface area of nanoparticles, presuming surface defects are intrinsic and their concentration is proportional to the area. If the large surface area leads to radiative center, the amounts of these oxygen vacancies would be expected to decrease with aggregation of the nanoparticles because of reduced surface area and satisfaction of surface chemical bonds. In addition, non-radiative centers are supposed to increase with aggregation.

In contrast to the ZnO nanoparticles suspension, ZnO:MgO suspensions did not show an increase of turbidity with aging time. After 6 months of aging, the suspended nanoparticles of ZnO:MgO remained transparent. In addition, the green emission from ZnO:MgO was higher than that from ZnO, with aging time. As shown in Fig. 7-8(b), the ratio of the green emission intensities from ZnO divided by that from ZnO:MgO decreased from 0.38 at 2 days to 0.08 at 139 days. Therefore, it is obvious that surface shell of MgO prevented aggregation of the ZnO core nanopartcles and stabilized the green emission. The isoelectric points (IEP) of MgO and ZnO are about 12 and 9, respectively [REE88], therefore MgO layers should electrostatically stabilize ZnO nanoparticles in the suspension, which usually has $7 < pH < 8$.

7.3.3.2 Red shift of green emission and band filling

As shown in Fig. 7-8(c), the green emission peak from both ZnO and ZnO:MgO nanoparticles exhibited a red shift (i.e., shift to lower energy) over the first ~ 28 days of ageing. The peak wavelength of ZnO nanoparticles increased from 500 nm at 2 days to 550 nm at 28 days, then increased slowly to 560 nm at 139 days. Previously a red shift of the green ZnO emission peak with aging time was attributed to an increased particle size leading to a decreased E_g [DIJ01]. This explanation assumes that only energy of shallow defect levels will shift in parallel with shifts in the valence band edges, without shift of deep defect levels such as oxygen vacancies [DIJ00]. Even though an increase in size does occur and could partly explain the absorption and emission data in Fig. 7-2 and 7-8(c), this effect is inconsistent with the following data. First, commercial micron-size ZnO phosphor excited by 325 nm UV showed a green emission peak at 490 nm (2.52 eV) with negligible UV emission at 385 nm. Therefore, the large particle size shift from nanometers to micrometers did not cause a red shift. In addition, note that the emission from nanometer particle ZnO is already red shifted relative to the larger micrometer particle ZnO, suggesting that the levels associated with green emission may not shift in parallel with changes in the band edges. Second, the E_g measured from absorption spectra decreased less with aging than did the corresponding energy of green emission. While E_g (or λ_g) of ZnO nanoparticles decreased from 3.66 eV (337 nm at 2 days) to 3.51 eV (352 nm at 25days), the peak energy of green emission decreased from 2.47 eV (500 nm at 2 days) to 2.24 eV (550 nm at 25days). In other words, the red shift in the green emission peak was larger than that of the band gap, reinforcing the conclusion that the green emission levels are somewhat independent of the band edges of ZnO.

As an alternative to increased particle size, band filling can also explain the red shift of the green peak with aging time. Band filling has been used to explain the red shift of emissions from InP with the decrease of bias [PAN71]. In the case of InP at lower bias, the energy of the top filled state was lower than at higher bias, therefore the energy of emission was red shifted. In the case of commercial ZnO phosphors, the oxygen vacancies are distributed in the bulk over a narrow energy distribution. In contrast, radiative centers (defects), which may be oxygen vacancies or some other type of defect, are at or within a short distance of the surface. The surface proximity could change their energy, and should broaden their energy distribution [PIE87]. Based upon a broad trap energy distribution, the energy (wavelength) of the green peak from ZnO nanoparticles will decrease (increase) when the amounts of electrons recombining at non-radiative centers increase (i.e., the population of electrons trapped on radiative centers decrease), as shown schematically in Fig. 7-9. Based on this postulated mechanism, the intensity should decrease, the wavelength should increase, and the breadth should decrease for the green peak with aging. These predicted behaviors are consistent with the observations reported above, except the peak is too broad to see changes in the breadth. Changes in the intensity and wavelength do support the band filling mechanism.

From the data above, it is clear that MgO passivates the surface of ZnO nanoparticles. It is therefore reasonable to expect some effects on the states leading to PL. As shown in Fig. 7-7, the green peak wavelength at 28 days from ZnO:MgO nanoparticles is smaller (520 nm) than that from ZnO (560 nm). This is consistent with larger radiative trap filling when MgO is passivating the surface. As shown in Fig. 7-8(c), the green peak wavelength from ZnO:MgO is lower (i.e., higher energy) and less shifts less than that from ZnO (e.g., from 495 nm (2.49 eV) at 2 days to 520 nm (2.37 eV) at 139 days). The difference of peak wavelength increases from 5 nm (0.02 eV) at 2 days to 40 nm (0.17 eV) at 139 days. Again this is consistent with more filling of radiative traps when MgO is present. Finally, note that no bandedge UV emission is observed from ZnO:MgO nanoparticle, indicating that all charge carriers recombine radiatively throught the defect traps in the bandgap.

7.3.4 Emissions from Powdered ZnO Nanoparticles

7.3.4.1 Effect of Mg surface segregation on the luminescence

Figure 7-10 shows the emission and excitation spectra from nanoparticles, precipitated by heptane, of ZnO and ZnO:MgO. The intensity of the green peak from ZnO was about 5% of that from ZnO:MgO. This decrease in intensity as a result of precipitation and drying is consistent with a similar effect during aggregation of suspended ZnO, and the same explanation as above would be employed here. Similar to the observation that MgO maintained dispersion and surface area in suspensions, they should also be maintained during drying and this is reflected by a higher intensity and shorter wavelength for the green peak from ZnO:MgO. Therefore, ZnO:MgO has better luminescence properties than ZnO, regardless of whether the nanoparticles are in the powdered or suspended form.

As shown in inset of Fig. 7-10(a), while ZnO:MgO shows only a minor UV emission peak at 355 nm (3.48 eV), ZnO shows significant UV emission at 369 nm (3.34 eV). In addition, while PLE maximum for 515 nm emission from ZnO:MgO occurs at 345nm (3.58 eV), the maximum for 555 nm emission from ZnO is at 382 nm (3.23 eV) (Fig. 7-10(b)). To compare to nanoparticle PLE, commercial micron-sized ZnO phosphor shows negligible UV emission at 385 nm (3.21 eV) and a PLE maximum for 490 nm emission at 375 nm (3.29 eV), as shown in Fig. 7-11.

At room temperature, the main source of UV photons is near bandedge emission from bound excitons [HAU03, REY97, REY98], that are reported for ZnO to be 0.08 ~ 0.1 eV (~ 10 nm) below bandgap [BAG98, WAN02]. For ZnO:MgO, the relationship between UV emission (minor peak at 355 nm / 3.48 eV) and E_g (PLE peak at 345 nm / 3.58 eV) is reasonable. However, the energy of PLE peak (382 nm / 3.20 eV) for ZnO is smaller than that of UV emission (369 nm / 3.34 ev). This suggests that the 382 nm PLE peak does not correspond to excitation across the bandgap of powdered ZnO nanoparticles. Rather, the broad secondary excitation peak at ~ 360 nm (3.43 eV) could correspond to E_g of powdered ZnO nanoparticles. In the case of suspended nanoparticles, the PLE peaks for green emission are at 340 nm (3.63 eV) for ZnO:MgO and at 355 nm (3.48 eV) for ZnO, as shown in Fig. 7-12. Both excitation peaks correspond to the bandgap energy measured by absorption. The differences between the PLE peak for ZnO in suspension versus powdered must be related to differences in the electronic surface states. It is speculated that the excitation peak at 382 nm for powdered ZnO is related to new surface states, which are generated during drying and control the green emission. The data show that a MgO layer prevents the formation of these new surface states during drying, allowing bandgap absorption to be the main excitation pathway for green emission from powdered ZnO:MgO nanoparticles.

7.3.4.2 Effect of excitation energy and precipitation medium on the luminescence

As stated above, a PLE peak at 382 nm was observed from dried ZnO nanoparticles. The emission spectra with three different excitation energies are shown in Fig. 7-13 from powdered ZnO nanoparticles, which were precipitated by heptane and dried. While the emission spectra from 325 nm (3.80 eV) and 360 nm (3.43 eV) are the same, excitation at 382 nm (3.23 eV) results in another weak emission peak at 470 nm (2.63 eV).

To test the effects of the precipitation medium, water was tested since it was reported to be important in the growth of ZnO nanoparticles [MEU98]. XRD pattern from powdered ZnO nanoparticles precipitated by water and dried showed only a hexagonal ZnO phase. The XRD average size of ZnO nanoparticles produced by this procedure was large at 16.5 nm, as compared to those precipitated by heptane (3.2 nm). The formation of large sized nanoparticles results from Ostwald ripening during the precipitation by water. The PL and PLE spectra from powdered ZnO nanoparticles precipitated by water are shown in Fig. 7-14. For excitation at 325 nm (3.80 eV) (Fig. 7-14(a)), typical UV and green PL peaks were observed at 385 nm (3.21 eV) and 570 nm (2.16 eV). The UV emission at 385 nm suggests no bandgap widening at the current particle size of 16.5 nm. The PLE spectrum for 570 nm green emission (Fig 7-14(b)) shows a strong peak at 415 nm (2.97 eV), significant excitation strength at 395 nm (3.12 eV), and with bandgap excitation onset at 375 nm (3.29 eV). The excitation at 395 nm (3.12 eV) is close to the excitation band at 382 nm (3.23 eV), observed from powdered ZnO nanoparticles precipitated by heptane. In ZnO precipitated by water, 395 nm excitation produced (Fig. 7-14(c)) PL peaks at different wavelengths than for 325 nm excitation (Fig. 7-14(a)), e.g., peaks at 475 nm (2.60 eV) and 507 nm (2.43 eV) along with the typical broad green peak at 570 nm (2.16 eV). The emission band at 475 nm was already observed in the powdered ZnO nanoparticles precipitated by heptane (~ 470 nm), even though the relative intensity of each emission band was significantly different. With 415 nm (2.97 eV) excitation, a PL peak at 507 nm was observed, along with a strong emission tail ranging from 450 to 700 nm for water precipitated ZnO. Similar emission tails were also observed for 457 and 488 nm excitation from micron-sized ZnO phosphors and heptane-precipitated ZnO nanoparticles (3.2 nm). Therefore, these strong emission tail correlates with the green emission, which results from energy spread in the electronic states associated with the oxygen vacancies. Figure 7-14(e) and 7-14(f) show PLE spectra for emission at 475 nm (2.60 eV) and 507 nm (2.43 eV). The excitation spectra show excitation bands at 395 nm (3.12 eV) and 415 nm (2.97 eV). In addition, they show that excitation at 475 nm contributes to emission at 507 nm. Note that PL emission at 570, 507 and 475 nm mainly result from excitation bands at 395, 415 and 475 nm, rather than bandgap excitation that would require $\lambda < 375$ nm. The excitation and emission bands at 395, 415, 475 and 507 nm are enhanced or newly generated during the precipitation of ZnO by water followed by drying. These bands are presumed to be related to the radiative surface states on ZnO nanoparticles. Note that non-radiative surface states will also be formed along with radiative surface states, and they may significantly reduce the intensity of green emission created by bandgap excitation.

Finally, in contrast to precipitation by heptane that resulted in different luminescent properties for ZnO versus ZnO:MgO, the properties of these two luminescent types of nanoparticles were the same when water was used for the precipitation medium. For example, new excitation and emission bands at 395, 410, 475 and 500 nm were observed from powdered nanoparticles of ZnO:MgO (size = 15.0 nm), when water was used for precipitation medium. The solubility product, K_{sp}, of ZnO, $Zn(OH)_2$ and $Mg(OH)_2$ is known to be 2.2×10^{-17}, 3×10^{-16} and 6.3×10^{-10}, respectively [SKO85]. The high solubility produce for $Mg(OH)_2$ suggests that Mg compounds on the surface of ZnO nanoparticles suspended in water may be washed out during the precipitation process. Thus it is not surprising that ZnO:MgO behaves like ZnO nanoparticles when precipitated by water.

7.4 Conclusions

The properties of ZnO and ZnO:MgO nanoparticles were studied. Using a reaction between $Zn(CH_3COO)_2$, $Mg(CH_3COO)_2$ NaOH, nanoparticles ranging in size from 3 to 16 nm were produced and tested. Initially it was postulated that this process could be used to produce non-equilibrium solid solutions of $Zn_{1-x}Mg_xO$ ($x = 0.1$), however EDS and AES data demonstrated instead that Zn-rich cores with Mg-rich surface shells were precipitated. While the luminescent properties demonstrate that the core was ZnO, the Mg-rich shell is presumed to be MgO. HRTEM images and XRD patterns showed that the ZnO nanoparticles were typically single crystalline with well-oriented lattice planes and a hexagonal phase with a size of ~ 3.0 nm. FT-IR data showed that the Zn-O stretching for ZnO nanoparticles was observed at 570 cm^{-1} (70 meV), instead of 597 cm^{-1} (74 meV) observed for micron-size ZnO.

The optical absorption spectra from nanoparticles suspended in ethanol showed that quantum confinement effects led to bandgap widening of ZnO nanoparticles, with bandgap narrowing with storage times of 2 ~ 168 days at RT. In addition, the PLE and PL spectra showed stronger green emission from ZnO:MgO versus ZnO nanoparticles (suspension: 3 ~ 13 times, dried powder: 20) and stabilized emission color (small red shift from 495 nm ~ 520 nm with 168 day aging of suspended nanoparticles). The presence of MgO on the surface of ZnO nanoparticles prevented aggregation via electrostatic stabilization in the suspension. In addition, MgO appeared to prevent the formation of surface non-radiative recombination states and thereby improved the luminescent properties of ZnO.

The green emission peaks from ZnO were red shifted with respect to the commercial micron-size ZnO phosphors, and they further red shifted upon aging in solution. This red shift was discussed in terms of the filling of radiative recombination centers in the bandgap. When the nanoparticles were precipitated from solution using heptane, followed by drying and testing, the properties of ZnO:MgO remained nearly unchanged while those of ZnO were consistent with a rich spectrum of surface traps. For precipitation by water, followed by drying, the properties of ZnO:MgO and ZnO nanoparticles were similar to one another and similar to the properties of ZnO precipitated by heptane.

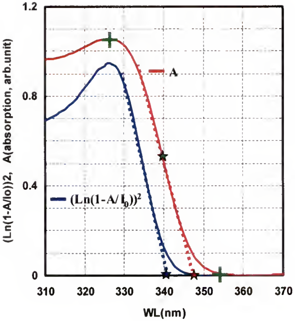

Figure 7-1. Optical absorption spectrum of ZnO nanoparticles suspended in ethanol and corresponding plot of $[\mathrm{Ln}\ (1\text{-}A/I_0)]^2$ versus wavelength. The latter plot allows determination of the optical bandgap.

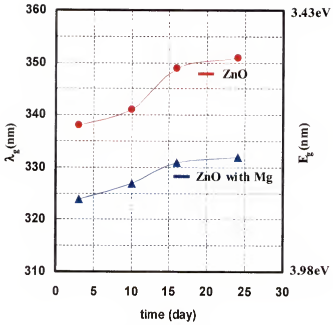

Figure 7-2. Bandgap energy (E_g) or corresponding wavelength (λ_g) versus aging time (t_a) of suspended nanoparticles of ZnO and ZnO:MgO.

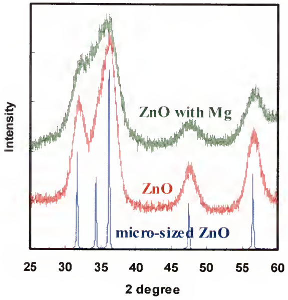

Figure 7-3. X-ray diffraction patterns from powdered (precipitated with heptane) nanoparticles of ZnO, ZnO:MgO, and micron-sized ZnO phosphors.

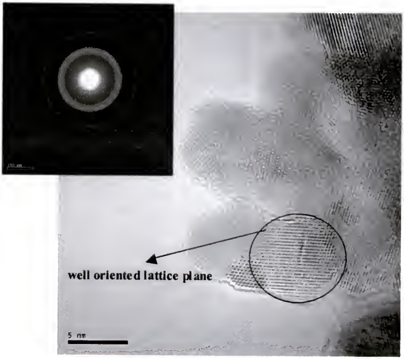

Figure 7-4. High resolution transmission electron microscope images and selected area diffraction patterns of ZnO nanoparticles.

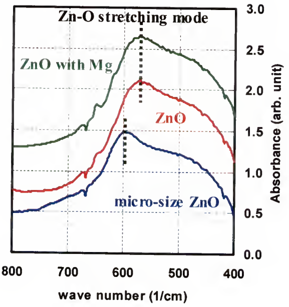

Figure 7-5. FT-IR spectra from powdered nanoparticles of ZnO and ZnO:Mg, and micron-sized ZnO phosphors.

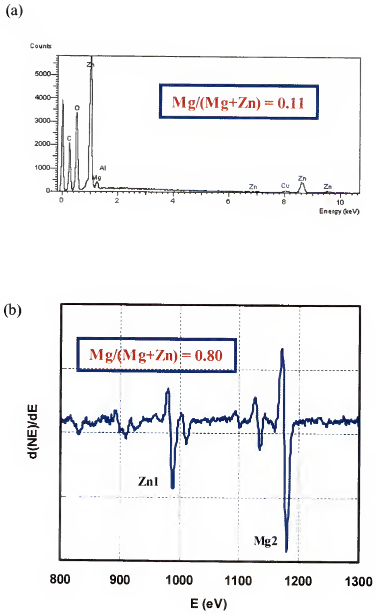

Figure 7-6. Chemical composition of ZnO:MgO. EDS spectrum (a) and AES spectrum (b) from powdered nanoparticles of ZnO:MgO.

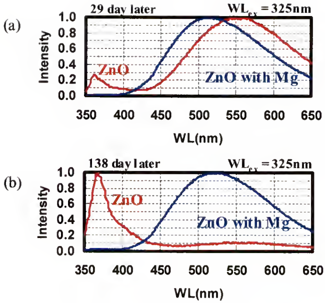

Figure 7-7. PL emission spectra from suspended nanoparticles of ZnO and ZnO:MgO, excited by 325nm UV photons from a HeCd laser. (Aging time = 29 days for (a), 138 days for (b)).

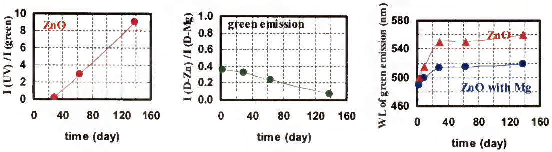

Figure 7-8. PL properties versus aging time. (a) Intensity ratio of UV to green emission (I(UV)/I(green)) from suspended ZnO nanoparticles versus aging time. (b) Intensity of green emission peak from ZnO divided by that from ZnO:MgO versus aging time. (c) Peak wavelength of green emission from suspended nanoparticles of ZnO and ZnO:MgO versus aging time.

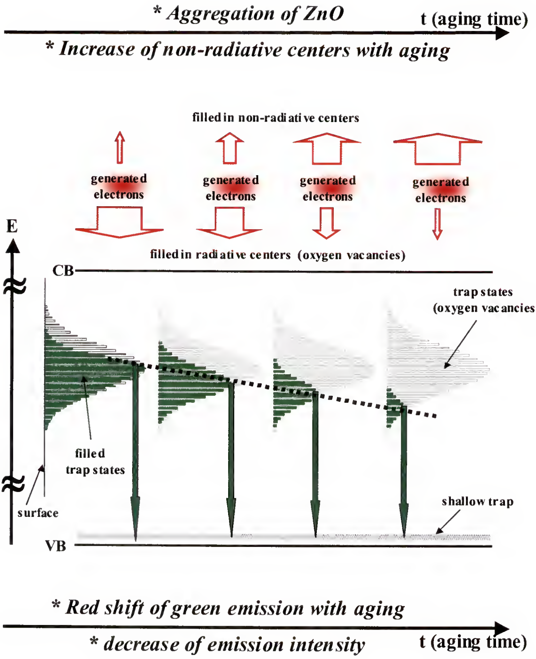
* Aggregation of ZnO
t (aging time)
* Increase of non-radiative centers with aging
filled in non-radiative centers
generated electrons
generated electrons
generated electrons
generated electrons
E
filled in radiative centers (oxygen vacancies)
CB
trap states
(oxygen vacancies)
filled
trap states
surface
shallow trap
VB
* Red shift of green emission with aging
* decrease of emission intensity
t (aging time)

Figure 7-9. Schematic diagram showing the effects of non-radiative centers and the various filling levels of radiative centers on the intensity and peak wavelength of green emission.

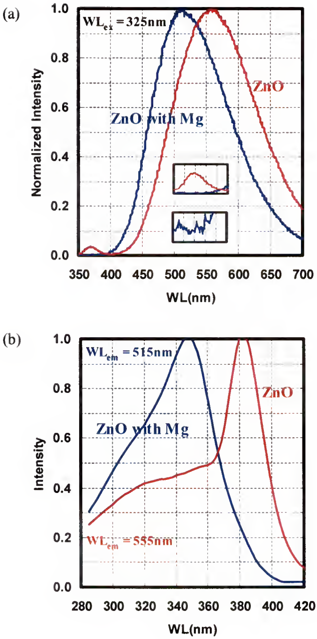

Figure 7-10. PL properties of powdered nanoparticles. PL emission (a) and PLE excitation (b) spectra from powdered nanoparticles of ZnO and ZnO:MgO precipitated using heptane.

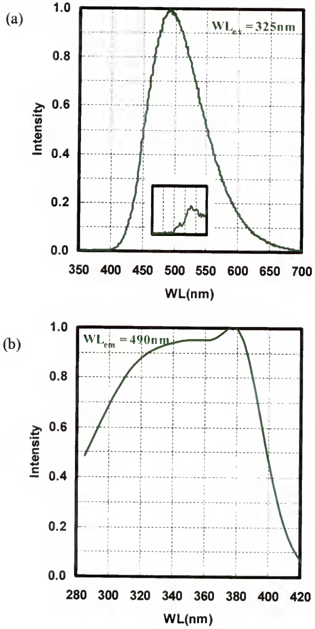

Figure 7-11. PL properties of micron-sized ZnO. PL (a) and PLE (b) spectrum from micron-sized ZnO phosphors.

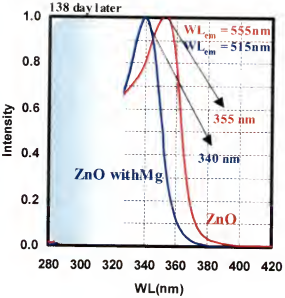

Figure 7-12. PLE spectra from suspended nanoparticles of ZnO and ZnO:MgO.

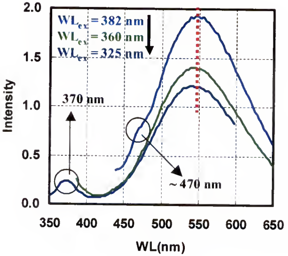

Figure 7-13. PL spectra for three different excitation energies from powdered ZnO nanoparticles that were precipitated by heptane.

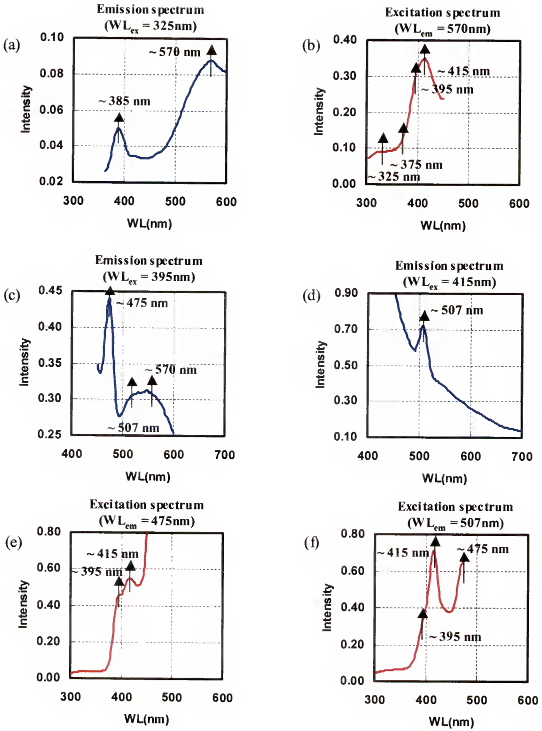

Figure 7-14. PL and PLE spectra from powdered ZnO nanoparticles that were precipitated by water. (a) PL spectrum from 325 nm excitation, (b) PLE spectrum for 570 nm emission, (c) PL spectrum from 395 nm excitation, (d) PL spectrum from 415 nm excitation, (e) PLE spectrum for 475 nm emission, and (f) PLE spectrum from 507 nm emission.

CHAPTER 8

ENHANCED LUMINESCENCE FROM SiO_2:Eu^{3+} BY EMBEDDING OF ZnO NANOPARTICLES

8.1 Introduction

The fact that a nanoparticle can transfer energy to another nanoparticle via electronic interactions (i.e., long range resonance transfer) [KAG96] suggests that this could be used to improve luminescence, especially photoluminescence, from phosphors. Luminescence from activator ions in host matrix could be increased by nanoparticle embedded into host matrix. In this approach, nanoparticles would not emit visible photons but would cause activator ions in the host matrix to emit more visible photons. In this approach, nanoparticles would be used as luminescence sensitizers.

SiO_2, Eu^{3+} and ZnO nanoparticles were chosen for the host material, activator ion in the host material, and embedded material, respectively. While the bandgap of micron-size ZnO is 3.29 eV (375 nm), that of ZnO nanoparticle increases as particle size decreases due to quantum effects. The bandgap of nanoparticle ZnO has been reported to be between 3.9 eV (316nm) and 3.4 eV (363 nm) [CHA03, MON98]. The energy absorbed above the bandgap of ZnO nanoparticles may be transferred to Eu^{3+} in SiO_2 via spectral overlap and will enhance luminescence. Since the bandgap varies with nanoparticle size, the energy transfer rate will also change with size because of changes in the spectral overlap between optical transitions from ZnO and Eu^{3+}. This suggests that the enhancement of luminescence from SiO_2:Eu^{3+} should be a function of the size of ZnO nanoparticles.

In the case of *in situ* embedding of nanoparticles in a host phosphor [FRA00, HAY00, NOG02, REI00, SEL01], it is uncertain as to whether the activator ion is doped in the nanoparticle and/or in the phosphor host matrix. As a result, it is difficult to prove that luminescence is enhanced via energy transfer from the nanoparticles. In this study, the enhanced luminescence from $SiO_2:Eu^{3+}$ will be achieved by *ex situ* embedding of ZnO nanoparticles. Energy transfer will be demonstrated based on photoluminescence excitation (PLE) spectrum.

8.2 Experimental section

8.2.1 *Ex situ* Embedding of ZnO Nanoparticles into $SiO_2:Eu^{3+}$

For the *ex situ* embedding of ZnO nanoparticles into SiO_2, suspended ZnO nanoparticles were prepared from $Zn(CH_3COO)_2$ and NaOH. For a typical preparation, 0.459g of $Zn(CH_3COO)_2$ and 0.2g of NaOH were dissolved in 30 ml and 10 ml of EtOH, respectively, with heating to 70 °C. After preparation of each solution, the OH^- solution was added into the Zn^{2+} solution in an ice bath while vigorously stirring. Based on green emission under an UV lamp, a transparent suspension of ZnO nanoparticles was formed. Remaining ions, e.g., CH_3COO^- and Na^+, were washed from the transparent suspension of nanoparticles by the repeated precipitation by adding heptane and centrifuging, followed by re-dispersion in EtOH.

Ex situ embedding was achieved by mixing of a SiO_2 sol with ZnO nanoparticles suspended in EtOH. Ethanol (4.6 g) and HNO_3 (4.5 g of 0.15 M aqueous solution) were mixed at room temperature with 10.4g of TEOS while stirring for 1 hr to produce a transparent SiO_2 sol. Equivalent amounts of the SiO_2 sol were slowly added into the suspended ZnO nanoparticles with vigorous stirring. For another *ex situ* embedding method, dilute HNO_3 was slowly added with vigorous stirring after adding equivalent amounts of TEOS into the suspended ZnO nanoparticles. In both embedding methods, the mixtures were poured into petri dish and dried in room temperature air.

For the preparation of ZnO nanoparticles embedded $SiO_2:Eu^{3+}$, $Eu(NO_3)_3$-$6H_2O$ was dissolved in EtOH then added into the TEOS in each embedding method. After gelation with controlled drying in room temperature air, the samples were dried at 150 °C or calcined at 500 ~ 700 °C . The mole % of Zn and Eu in the embedding system was from 5 to 20 % and from 1 to 5 %, respectively.

8.2.2 Characterization

ZnO embedded SiO_2 or $SiO_2:Eu^{3+}$ powders were characterized by X-ray diffraction (XRD) using a Philips Model APD 3720 diffractometer with Cu Kα radiation, by Fourier Transform Infrared (FT-IR) absorption analysis using a Nicolet Model 20 SXB, and by Auger Electron Spectroscopy (AES) using a PHI Model 545 scanning Auger Electron Spectrometer.

Optical absorption data were collected from diluted suspensions of ZnO embedded SiO_2, which were contained in polystyrene curvet, using a Perkin Elmer Lambda Model 800 spectrometer. Photoluminescence (PL) emission spectra from the ZnO embedded SiO_2 or $SiO_2:Eu^{3+}$ (suspended in EtOH or as dried powder) were collected using both a monochromatized 300 W Xe lamp and a HeCd laser (325 nm) as an excitation source. In addition, the monochromatized 300 W Xe lamp was used for PL excitation (PLE) spectra.

8.3 Results and Discussion

8.3.1 Luminescence from ZnO Nanoparticles Embedded in SiO_2

The X-ray diffraction (XRD) patterns from dried or calcined (500 ~ 700 °C) powders of ZnO embedded SiO_2 showed only an amorphous phase without any peaks from the hexagonal phase of ZnO. Due to extreme broadening of the XRD peaks by the small particle size, it is difficult to identify nanoparticles embedded in nanocomposites using XRD. ZnO nanopartcles embedded in SiO_2 were identified by FT-IR data collected in diffuse reflectance mode. As shown in the Fig. 8-1, both powdered (precipitated and dried) ZnO nanoparticles and ZnO nanoparticles embedded in SiO_2 showed a Zn-O stretching absorption band at 570 cm^{-1}, close to that from micron-size ZnO at 597 cm^{-1}. These data are strong evidence that nanoparticles were embedded as ZnO during gelation, i.e. were not simply dissolved as Zn^{2+} ions in solution in SiO_2.

As further evidence that nanoparticles were incorporated, ZnO embedded SiO_2 powders showed emission at 510 nm (Fig. 8-2), corresponding to the green emission from ZnO [LIJ00]. A bandgap absorption band for the 510 nm emission was observed at 320 nm (3.86 eV; see Fig. 8-2), higher than PLE from micron-size ZnO due to bandgap widening in the nanoparticle.

Note that just one excitation band was observed from ZnO in SiO_2, in contrast to several excitation bands observed in powdered ZnO nanoparticles (see Chapter 7 above) These differences may result from passivation of ZnO surfaces by SiO_2, similar to the effects of MgO on ZnO surfaces that were presented and discussed in Chapter 7. Data in Chapter 7 demonstrated that the agglomeration and formation of new excitation bands for ZnO nanoparticles were restricted by segregation of MgO on the surface. Similarly, SiO_2 should also retard the growth and agglomeration of ZnO nanoparticles, and restrict the formation of non-radiative centers on ZnO surfaces, as suggested by the PLE data.

The green emission peaks ($\lambda_{ex} = 325$ nm) from dilute suspension and dried powders of ZnO embedded SiO_2 were observed at 510 nm, in contrast to non-passivated ZnO nanoparticles.(~ 510 nm for suspension and ~ 550 nm for powder, refer to Chapter 7)

This invariance of emission peak after drying (or gelation of SiO_2) is consistent with surface passivation by SiO_2 that reduces the formation of surface traps.

8.3.2 Luminescence from ZnO Nanoparticles Embedded $SiO_2:Eu^{3+}$

8.3.2.1 Enhanced emissions from $SiO_2:Eu^{3+}$ by embedding of ZnO nanoparticles

Figure 8-3 shows the emission spectra from $SiO_2:Eu^{3+}$ (1 mole % of Eu^{3+}) without and with ZnO nanoparticles (10 mole % of Zn^{2+}), both of which were calcined in air at 500 °C for 2 hr. With excitation at 325 nm, both emission spectra correspond to the characteristic peaks from Eu^{3+} with emission at 612 nm being ~10 times more intense with embedded ZnO nanoparticles. Figure 8-4 shows the PLE spectra for the 612 nm emission. While $SiO_2:Eu^{3+}$ shows typical direct f-f excitation peaks including peaks at 260 nm, 325 nm, 395 nm (most intense) and 470 nm [HRE02], the ZnO embedded $SiO_2:Eu^{3+}$ shows a broad excitation band at 320 nm (3.80 eV) with small peak at 395 nm, presumably from residual excitation through the most intense Eu^{3+} f-f excitation. These excitation spectra strongly suggest that enhanced emissions from Eu^{3+} results from energy transfer from ZnO nanoparticles to Eu^{3+} activators in SiO_2 matrix. Notice that the PLE peak maximum at 320 nm for Eu^{3+} emission in Fig. 8-4 corresponds very well with that for green ZnO emission in Fig. 8-2. The PLE excitation curve for Eu^{3+} emission tails to longer wavelengths than that for ZnO green emission, however this presumably is a contribution from direct Eu^{3+} excitation as indicated by the small peak at 325 nm. The excitation and energy transfer process for ZnO nanoparticles embedded in $SiO_2:Eu^{3+}$ is illustrated schematically in Fig. 8-5.

Energy transfer rates are known to be proportional to the spectral overlap and interactions between donor and acceptor sites or species [BLA94]. Energy transfer rates are larger for band to band processes due to the larger spectral overlap. In addition, the strength of interaction is determined by the intensity of an optical transition, and this is larger for allowed (i.e., broad band) compared to forbidden (i.e., narrow line) transitions [BLA94]. Energy transfer from ZnO nanoparticles embedded in $SiO_2:Eu^{3+}$ occurs from a 'allowed' broad band emitting donor (ZnO) to a 'forbidden' line absorbing acceptor (Eu^{3+}), and high rates were expected. Even though band-to-line energy transfer is less efficient than a band-to-band transfer, it has been used for commercial phosphors. The luminescence from Tb^{3+} (f-f line transition) is enhanced by co-doping with Ce^{3+} (f-d band transition) [SHI98].

Notice in Fig. 8-4 that $SiO_2:Eu^{3+}$ cannot be excited by 350 nm (3.53 eV) photon, while strong 612 nm emission is observed when ZnO nanoparticles are present. By the principles of energy transfer, re-emission of a 350 nm photon from ZnO cannot cause direct emission from a Eu^{3+} absorber due to lack of spectral overlap. These data strongly suggest that energy absorbed by ZnO nanoparticles is also transferred to Eu^{3+} by phonon-mediated processes, leading to emission when there is no spectral overlap. Note also that the energy transfer process from ZnO to Eu^{3+} is very efficient based on the fact that only Eu^{3+} emission is observed. Emission from ZnO is completely quenched.

8.3.2.2 Effect of Eu^{3+} and ZnO concentration on PL enhancement

The 612 nm emission intensities from $SiO_2:Eu^{3+}$ (5 mole % of Eu^{3+}) versus amounts of embedded ZnO nanoparticles is shown in Fig. 8-6. Embedded ZnO nanoparticle enhanced the luminescence from Eu^{+3}, whether calcined (600 °C) or not (dried, 150 °C). For calcined samples, the 612 nm intensities increased with amounts of embedded ZnO nanoparticles up to ~ 10 mole %, then remained nearly unchanged at larger concentrations. The ratio of intensity with and without ZnO nanoparticles is nearly constant at ~ 5.5 for $x > 10$ mole %. As shown in Fig. 8-3, the intensity from SiO_2 with 1 mole % of Eu^{3+} and 10 mole % of ZnO is ~ 10 times larger than for no ZnO, compared to ~ 5.5 times for 5 mole % Eu^{3+}. These data show that the enhancement by energy transfer from ZnO nanoparticles to Eu^{3+} depends on the amounts of both embedded ZnO and Eu^{3+}.

Energy transfer from ZnO to Eu^{3+} will dominate over emission from ZnO when R (the distance between a donor ZnO nanoparticle and an acceptor Eu^{3+}) < R_c (the critical distance at which ZnO emission dominates over energy transfer). Even though the critical distance, R_c, cannot be calculated, data in Fig. 8-3, 8-4 and 8-6 suggest that 5 ~ 20 mole % of ZnO nanoparticle embedded in SiO_2 with 1 ~ 5 mole % of Eu^{3+} has sufficiently small distance for energy transfer to occur. R will decrease with an increase of embedded ZnO and/or Eu^{3+}. However, concentration quenching by energy transfer between Eu^{3+} (i.e., interaction quenching) must also be a factor limiting increased luminescence from Eu^{3+}, even with energy transfer (i.e., sensitizing) from ZnO nanoparticles. Concentration quenching of Eu^{3+} is well known and dependent on host materials [SHI98]. Presumably, the decreased enhancement for 5 versus 1 mole % of Eu^{3+} (~ 5.5 versus ~ 10 with 325 nm excitation and 10 mole % ZnO) results from concentration quenching.

For a fixed Eu^{3+} concentration, an increase of embedded ZnO will result in a decreased R and an increased enhancement, as shown in the Fig. 8-6. However, energy back-transfer from Eu^{3+} to ZnO and possible energy dissipation by non-radiative centers will also increase with an increased ZnO nanoparticle concentration. Based upon such a process, energy transfer from ZnO to Eu^{3+} would be expected to increase, then remain constant for larger concentrations of ZnO, as shown in Fig. 8-6.

The optical transitions involved in energy transfer between ZnO nanoparticles and Eu^{3+} ions are ill defined. The excitation spectra in the Fig. 8-4 demonstrate the existence of energy transfer between ZnO nanoparticles and Eu^{3+}, and explain the enhanced luminescence from Eu^{3+}. Two possible energy transfer mechanisms leading to enhanced luminescence are suggested in Fig. 8-7. In the first, energy at or above bandgap is absorbed by ZnO and transferred to Eu^{3+} states higher in energy than the radiative ^5D_j state (Fig. 8-7) via UV bandedge emissions from ZnO. The excited state is relaxed to the ^5D_j states and enhanced luminescence is observed. In the second, defect states in the bandgap of ZnO (with a broad energy distribution) are filled by bandgap absorption from ZnO and transfer energy resonantly (or by phonon mediated processes) to the ^5D_j states via green emissions from ZnO, again resulting in enhanced luminescence.

8.4 Conclusions

ZnO nanoparticles embedded into SiO_2 by an ex-situ method were shown to result in stabilized green emission with a peak at ~ 510 nm compared to the normal peak at 495 nm from micron-sized ZnO powders. The green emission from ZnO nanoparticles was completely suppressed when embedded in SiO_2 doped with Eu^{3+}. Instead, the f-f emissions from Eu^{3+} were enhanced by 5 ~ 10 times by energy transfer from the embedded ZnO nanoparticles to Eu^{3+}. The increase in the Eu^{+3} luminescence was shown to be larger for 1 vs. 5 mole % Eu^{3+}, and to increase up to 10 mole % of embedded ZnO nanoparticles. The roles in this luminescence of phonon mediated energy transfer, quenching by activator interactions between Eu^{3+} ions, and energy back-transfer from Eu^{3+} ions to ZnO nanoparticles were discussed.

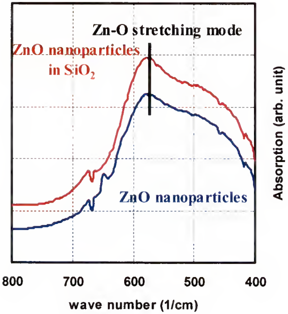

Figure 8-1. FT-IR spectra from ZnO nanoparticle powders and from ZnO embedded in SiO_2 (Zn:Si = 1:9). The coincidence between the Zn-O stretching frequency demonstates that ZnO embedded in SiO_2 as nanoparticles.

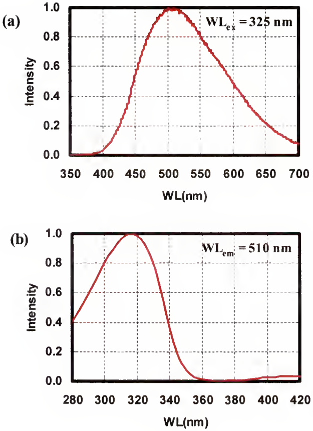

Figure 8-2. PL properties of embedded ZnO. PL emission (a) and excitation (b) spectrum from ZnO nanoparticles embedded SiO_2

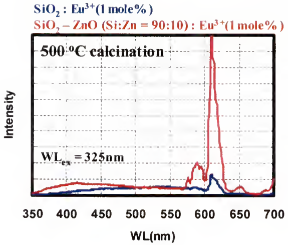

Figure 8-3. PL emission spectra from $SiO_2:Eu^{3+}$ and ZnO nanoparticle embedded $SiO_2:Eu^{3+}$ after calcining at 500 °C. (λ_{ex} = 325 nm) Note the lack of green emission from ZnO.

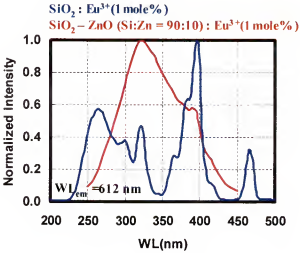

Figure 8-4. PL excitation spectra from $SiO_2:Eu^{3+}$ and ZnO nanoparticle embedded $SiO_2:Eu^{3+}$ after calcining at 500°C. (λ_{em} = 612 nm)

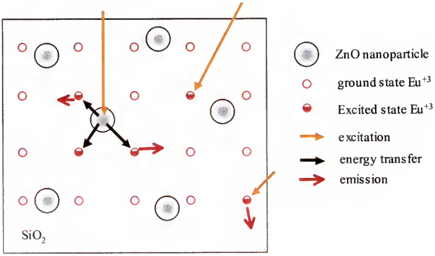

Figure 8-5. Schematic diagram of ZnO nanoparticles embedded in SiO$_2$:Eu^{+3}

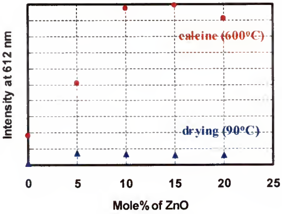

Figure 8-6. Emission intensities (at 612 nm) from SiO$_2$:Eu^{+3} (5 mole %) versus concentration of embedded ZnO nanoparticles.

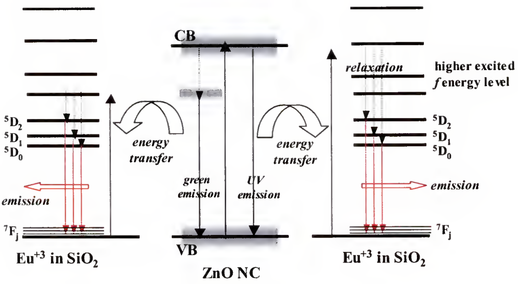

Figure 8-7. Possible luminescent mechanisms for ZnO nanoparticle embedded SiO_2: Eu^{+3}

CHAPTER 9
CONCLUSIONS AND FUTURE WORK

9.1 Conclusions

9.1.1 Combustion Synthesis of Eu^{3+}, Tb^{3+} and Tm^{3+} Doped Ln_2O_2S (Ln = Y, La, Gd) Phosphors

Powder phosphors of $(Y_{1-x}RE_x)_2O_2S$, $(La_{1-x}RE_x)_2O_2S$, and $(Gd_{1-x}RE_x)_2O_2S$ where RE = Eu^{3+}, Tb^{3+}, or Tm^{3+} were prepared by combustion reactions from mixed metal nitrate reactants and dithiooxamide ($(CSNH_2)_2$) with ignition temperatures of 300 ~ 350 °C. The X-ray diffraction patterns of as-synthesized powders revealed that the Ln_2O_2S (Ln = Y, La, and Gd) phase crystallized directly from the combustion reaction with fuel to oxidizer ratios of ~ 2.0. Powders synthesized with a lower F/O ratio, especially for yttrium phosphors, were contaminated by residual carbonaceous material. Increased water during combustion was shown to favor formation of oxides or sulfates over oxysulfides. Scanning electron microscope images of as-synthesized powders showed a foamy, porous agglomeration and a continuous three-dimensional network. The agglomerates ranged in size between 10 μm and 30 μm, while the primary particles ranged in size between 100 nm and 200 nm. The phosphors prepared by combustion reaction were cathodoluminescent and photoluminescent immediately after combustion without additional heating. They exhibited the characteristic emission spectrum of Eu^{3+}, Tb^{3+}, or Tm^{3+}. The cathodoluminescent efficiency of as-synthesized, non-optimized $Gd_2O_2S:Tb^{3+}$ (1.0 mole %) phosphors was lower than that of commercial phosphors at all electron beam energies (30 to 15 % at 1 to 4 kV). While grinding and heat treatment (900 °C, Ar, 60 min) decreased and increased the PL intensity, respectively, the CL intensity was not changed by these treatments. Possible reasons for these observations were discussed.

9.1.2 Temporal Cathodoluminescence Quenching from Eu^{3+} Doped La_2O_2S

Quenching of the cathodoluminescent (CL) efficiency of $La_2O_2S:Eu^{3+}$ prepared by combustion reaction was investigated by measuring the temporal dependence of the CL intensities. While the emission intensity corresponding to the $^5D_0 \Rightarrow ^7F_2$ electronic transition of Eu^{3+} did not change at a low current density (e.g. 65 μA/cm^2), it decayed over the first ~ 5 sec. of irradiation at a high current density (e.g. 500 μA/cm^2). Also, the difference between the initial and steady state emission intensities increased as the current density increased. Based on thermal quenching data for the $^5D_0 \Rightarrow ^7F_2$ transition, the quenching observed at high current densities was only partially explained by electron beam heating. In addition to changes in intensity, the ratio of the CL intensities from the $^5D_1$ transition ($^5D_1 \Rightarrow ^7F_3$) and the $^5D_0$ transition ($^5D_0 \Rightarrow ^7F_2$) (designated $^5D_1/^5D_0$) also decreased with increasing current density during the first ~ 5 sec of electron irradiation. Based upon measurement of the Auger electron peak energies, it is suggested that surface voltage changes due to charging cannot explain these changes. Instead, it was postulated that local redistribution of charge carriers over the range of the primary electron beam resulted from induced internal electron field and enhanced activator interactions, specifically at higher excitation densities (e.g., at high primary beam energy and high current densities). Further, it was speculated that different effects of the induced internal electric field on the activator interaction for different excited ^5D_j state of the Eu^{3+} also changed the $^5D_1/^5D_0$ ratio. These mechanisms were used to explain the difference between PL and CL results. The effects of current density, beam energy and Eu^{3+}

activator concentration on CL quenching were classified into three regions dependent upon whether first or second order activation interactions were dominant in the radiative relaxation process.

9.1.3 Effects of Energy Feeding and Funneling on Peak Height Ratios $^5D_J/^5D_0$ from Cathodoluminescence of Ln_2O_2S: Eu^{3+} (Ln = La, Gd)

The effects of current densities and temperature on the temporal quenching of the $^5D_2{=}{>}^7F_3$, $^5D_1{=}{>}^7F_3$ and $^5D_0{=}{>}^7F_2$ cathodoluminescent transitions from Eu^{3+} were studied for $Ln_2O_2S{:}Eu^{3+}$ (Ln = La, Gd) phosphors. The decrease of the emission intensities with time, i.e. temporal quenching, was characterized by the initial (t = 0) and the steady state (t = ~5-15 secs) intensity ratios of these transitions, designated as $^5D_2/^5D_0$ and $^5D_1/^5D_0$. The intensity ratio, $^5D_1/^5D_0$, increased then decreased for both $La_2O_2S{:}Eu^{3+}$ (0.1 mole %) and $Gd_2O_2S{:}Eu^{3+}$ (0.4 mole %), as the current density was changed from 10 towards a 1000 $\mu A/cm^2$. Specifically, for $Gd_2O_2S{:}Eu^{3+}$ (0.4 mole %), the steady state $^5D_1/^5D_0$ ratios increased (from 0.26 to 0.38) at lower current densities (from 14 to 386 $\mu A/cm^2$) and decreased (from 0.38 to 0.34) at higher current densities (from 386 to 772 $\mu A/cm^2$). These data were explained by postulating that energy feeding from the higher $^5D_2$ excited state to the lower energy $^5D_1$ excited state was dominant at lower current densities, resulting in an increase of the $^5D_1/^5D_0$ ratio. At higher current densities, energy funneling from the $^5D_1$ to $^5D_0$ states was dominant, resulting in a decrease of the $^5D_1/^5D_0$ ratio. Consistent with this interpretation, the steady state $^5D_2/^5D_0$ ratios decreased (from 0.08 to 0.03) at lower current densities (from 14 to 386 $\mu A/cm^2$), consistent with feeding from the higher $^5D_2$ to the lower excited state $^5D_1$ resulting in the decrease of $^5D_2/^5D_0$, along with the increase of $^5D_1/^5D_0$. These effects of feeding versus funneling were dependent on both the Eu^{3+} concentration and current density, and changed with times (i.e., approached a steady state after ~5 sec) due to increased activator interactions from induced internal electric fields. The magnitudes of quenching due to thermal versus activator interactions were investigated using changes of the peak height ratios of $^5D_2/^5D_0$ and $^5D_1/^5D_0$ from $Gd_2O_2S:Eu^{3+}$ (0.4 mole %). The different behavior of the $^5D_1/^5D_0$ versus $^5D_2/^5D_0$ peak height ratios with an increase of temperature and current densities results from the different mechanisms for thermal and interaction quenching. The different convergent values of $^5D_1/^5D_0$ ratio from $La_2O_2S:Eu^{3+}$ (0.5 mole %) phosphors versus temperature and current densities (~ 0.1 at high temperatures and ~ 0.3 at high current densities) results from these different quenching mechanisms, suggesting that temporal CL quenching does not result from heating by the electron beam.

9.1.4 Effects of Coatings on Temporal Cathodoluminescence Quenching in ZnS:Ag,Cl Phosphors

Powder phosphors of ZnS:Ag,Cl coated with SiO_2 (22 or 130 nm nanoparticles), SnO_2 or Al_2O_3 showed different cathodoluminescent (CL) brightness versus time (temporal CL quenching) behavior as compared to non-coated phosphors. At high current density (e.g., 600 $\mu A/cm^2$, 2 kV), while non-coated ZnS powder phosphors did not show temporal CL quenching, the CL emission intensity of coated ZnS:Ag,Cl powder phosphors decayed by factors ranging from 70 % to 90 % (i.e., temporal quenching factors ranging from 0.3 to 0.1) over the first ~ 15 seconds of electron beam irradiation. This temporal CL quenching was shown to be consistent with an increase in the concentration of non-radiative surface centers generated during surface modification of the phosphor. During the first ~ 15 sec of excitation, generated electrons are postulated to be localized at the surface by primary beam-induced internal electric fields, resulting in a decrease of emission intensity due to the increased non-radiative surface recombination between electrons and holes. Based on temporal quenching even in the absence of an energy shift for Auger electrons, it was suggested that development of a surface potential on the phosphor did not result in significant temporal quenching. The formation of a non-radiative surface layer either from electron-stimulated surface chemical reactions on coated or from heat treatment of non-coated ZnS:Ag,Cl powder phosphors was shown to affect temporal CL quenching.

9.1.5 Enhanced Green Emission from ZnO Nanoparticles by Surface Segregation of Mg

Using a reaction between Zn^{2+}, Mg^{2+} and OH^- containing EtOH solutions, ZnO and ZnO:MgO nanoparticles ranging in size from 3 to 16 nm were produced. Initially it was postulated that this process could be used to produce non-equilibrium solid solutions of $Zn_{1-x}Mg_xO$ ($x = 0.1$), however EDS and AES data demonstrated instead that ZnO nanoparticles with surface segregation of Mg (ZnO:MgO) were precipitated. HRTEM images and XRD patterns showed that the ZnO nanoparticles were typically single crystalline with well-oriented lattice planes and a hexagonal phase with a size of ~ 3.0 nm. FT-IR data showed the Zn-O stretching band at 570 cm^{-1} (70 meV) for ZnO nanoparticles, instead of 597 cm^{-1} (74 meV) for micron-size ZnO. The optical absorption spectra from suspended nanoparticles showed bandgap widening of ZnO nanoparticles, with bandgap narrowing with aging of 2-140 days. In addition, the PLE and PL spectra showed that surface segregation of Mg on ZnO nanoparticles led to stronger green emission (3 ~ 13 times for suspension and 20 times for dried powder) and stabilized emission color (small red shift from 495 nm to 520 nm with aging of 140 days). The presence of MgO on the surface of ZnO nanoparticles appeared to prevent aggregation via electrostatic stabilization in the suspension, and also prevented the formation of surface non-radiative recombination states. The green emission peak from ZnO nanoparticles was red shifted with respect to the commercial micron-size ZnO phosphors, and they further red shifted upon aging in solution. This red shift was discussed in terms of the filling of radiative centers (i.e., oxygen vacancies) distributed over an energy band in the bandgap. When heptane was used for precipitation of nanoparticles from suspension, the luminescent properties of dried ZnO:MgO powder remained nearly unchanged, while those of ZnO were consistent with a spectrum of non-radiative centers, some newly formed during drying. In addition, PLE and PL spectra showed that the emission and excitation due to new radiative centers were stronger in ZnO precipitated by water, as compared to ZnO precipitated by heptane, and that the luminescent properties of ZnO and ZnO:MgO nanoparticles precipitated by water were similar to one another.

9.1.6 Enhanced Luminescence from SiO_2:Eu^{3+} by Embedding of ZnO Nanoparticles

ZnO nanoparticles embedded into SiO_2 by an *ex-situ* method were shown to result in stabilized green emission with a peak at ~ 510 nm compared to the normal peak at 495 nm from micron-sized ZnO powders. The green emission from ZnO nanoparticles was completely suppressed when embedded in SiO_2 doped with Eu^{3+}. Instead, the f-f emissions from Eu^{3+} were enhanced by 5 ~ 10 times by energy transfer from the embedded ZnO nanoparticles to Eu^{3+}. The increase in the Eu^{3+} luminescence was shown to be larger for 1 vs. 5 mole % Eu^{3+}, and to increase up to 10 mole % of embedded ZnO nanoparticles. The roles in this luminescence of phonon mediated energy transfer, quenching by activator interactions between Eu^{3+} ions, and energy back-transfer from Eu^{3+} ions to ZnO nanoparticles were discussed.

9.2 Future Work

Optimization of combustion synthesized Ln_2O_2S (Ln = Y, La, Gd) phosphors and a more detailed study of temporal CL quenching from thin film phosphors versus current density are needed. In addition, temporal CL quenching from various powder phosphors should be studied in order to correlate temporal CL quenching with the properties of host materials and luminescence mechanisms (i.e., luminescence via donor-acceptor recombination and iso-electronic transition).

The mechanism for surface segregation of Mg on ZnO nanoparticles, synthesis of nanoparticles with similar compositions (e.g., ZnO:CaO) and analysis of surface Mg layer should be studied. In addition, the optimization of *ex-situ* embedding with homogeneous dispersion of ZnO nanoparticles, and measurements of CL properties from ZnO embedded $SiO_2:Eu^{3+}$ should be continued in the future.

LIST OF REFERENCES

[ABD92] A. Abdelkader and M. M. Elkholy, Journal of Materials Science 27, 2887 (1992).

[ABE01] K. Abe, Y. Sanada, and T. Morimoto, Journal of Sol-Gel Science and Technology 22, 151 (2001).

[ABR00] B. L. Abrams, W. Roos, P. H. Holloway, and H. C. Swart, Surface Science 451, 174 (2000).

[ABR01] B. L. Abrams, Ph.D. Dissertation, University of Florida, 2001.

[ALI77] R. C. Alig and S. Bloom, Journal of the Electrochemical Society 124, 1136 (1977).

[BAC00] C. F. Bacalski, M. A. Cherry, G. A. Hirata, J. M. Mckittrick, and J. Mourant, Journal of the SID Suppl.1, 93 (2000).

[BAG98] D. M. Bagnall, Y. F. Chen, M. Y. Shen, Z. Zhu, T. Goto, and T. Yao, Journal of Crystal Growth 185, 605 (1998).

[BAN03] J. Bang, A. Mostafa, B. Abrams, and P. Holloway, Journal of Applied Physiscs 94, 7091 (2003).

[BAN04] J. Bang, A. Mostafa, B. Abrams, and P. Holloway, Journal of Luminescence 106, 177 (2004).

[BHA94] R. N. Bhargava, D. Gallagher, X. Hong, and A. Nurmikko, Physical Review Letters 72, 416 (1994).

[BLA94] G. Blasse and B. C. Grabmaier, Luminescent Materials (Springer-Verlag, Heidelberg, 1994).

[BOL00] A. A. Bol and A. Meijerink, Journal of Luminescence 87-89, 315 (2000).

[BOS02] E. J. Bosze, G. A. Hirata, and J. Mckittrick, 2002 International conference on the science and technology of emissive displays and lighting, 395 (2002).

[BRO01] F. Brotman, Information Display 17, 32 (2001).

[BRU86] L. Brus, Journal of Physical Chemistry 90, 2555 (1986).

[BUK01] S. A. Bukesov, Proceedings of the SPIE - The International Society for Optical Engineering 4511, 43 (2001).

[BUK02] S. A. Bukesov and D. Y. Jeon, Applied Physics Letters 81, 2184 (2002).

[CAZ91] J. Cazaux, K. H. Kim, O. Jbara, and G. Salace, Journal of Applied Physics 70, 960 (1991).

[CHA97] A. G. Chakhovskoi, C. E. Hunt, M. E. Malinowski, T. E. Felter, and A. A. Talin, Journal of Vacuum Science & Technology B 15, 507 (1997).

[CHA03] S. Chakrabarti, D. Ganguli, and S. Chaudhuri, Journal of Physics D-Applied Physics 36, 146 (2003).

[CHE97] W. Chen, Z. G. Wang, Z. J. Lin, and L. Y. Lin, Journal of Applied Physics 82, 3111 (1997).

[CHO98] K. G. Cho, D. Kumar, D. G. Lee, P. H. Holloway, and R. K. Singh, Flat-Panel Display Materials - 1998. Symposium, 301 (1998).

[CHO99] K. G. Cho, D. Kumar, Z. Chen, P. H. Holloway, and R. K. Singh, Luminescent Materials. Symposium, 83 (1999).

[CHO01] J. Y. Choe, D. Ravichandran, S. M. Blomquist, D. C. Morton, K. W. Kirchner, M. H. Ervin, and U. Lee, Applied Physics Letters 78, 3800 (2001).

[CHU95] J. Chunming, Y. Jiaqi, S. Lingdong, D. Kai, H. Shanggong, Z. Jialong, C. Yimin, and H. Shihua, Journal of Luminescence 66-67, 315 (1995).

[CRO02] S. A. Crooker, J. A. Hollingsworth, S. Tretiak, and V. I. Klimov, Physical Review Letters 89 (2002).

[DEX53] D. L. Dexter, Journal of Chemical Physics 21, 836 (1953).

[DEX54] D. L. Dexter, Journal of Chemical Physics 22, 1063 (1954).

[DIJ00] A. V. Dijken, E. A. Meulenkamp, D. Vanmaekelbergh, and A. Meijerink, Journal of Luminescence 90, 123 (2000).

[DIJ01] A. V. Dijken, J. Makkinje, and A. Meijerink, Journal of Luminescence 92, 323 (2001).

[DIN99] A. D. Dinsmore, D. S. Hsu, H. F. Gray, S. B. Qadri, Y. Tian, and B. R. Ratna, Applied Physics Letters 75, 802 (1999).

[EFR96] A. L. Efros, M. Rosen, M. Kuno, M. Nirmal, D. J. Norris, and M. Bawendi, Physical Review B 54, 4843 (1996).

[FEL86] L. C. Feldman and J. W. Mayer, Fundamentals of surface and thinfilm analysis (North-Holland, Amsterdam, 1986).

[FEL00] C. Feldmann and J. Merikhi, Journal of Colloid and Interface Science 223, 229 (2000).

[FIT98] J. M. Fitzgerald, T. A. Trottier, R. K. Singh, and P. H. Holloway, Applied Physics Letters 72, 1838 (1998).

[FON66] W. H. Fonger and C. W. Struck, Journal of Chemical Physics 52, 6364 (1966).

[FON70] W. H. Fonger and C. W. Struck, Journal of Chemical Physics 52, 6364 (1970).

[FOR48] V. T. Forster, Annalen der Physik 2, 55 (1948).

[FRA00] G. Franzo, D. Pacifici, V. Vinciguerra, F. Priolo, and F. Iacona, Applied Physics Letters 76, 2167 (2000).

[GES68] G. H. Gessinger, F. V. Lenel, and G. S. Ansell, Journal of Applied Physics 39, 5593 (1968).

[GIB99] C. S. Gibbons, D. M. Nicholas, D. Morton, A. Vecht, and D. W. Smith, Society for Information Display 1999 International Symposium, 1030 (1999).

[GOR97] S. Gorer, G. Hodes, Y. Sorek, and R. Reisfeld, Materials Letters 31, 209 (1997).

[GRE02] A. P. Greeff and H. C. Swart, Thin Solid Films 408, 260 (2002).

[GRO87] B. Gross, H. von Seggern, and A. Berraissoul, IEEE Transactions on Electrical Insulation EI-22, 23 (1987).

[GUO00] L. Guo, S. H. Yang, C. L. Yang, P. Yu, J. N. Wang, W. K. Ge, and G. K. L. Wong, Applied Physics Letters 76, 2901 (2000).

[HAC02] M. Hack and J. J. Brown, Information Display 18, 16 (2002).

[HAU03] M. Haupt, A. Ladenburger, R. Sauer, K. Thonke, R. Glass, W. Roos, J. P. Spatz, H. Rauscher, S. Riethmuller, and M. Moller, Journal of Applied Physics 93, 6252 (2003).

[HAY00] T. Hayakawa, S. T. Selvan, and M. Nogami, Journal of Sol-Gel Science and Technology 19, 779 (2000).

[HAY68] J. W. Haynes and J. J. Brown, Journal of the Electrochemical Society 115, 1060 (1968).

[HEI98] J. R. Heine, J. Rodriguez-Viejo, M. G. Bawendi, and K. F. Jensen, Journal of Crystal Growth 195, 564 (1998).

[HOL99] P. H. Holloway, T. A. Trottier, B. Abrams, C. Kondoleon, S. L. Jones, J. S. Sebastian, W. J. Thomes, and H. Swart, Journal of Vacuum Science & Technology B (Microelectronics and Nanometer Structures) 17, 758 (1999).

[HOL00a] P. H. Holloway, T. A. Trottier, J. Sebastian, S. Jones, X.-M. Zhang, J.-S. Bang, B. Abrams, W. J. Thomas, and T.-J. Kim, Journal of Applied Physics 88, 483 (2000).

[HOL00b] P. H. Holloway, W. J. Thomes, B. Abrams, S. Jones, and L. Williams, IDW '00. Proceedings of the Seventh International Display Workshops, 837 (2000).

[HON94] C. S. Hong, P. Ravindranathan, D. K. Agrawal, and R. Roy, Journal of Materials Research 9, 2398 (1994).

[HOP00] G. Hopple and C. Curtin, Information Display 16, 34 (2000).

[HRE02] D. Hreniak, M. Jasiorski, K. Maruszewski, L. Kepinski, L. Krajczyk, J. Misiewicz, and W. Strek, Journal of Non-Crystalline Solids 298, 146 (2002).

[Hu03] Z. S. Hu, G. Oskam, and P. C. Searson, Journal of Colloid and Interface Science 263, 454 (2003).

[IGA01] T. Igarashi, T. Kusunoki, K. Ohno, T. Isobe, and M. Senna, Materials Research Bulletin 36, 1317 (2001).

[IGA02] T. Igarashi, T. Kusunoki, K. Ohno, T. Isobe, and M. Senna, Materials Research Bulletin 37, 533 (2002).

[IHA02] M. Ihara, T. Igarashi, T. Kusunoki, and K. Ohno, Journal of the Electrochemical Society 149, H72 (2002).

[IMA80] S. Imanaga, S. Yokono, and T. Hoshina, Japanese Journal of Applied Physics 19, 41 (1980).

[INO65] M. Inokuti and F. Hirayama, Journal of Chemical Physics 43, 1978 (1965).

[ITO00] S. Itoh, H. Toki, F. Kataoka, Y. Sato, and K. Tamura, Journal of the SID suppl.1, 187 (2000).

[JON99] S. L. Jones, D. Kumar, K.-G. Cho, R. Singh, and P. H. Holloway, Displays 19, 151 (1999).

[JUS98] T. Justel, H. Nikol, and C. Ronda, Angewandte Chemie-International Edition 37, 3085 (1998).

[KAG96] C. R. Kagan, C. B. Murray, and M. G. Bawendi, Physical Review B 54, 8633 (1996).

[KAJ03] K. Kajiwara, Journal of Vacuum Science and Technology B 21, 1622 (2003).

[KAN99] Y. C. Kang, S. B. Park, I. W. Lenggoro, and K. Okuyama, Journal of Physics and Chemistry of Solids 60, 379 (1999).

[KIM01] G. C. Kim, H. L. Park, and T. W. Kim, Materials Research Bulletin 36, 1603 (2001).

[KOM97] H. Kominami, Y. Nakanishi, Y. Hatanaka, G. Shimaoka, T. Nakamura, and K. Sowa, Applied Surface Science 113-114, 519 (1997).

[KOM98] K. Kominami, K. Horikawa, T. Aoki, T. Nakamura, Y. Nakanishi, and Y. Hatanaka, The 4th international conference on the science and technology of display phosphors, 381 (1998).

[KOT96] M. Kottaisamy, D. Jeyakumar, R. Jagannathan, and M. Mohan Rao, Materials Research Bulletin 31, 1013 (1996).

[KUB80] S. Kuboniwa, H. Kawai, and T. Hoshina, Japanese Journal of Applied Physics 19, 1647 (1980).

[LEE98] R. Y. Lee, F. L. Zhang, J. Penczek, B. K. Wagner, P. N. Yocom, and C. J. Summers, Journal of Vacuum Science & Technology B (Microelectronics and Nanometer Structures) 16, 855 (1998).

[LEE01] R. Y. Lee and S. W. Kim, Journal of Luminescence 93, 93 (2001).

[LEE83] D. M. Leeuw and G. W. Hooft, Journal of Luminescence 28, 275 (1983).

[LOO01] D. C. Look, Materials Science and Engineering B-Solid State Materials For Advanced Technology 80, 383 (2001).

[LOP97] O. A. Lopez, J. McKittrick, and L. E. Shea, Journal of Luminescence 71, 1 (1997).

[MA97] D. Ma, X. Liu, Y. Pei, and L. Cao, SID 97 Digest, 423 (1997).

[MAH99] S. Mahamuni, K. Borgohain, B. S. Bendre, V. J. Leppert, and S. H. Risbud, Journal of Applied Physics 85, 2861 (1999).

[MAP73] T. G. Maple and R. A. Buchanan, Journal of Vacuum Science and Technology 10, 616 (1973).

[MAT99] Y. Matsumoto, M. Murakami, Z. W. Jin, A. Ohtomo, M. Lippmaa, M. Kawasaki, and H. Koinuma, Japanese Journal of Applied Physics Part 2-Letters 38, L603 (1999).

[MCC82] J. R. McColl, Journal of the Electrochemical Society 129, 1546 (1982).

[MEL95] A. Melchinger and S. Hofmann, Journal of Applied Physics 78, 6224 (1995).

[MER00] J. Merikhi and C. Feldmann, Journal of Colloid and Interface Science 228, 121 (2000).

[MEU98] E. A. Meulenkamp, Journal of Physical Chemistry B 102, 5566 (1998).

[MIS94] L. N. Mishenina, T. V. Kazarbina, and V. V. Kozik, Inorganic Materials 30, 733 (1994).

[MON98] S. Monticone, R. Tufeu, and A. V. Kanaev, Journal of Physical Chemistry B 102, 2854 (1998).

[MUR93] C. B. Murray, D. J. Norris, and M. G. Bawendi, Journal of the American Chemical Society 115, 8706 (1993).

[MUR00] C. B. Murray, C. R. Kagan, and M. G. Bawendi, Annual Review of Materials Science 30, 545 (2000).

[NAK99] Y. Nakanishi, H. Wada, H. Kominami, M. Kottaisamy, T. Aoki, and Y. Hatanaka, Journal of the Electrochemical Society 146, 4320 (1999).

[NOG02] M. Nogami, T. Enomoto, and T. Hayakawa, Journal of Luminescence 97, 147 (2002).

[NOR02] B. Norris and L. Luffman, Information Display 18, 32 (2002).

[OZA71] L. Ozawa and P. M. Jaffe, Journal of the Electrochemical Society 118, 1678 (1971).

[OZA81] L. Ozawa, Journal of the Electrochemical Society 128, 2484 (1981).

[OZA90] Ozawa, Cathodoluminescence : Theory and Applications (VCH, New York, 1990).

[PAN71] J. I. Pankove, Optical Processes in Semiconductors (Dover Publications, New York, 1971).

[PAT97] K. C. Patil and S. Ekambaram, Journal of Alloys and Compounds 248, 7 (1997).

[PIE87] R. F. Pierret, Advanced Semiconductor Fundamentals, Vol. IV (Addison-Wesley Publishing Company, Reading, Massachusetts, 1987).

[POO01] A. Poor, Information Display 17, 18 (2001).

[QAD99] S. B. Qadri, E. F. Skelton, D. Hsu, A. D. Dinsmore, J. Yang, H. F. Gray, and B. R. Ratna, Physical Review B (Condensed Matter) 60, 9191 (1999).

[RAB87] E. M. Rabinovich, J. Shmulovich, V. J. Fratello, and N. J. Kopylov, American Ceramic Society Bulletin 66, 1505 (1987).

[RAJ00] M. Rajalakshmi, A. K. Arora, B. S. Bendre, and S. Mahamuni, Journal of Applied Physics 87, 2445 (2000).

[RAN01] G. Z. Ran, Y. Chen, F. C. Yuan, Y. P. Qiao, J. S. Fu, Z. C. Ma, W. H. Zong, and G. G. Qin, Solid State Communications 118, 599 (2001).

[RAO96] R. P. Rao, Journal of the Electrochemical Society 143, 189 (1996).

[RAV97] D. Ravichandran, R. Roy, A. G. Chakhovskoi, C. E. Hunt, W. B. White, and S. Erdei, Journal of Luminescence 71, 291 (1997).

[RAV99] D. Ravichandran, R. Roy, P. Ravindranathan, and W. B. White, Journal of the American Ceramic Society 82, 1082 (1999).

[RED96] K. R. Reddy, K. Annapurna, and S. Buddhudu, Materials Research Bulletin 31, 1355 (1996).

[REE88] J. R. Reed, Introduction to the Principles of Ceramic Processing (John Wiley & Sons, New York, 1988).

[REI00] R. Reisfeld, M. Gaft, T. Saridarov, G. Panczer, and M. Zelner, Materials Letters 45, 154 (2000).

[REU01] R. H. Reuss and B. R. Chalamala, Information Display 17, 28 (2001).

[REY97] D. C. Reynolds, D. C. Look, B. Jogai, and H. Morkoc, Solid State Communications 101, 643 (1997).

[REY98] D. C. Reynolds, D. C. Look, B. Jogai, C. W. Litton, T. C. Collins, W. Harsch, and G. Cantwell, Physical Review B 57, 12151 (1998).

[ROB76] D. J. Robbins, Journal of the Electrochemical Society 123, 1219 (1976).

[ROB80] J. M. Robertson and M. W. Van Tol, Applied Physics Letters 37, 471 (1980).

[ROD97] J. Rodriguez, K. F. Jensen, H. Mattoussi, J. Michel, B. O. Dabbousi, and M. G. Bawendi, Applied Physics Letters 70, 2132 (1997).

[RUA98] S.-K. Ruan, J.-G. Zhou, A.-M. Zhong, J.-F. Duan, X.-B. Yang, and M.-Z. Su, Journal of Alloys and Compounds 275-277, 72 (1998).

[SEA97] C. H. Seager, W. L. Warren, and D. R. Tallant, Journal of Applied Physics 81, 7994 (1997).

[SEA98] C. H. Seager, Applied Physics Letters 73, 85 (1998).

[SEA00a] C. H. Seager and D. R. Tallant, Journal of Applied Physics 87, 4264 (2000).

[SEA00b] C. H. Seager and D. R. Tallant, 20th International Display Research Conference, 382 (2000).

[SEL82] C. Sella, J. C. Martin, and Y. Charreire, Thin Solid Films 90, 181 (1982).

[SEL01] S. T. Selvan, T. Hayakawa, and M. Nogami, Journal of Non-Crystalline Solids 291, 137 (2001).

[SHA92] V. Shanker, S. Chatterjee, and P. K. Ghosh, Journal of Applied Physics 72, 5416 (1992).

[SHE96] L. E. Shea, J. McKittrick, O. A. Lopez, and E. Sluzky, Journal of the American Ceramic Society 79, 3257 (1996).

[SHE97] L. E. Shea, J. Mckittrick, O. A. Lopez, E. Sluzky, and M. L. F. Phillips, Journal of the SID 5, 117 (1997).

[SHI98] S. Shionoya and W. M. Yen, Phosphor Handbook (CRC press, Boca Raton, 1998).

[SKO85] D. Skoog and D. West, Analytical Chemistry: An Introduction (Saunders College Publishing, New York, 1985).

[SOU00] J. C. Souriau, Y. Dong Jiang, J. Penczek, H. G. Paris, and C. J. Summers, Materials Science and Engineering B 76, 165 (2000).

[STO00] C. Stoffers, R. Y. Lee, J. Penczek, B. K. Wagner, and C. J. Summers, Applied Physics Letters 76, 949 (2000).

[STR70] C. W. Struck and W. H. Fonger, Journal of Luminescence 1,2, 456 (1970).

[STR76] C. W. Struck and W. H. Fonger, Journal of Chemical Physics 64, 1784 (1976).

[STU02] S. A. Studenikin and M. Cocivera, Journal of Applied Physics 91, 5060 (2002).

[SUN00] L. D. Sun, J. Yao, C. G. Liu, C. S. Liao, and C. H. Yan, Journal of Luminescence 87-9, 447 (2000).

[SWA99] H. C. Swart, A. P. Greeff, P. H. Holloway, and G. L. P. Berning, Applied Surface Science 140, 63 (1999).

[SZE81] S. M. Sze, Physics of Semiconductor Devices, 2nd edition ed. (John Wiley & Sons, New York, 1981).

[TAK03] I. Takeuchi, W. Yang, K. S. Chang, M. A. Aronova, T. Venkatesan, R. D. Vispute, and L. A. Bendersky, Journal of Applied Physics 94, 7336 (2003).

[TAL01] A. A. Talin, K. A. Dean, and J. E. Jaskie, Solid-State Electronics 45, 963 (2001).

[TAL02] D. R. Tallant, C. H. Seager, and R. L. Simpson, Journal of Applied Physics 91, 4053 (2002).

[TAN00a] M. Tanaka and Y. Masumoto, Chemical Physics Letters 324, 249 (2000).

[TAN00b] M. Tanaka, J. Qi, and Y. Masumoto, Journal of Crystal Growth 214-215, 410 (2000).

[TAY62] K. N. R. Taylor, Journal of Physics and Chemistry of Solids 23, 1689 (1962).

[THO02] W. J. Thomes, C. H. Seager, and P. H. Holloway, Journal of Applied Physics 91, 9657 (2002).

[TSA94] M. Tsai and M. Hon, Ceramics International 20, 303 (1994).

[UEK03] N. Uekawa, N. Mochizuki, J. Kajiwara, F. Mori, Y. J. Wu, and K. Kakegawa, Physical Chemistry Chemical Physics 5, 929 (2003).

[UHL97] D. R. Uhlmann, T. Suratwala, K. Davidson, J. M. Boulton, and G. Teowee, Journal of Non-Crystalline Solids 218, 113 (1997).

[UIT66] L. G. V. Uitert and L. F. Johnson, Journal of Chemical Physics 44, 3514 (1966).

[UIT67a] L. G. V. Uitert, Journal of the Electrochemical Society 114, 1048 (1967).

[UIT67b] L. G. V. Uitert, E. F. Dearborn, and J. J. Rubin, Journal of Chemical Physics 47, 547 (1967).

[VAN96] K. Vanheusden, W. L. Warren, C. H. Seager, D. R. Tallant, J. A. Voigt, and B. E. Gnade, Journal of Applied Physics 79, 7983 (1996).

[VON85] H. Von Seggern, IEEE Transactions on Nuclear Science NS-32, 1503 (1985).

[WAG00] B. K. Wagner, F. Zhang, P. Manigault, W. Park, C. J. Summers, P. N. Yocom, and D. Zarimba, The 7th International Display Workshops, 833 (2000).

[WAN02] J. N. Wang, C. L. Yang, S. H. Wang, L. Guo, S. H. Yang, I. K. Sou, and W. K. Ge, International Journal of Modern Physics B 16, 4363 (2002).

[WER01] K. Werner, Information Display 17, 14 (2001).

[WON98] E. M. Wong, J. E. Bonevich, and P. C. Searson, Journal of Physical Chemistry B 102, 7770 (1998).

[XIN03] Y. J. Xing, Z. H. Xi, Z. Q. Xue, X. D. Zhang, J. H. Song, R. M. Wang, J. Xu, Y. Song, S. L. Zhang, and D. P. Yu, Applied Physics Letters 83, 1689 (2003).

[YAM91] H. Yamamoto and H. Matsukiyo, Journal of Luminescence 48-49, 43 (1991).

[YAN98a] S. Yang, Ph.D. Dissertation, Georgia Institute of Technology, 1998.

[YAN98b] S. Yang, C. Stoffers, F. Zhang, S. M. Jacobsen, B. K. Wagner, C. J. Summers, and N. Yocom, Applied Physics Letters 72, 158 (1998).

[YAN02] P. Yang, M. Kai Lu, C. Feng Song, G. Jun Zhou, D. Xu, and D. Rong Yuan, Inorganic Chemistry Communications 5, 187 (2002).

[YU99] S. H. Yu, Z. H. Han, J. Yang, H. Q. Zhao, R. Y. Yang, Y. Xie, Y. T. Qian, and Y. H. Zhang, Chemistry of Materials 11, 192 (1999).

[ZAK91] A. Zakrzwski and M. Godlewski, Applied Surface Science 50, 257 (1991).

[ZEL01] M. Zelner, H. Minti, R. Reisfeld, H. Cohen, Y. Feldman, S. R. Cohen, and R. Tenne, Journal of Sol-Gel Science and Technology 20, 153 (2001).

[ZIE72] J. P. V. Ziel, L. Kopf, and L. G. V. Uitert, Physical Review B 6, 615 (1972).

BIOGRAPHICAL SKETCH

Jungsik Bang was born in Seoul, Republic of Korea on September 15, 1967. He grew up and was educated in his hometown. He attended the Department of Chemical Technology at the Seoul National University in 1986 to study chemistry and engineering. After graduation in 1990, he attended graduate school at the Seoul National University and worked on the surface chemistry of Hydrogen and Deuterium on Si surface under the guidance of Dr. Jiwha Lee. Jungsik Bang obtained his Master of Engineering degree in February of 1992. After graduation, he worked for eight and half years as a research scientist for LG Chemicals, Taejon, Korea. His research topics at LG Chemicals were the development of large scale process for cephalosporins antibiotics, development of continuous process for submicron-sized barium titanates, synthesis of carbon nano-fibrils, synthesis of round shaped green CRT phosphors, and development of highly pigmented blue and red CRT phosphors. In 1997, he visited the Dr. Holloway's Lab. at the University of Florida and studied the degradation of phosphors under electron beam bombardment for six months. In the summer of 2000, he entered the Department of Materials Science and Engineering at the University of Florida and worked for Dr. Paul H. Holloway. Jungsik Bang worked on the combustion synthesis of metal oxysulfide, temporal cathodoluminescence quenching from powder phosphors, luminescent properties of zinc oxide nanoparticles and energy transfer from nanoparticles to activators. Under the continuing guidance of Dr. Holloway, Jungsik Bang obtained his Master of Science degree in August of 2003 and Ph. D. degree in August of 2004.

I certify that I have read this study and that in my opinion it conforms to acceptable standards of scholarly presentation and is fully adequate, in scope and quality, as a dissertation for the degree of Doctor of Philosophy.

Paul H. Holloway, Chairman
Distinguished Professor of Materials
Science and Engineering

I certify that I have read this study and that in my opinion it conforms to acceptable standards of scholarly presentation and is fully adequate, in scope and quality, as a dissertation for the degree of Doctor of Philosophy.

David Norton
Professor of Materials Science and
Engineering

I certify that I have read this study and that in my opinion it conforms to acceptable standards of scholarly presentation and is fully adequate, in scope and quality, as a dissertation for the degree of Doctor of Philosophy.

Wolfgang Sigmund
Associate Professor of Materials Science
and Engineering

I certify that I have read this study and that in my opinion it conforms to acceptable standards of scholarly presentation and is fully adequate, in scope and quality, as a dissertation for the degree of Doctor of Philosophy.

Rajiv Singh
Professor of Materials Science and
Engineering

I certify that I have read this study and that in my opinion it conforms to acceptable standards of scholarly presentation and is fully adequate, in scope and quality, as a dissertation for the degree of Doctor of Philosophy.

David Tanner
Professor of Physics

This dissertation was submitted to the Graduate Faculty of the College of Engineering and to the Graduate School and was accepted as partial fulfillment of the requirements for the degree of Doctor of Philosophy.

August 2004

Pramod Khargonekar

Pramod P. Khargonekar
Dean, College of Engineering

Kenneth J. Gerhardt
Interim Dean, Graduate School